5-24-2017 12:00 AM

Tools for improving high-dose-rate prostate cancer brachytherapy using three-dimensional ultrasound and magnetic resonance imaging

William T. Hrinivich
The University of Western Ontario

Supervisor
Eugene Wong
The University of Western Ontario Joint Supervisor
Aaron Fenster
The University of Western Ontario

Graduate Program in Medical Biophysics
A thesis submitted in partial fulfillment of the requirements for the degree in Doctor of Philosophy
© William T. Hrinivich 2017

Abstract

High-dose-rate brachytherapy (HDR-BT) is an interstitial technique for the treatment of intermediate and high-risk localized prostate cancer that involves placement of a radiation source directly inside the prostate using needles. Dose-escalated whole-gland treatments have led to improvements in survival, and tumour-targeted treatments may offer future improvements in therapeutic ratio. The efficacy of tumour-targeted HDR-BT depends on imaging tools to enable accurate dose delivery to prostate subvolumes. This thesis is focused on implementing ultrasound tools to improve HDR-BT needle localization accuracy and efficiency, and evaluating dynamic contrast enhanced magnetic resonance imaging (DCE-MRI) for tumour localization.

First, we implemented a device enabling sagittally-reconstructed 3D (SR3D) ultrasound, which provides sub-millimeter resolution in the needle insertion direction. We acquired SR3D and routine clinical images in a cohort of 12 consecutive eligible HDR-BT patients, with a total of 194 needles. The SR3D technique provided needle insertion depth errors within 5 mm for 93% of needles *versus* 76% for the clinical imaging technique, leading to increased precision in dose delivered to the prostate.

Second, we implemented an algorithm to automatically segment multiple HDR-BT needles in a SR3D image. The algorithm was applied to the SR3D images from the first patient cohort, demonstrating mean execution times of 11.0 s per patient and successfully segmenting 82% of needles within 3 mm.

Third, we augmented SR3D imaging with live-2D sagittal ultrasound for needle tip localization. This combined technique was applied to another cohort of 10 HDR-BT patients, reducing insertion depth errors compared to routine imaging from a range of [-8.1 mm, 7.7 mm] to [-6.2 mm, 5.9 mm].

Finally, we acquired DCE-MRI in 16 patients scheduled to undergo prostatectomy, using either high spatial resolution or high temporal resolution imaging, and compared the images to whole-mount histology. The high spatial resolution images demonstrated

improved high-grade cancer classification compared to the high temporal resolution images, with areas under the receiver operating characteristic curve of 0.79 and 0.70, respectively.

In conclusion, we have translated and evaluated specialized imaging tools for HDR-BT which are ready to be tested in a clinical trial investigating tumour-targeted treatment.

Co-Authorship Statement

The following thesis contains four manuscripts produced in collaboration with multiple authors. One manuscript has been published in a peer-reviewed scientific journal, one manuscript has been accepted for publication in a peer-reviewed scientific journal, one manuscript has been submitted for publication in a scientific journal and is currently under peer-review, and one manuscript is in preparation for submission. As the first author of these manuscripts, I was a significant contributor to all aspects of the studies including study conception and design, data analysis, drafting, and revising the manuscripts, and additional specific responsibilities indicated for each chapter.

Chapter 2 is an original research article entitled "Three-dimensional transrectal ultrasound guided high-dose-rate prostate brachytherapy: a comparison of needle segmentation accuracy with two-dimensional image-guidance" and was published in *Brachytherapy* in 2016. This manuscript was co-authored by W. Thomas Hrinivich, Douglas A. Hoover, Kathleen Surry, Chandima Edirisinghe, Jacques Montreuil, David D'Souza, Aaron Fenster, and Eugene Wong. My specific responsibilities included commissioning the mechatronic device hardware and software for use during high-dose-rate prostate brachytherapy procedures, image acquisition and data collection at all brachytherapy procedures, device sanitation and quality assurance, image segmentation and statistical analysis, and phantom design, construction, and scanning. Douglas Hoover and Kathleen Surry assisted with study design, device and hardware commissioning, image acquisition, segmentation analysis, and manuscript preparation. Chandima Edirisinghe and Jacques Montreuil were responsible for implementing hardware and software modifications required to commission the mechatronic device for high-dose-rate prostate brachytherapy. David D'Souza was the physician who performed the brachytherapy procedures, and was the principal investigator of this imaging study. Aaron Fenster and Eugene Wong contributed to the study conception, design, drafting, and revising the manuscript.

Chapter 3 is an original research article entitled "Simultaneous automatic segmentation of multiple needles using 3D ultrasound for high-dose-rate prostate brachytherapy". This manuscript was accepted for publication in *Medical Physics* on January 29, 2017 and is available through *Epub ahead of print*. This manuscript was co-authored by W. Thomas Hrinivich, Douglas A. Hoover, Kathleen Surry, Chandima Edirisinghe, Jacques Montreuil, David D'Souza, Aaron Fenster, and Eugene Wong. This study involved developing and applying an image processing algorithm to the images acquired during the study in Chapter 2. My specific responsibilities included designing, implementing, and validating the algorithm. The remaining co-authors had identical responsibilities to those listed for Chapter 2.

Chapter 4 is an original research article entitled "Improved high-dose-rate prostate brachytherapy needle tip localization using live two-dimensional and sagittally-reconstructed three-dimensional ultrasound" and was submitted to *Brachytherapy* on March 7, 2017 and is currently under peer-review. This manuscript was co-authored by W. Thomas Hrinivich, Douglas A. Hoover, Kathleen Surry, Chandima Edirisinghe, Vikram Velker, Glenn Bauman, David D'Souza, Aaron Fenster, and Eugene Wong. My specific responsibilities included commissioning the intra-operative needle segmentation software for use during high-dose-rate prostate brachytherapy procedures, image acquisition and data collection at all brachytherapy procedures, device sanitation and quality assurance, and image and statistical analysis. Douglas Hoover assisted with the study design, image acquisition, manuscript preparation, and participated in the needle segmentation observer study. Kathleen Surry assisted with study design and image acquisition. Chandima Edirisinghe implemented the software modifications required to commission the intra-operative needle segmentation software. Vikram Velker and Glenn Bauman were the physicians who performed a portion of the brachytherapy procedures and assisted in drafting the manuscript. David D'Souza was the physician who performed the majority of the brachytherapy procedures and was the principal investigator of this

imaging study. Aaron Fenster and Eugene Wong contributed to the study conception, design, drafting, and revising the manuscript.

Chapter 5 is an original research article entitled "Spatial *versus* temporal resolution of dynamic contrast enhanced MRI for prostate cancer localization: Comparing images from two pulse sequences with histology" and is in preparation for submission to the *Journal of Magnetic Resonance Imaging*. This manuscript was co-authored by W. Thomas Hrinivich, Eli Gibson, Peter Martin, Mena Gaed, Aaron Ward, Charles McKenzie, Glenn Bauman, Aaron Fenster, and Eugene Wong. My specific responsibilities included applying the reference region pharmacokinetic model to the prostate, producing DCE-MRI parameter maps, and performing all region-based and voxel-wise statistical analysis. Eli Gibson and Peter Martin were responsible for registering whole mount histology slides to the *in vivo* image space. Mena Gaed was the pathologist responsible for all whole-mount histology contouring. Aaron Ward assisted with study design, whole-mount histology registration, and provided access to the image data. Charles McKenzie was responsible for MRI pulse sequence design and assisted with image interpretation. Glenn Bauman assisted with study design and led the MR imaging study. Aaron Fenster and Eugene Wong contributed to the study conception, design, and drafting the manuscript.

Dedication

To my parents, Bill and Tina.

Acknowledgments

Thank you to my supervisor, Eugene Wong. You introduced me to the world of research and medical physics when I was a 2nd year undergraduate student and made me into the researcher I am today. It has been a true pleasure working together for the last 7 years. Thank you to my co-supervisor, Aaron Fenster. Working in your group for the last 5 years has been an incredible experience. Thank you to my advisory committee members David D'Souza, Kathleen Surry, and Doug Hoover. Your expertise, talent, and dedication to research made this work possible.

Thank you to everyone who assisted me during my graduate studies and contributed to the work described in this thesis. Chandima Edirisinghe, Jacques Montreuil, David Tessier, Igor Gyacskov, Kevin Barker, Lori Gardi, Bon Ryu, Wu Qiu, Eli Gibson, the many other past and present members of the Fenster lab, Aaron Ward, Peter Martin, Khadija Sheikh, Brian Dalrymple, Frank Van Sas, Jeff Chen, Anthony Lausch, Michael Jensen, Nili Zargami, the many other students and physicists at the London Regional Cancer Program, Charles McKenzie, Tammie Murray, Leanne Derrah, Matt Mulligan, Homeira Mosalaei, Linada Kaci, Vikram Velker, Glenn Bauman, Jerry Battista, Barb Barons, Grace Parraga, Rob Stodilka, Wendy Hough, and anyone I forgot to mention. Thank you to the friends I've made over the last 5 years at Robarts Research Institute and the London Regional Cancer Program. Spencer Martin, Damien Pike, Jesse Tanguay, Jeremy Cepek, and many more.

Thank you to my parents, Bill and Tina. Your love and support are behind all of my accomplishments. Thank you to my sister Ellen, my lifelong friends Glenn Austin Gaviller, Nate Hayward, Chris Pantlin, Evan Wyborn-Creamer, the London BMX community, and everyone else.

Finally, thank you to my examination committee members Ananth Ravi, Tamie Poepping, Tracy Sexton, and Kevin Jordan for taking the time to critically review this thesis and participate in my defense.

Contents

List of Figures

List of Tables

List of Appendices

List of Abbreviations

^{125}I	iodine-125
^{192}Ir	iridium-192
3DHT	three-dimensional Hough transform
3TP	three time point method
ADC	apparent diffusion coefficient
AIF	arterial input function
AR3D	axially-reconstructed three-dimensional
AUC	area under the receiver operating characteristic curve
bDFS	biochemical disease free survival
CBCT	cone-beam CT
CT	x-ray computed tomography
CTV	clinical target volume
D90%	dose delivered to 90% of the target volume
DCE	dynamic-contrast-enhanced
DIL	dominant index lesion
DNA	deoxyribonucleic acid
DRE	digital rectal examination
DW	diffusion-weighted
EBRT	external beam radiotherapy
EES	extra-cellular extra-vascular space
EM	electromagnetic
FSPGR	fast spoiled gradient echo
Gd	gadolinium
GTV	gross tumour volume
HDR-BT	high-dose-rate brachytherapy
IDE	insertion depth error
IMCT	intensity modulated carbon-ion therapy
IMPT	intensity modulated proton therapy
IMRT	intensity modulated radiotherapy
K^{trans}	pharmacokinetic transfer constant
k_{ep}	pharmacokinetic rate constant
L-BFGS	limited-memory Broyden-Fletcher-Goldfarb-Shanno
LDR-BT	low-dose-rate brachytherapy

MLC	multi-leaf collimator
MMI	Mattes mutual information
mpMRI	multi-parametric magnetic resonance imaging
MRI	magnetic resonance imaging
MRS	magnetic resonance spectroscopy
OIM	obturator internus muscle
PET	positron emission tomography
PIN	prostatic intra-epithelial neoplasia
PIP	parallel integral projection
PSA	prostate specific antigen
PSMA	prostate specific membrane antigen
PTV	planning target volume
r	direction radial to TRUS probe axis of rotation
RANSAC	random sample consensus
ROC	receiver operating characteristic
RRM	reference region model
SAAR	sagittally-assisted axially-reconstructed
SASR	sagittally-assisted sagittally-reconstructed
SD	standard deviation
SNR	signal-to-noise ratio
SPECT	single photon emission computed tomography
SR3D	sagittally-reconstructed three-dimensional
t	direction tangential to TRUS probe axis of rotation
T1w	T1-weighted
T2w	T2-weighted
TE	echo time
TR	repetition time
TRUS	trans-rectal ultrasound
v_e	extra-cellular extra-vascular space fractional volume
V100%	volume of the target receiving 100% of the prescribed dose
V120%	volume of the target receiving 120% of the prescribed dose
VMAT	volumetric modulated arc therapy
WG	wash-out gradient

Chapter 1

General Introduction

Prostate cancer is the second leading cause of cancer-related death among men in developed countries [1]. Conventional radiotherapy targeting the whole prostate is limited by toxicity in surrounding organs [2, 3]. High-dose-rate prostate brachytherapy is a radiotherapy technique that delivers lower dose to surrounding organs than other techniques [4]. Ultrasound can be used to guide high-dose-rate prostate brachytherapy [5], and magnetic resonance imaging can be used to localize prostate tumours [6]. Optimizing these imaging techniques for tumour-targeted high-dose-rate prostate brachytherapy may lead to improvements in local disease control and cause-specific survival.

1.1   Prostate Cancer

Prostate cancer is the most commonly diagnosed non-cutaneous cancer and the third leading cause of cancer-related death in Canadian men, with an estimated 26,200 new cases and 4,000 deaths in 2016 [7]. Accordingly, it is estimated that 1 in 8 Canadian men will develop prostate cancer in his lifetime, and 1 in 27 Canadian men will die from the disease [7]. Prostate cancer is also the most commonly diagnosed non-cutaneous cancer and the second leading cause of cancer-related death among men in developed countries [1] with an estimated 180,890 new cases and 26,120 deaths in 2016 in the United States alone [8].

Physiologically, the prostate is an accessory organ of the male reproductive system surrounding the urethra inferior to the bladder and anterior to the rectum [9]. The prostate contributes secretions to semen including buffers, enzymes, and nutrients for

1

sperm metabolism [10]. Prostate tissue is characterized by the presence of 30 to 40 glands lined with epithelial cells which drain into the prostatic urethra through ducts [9, 10]. The most common prostate cancer, adenocarcinoma, is characterized by the development of abnormal cells in prostate glands [11]. These abnormal cells grow in a disorganized and uncontrolled manner and have the potential to metastasize to other tissues [12].

The prostate is not critical to survival, and mortality from prostate cancer is caused by metastatic disease [13, 14]. Prostate cancer metastases most commonly manifest in the lymph nodes, bones, lung, and liver [14]. Aside from the risk of premature mortality, prostate cancer is associated with adverse genitourinary symptoms, pain, and general malaise with frequency and severity depending on disease stage [15, 16]. Diagnostic and therapeutic procedures are also associated with physical side-effects that are described further in subsequent sections. Prostate cancer treatments lead to improvements in disease control, but evidence of prostate cancer recurrence five years following treatment remains at 15-66% for high-risk disease [2, 3], and treatment aggressiveness is limited by treatment toxicities [17–19]. Increasing treatment aggressiveness to reduce rates of prostate cancer recurrence while minimizing toxicity is the long-term clinical objective motivating the work described in this thesis.

1.2 Prostate Cancer Diagnosis

The selection of a prostate cancer treatment is preceded by an initial diagnosis. Patients are typically screened for signs of prostate cancer using the digital rectal examination (DRE) and the prostate-specific-antigen (PSA) blood test [20]. The DRE refers to the clinical procedure in which a physician palpates the prostate using a gloved finger placed in the rectum. Prostate cancer tends to create lumps which can be detected through palpation. DRE can be used to detect cancers in the posterior peripheral zone

of the prostate, but fails to detect 45% of biopsy-confirmed cancers [21]. PSA is a glycoprotein produced by cells in the prostate that can be detected in a blood sample. Serum PSA concentrations have been shown to correlate with prostate cancer presence [22] and prognostic factors such as tumour volume [23]. PSA screening in the general population is not recommended due to over-diagnosis of very low-risk disease that is unlikely to become symptomatic in the patient's lifetime [24]. PSA tests are currently used to screen men suspected of having prostate cancer based on additional information such as symptom presentation or a DRE [20], and to monitor treatment response [25, 26]. Rising PSA following treatment is referred to as biochemical recurrence and is considered a precursor to prostate cancer recurrence and/or metastasis and mortality [27]. Biochemical disease-free survival (bDFS) refers to patient survival with the absence of a rise in PSA or any other signs of recurrence, and is a common measurement in clinical trials investigating prostate cancer treatments.

For patients exhibiting signs of prostate cancer, an initial diagnosis is made based on the results of a trans-rectal biopsy involving the systematic retrieval of small tissue samples from varying regions within the prostate using needles inserted via the rectum. These small tissue samples, referred to as cores, are then analyzed in a pathology lab to determine whether cancer is present. If cancer is present, the cores are used to characterize, or stage, the cancer. An estimate of the spatial cancer distribution is determined based on the number, distribution, and fraction of biopsy cores containing cancerous cells [28], and an estimate of the cancer aggressiveness is determined based on the characteristics of the cancer cells themselves as visible under a microscope. A standardized numeric scoring system from 6-10, called the Gleason score, is used to characterize the architecture of prostate cancer cells on tissue samples [11]. Higher Gleason scores correspond to architectural characteristics tending towards greater disorganization, with higher scores also associated with increased risks of prostate cancer mortality [20].

A patient's overall risk of prostate cancer mortality is typically estimated using all available diagnostic information and stratified into one of four broad categories for clinically localized disease: very low risk, low risk, intermediate risk, and high risk [20]. Table 1.1 summarizes risk stratification criteria such as PSA concentration, Gleason score, and tumour burden recommended by the National Comprehensive Cancer Network (NCCN) [20]. Risk of cancer recurrence following curative-intent treatment is increased in higher-risk groups, with specific risk of recurrence dependent on the treatment modality selected [29]. There is the potential for exceptions from the guidelines listed in Table 1.1. Furthermore, diagnostic information may not be entirely accurate. PSA tests fail to detect 18% of biopsy-confirmed cancers [21] and may be elevated in patients without clinically significant disease [30]. Systematic trans-rectal biopsies only sample small portions of prostate tissue leading to cancer under-sampling in 23% of patients [31]. Investigators have proposed the use of image-guided trans-rectal biopsies using magnetic resonance imaging (MRI) or a combination of MRI and ultrasound to decrease the false negative rate of trans-rectal biopsies [32, 33].

risk group	PSA conc. (ng/ml)	Gleason score	T-stage
very low	<10	≤ 6	T1c (only detected through elevated PSA)
low	<10	≤ 6	T1-T2a (half a lobe or less)
intermediate	10-20	7	T2b-T2c (more than half a lobe or both lobes)
high	>20	≥ 8	T3a (extra-capsular extension)

Table 1.1: Summary of NCCN risk stratification criteria for mortality from clinically localized prostate cancer [20]

1.3   Prostate Cancer Imaging

Medical imaging provides a spatial characterization of tissue non-invasively which can be applied to the diagnosis, treatment planning, treatment delivery guidance, and treatment response assessment of prostate cancer. There are multiple medical imaging tech-

niques with applications related to prostate cancer. The most common imaging techniques for treatment delivery guidance are x-ray computed tomography (CT) and ultrasound, and the most common techniques for prostate cancer localization are nuclear imaging and MRI.

1.3.1   X-ray Computed Tomography

CT imaging involves the projection of X-rays through tissue at various angles, and detection of the X-rays that pass through the sample. The detected X-ray fluence at varying projection angles can be used to reconstruct a map of X-ray attenuation coefficients in tissue. CT scans are critically important for certain radiotherapy planning techniques. CT scans acquired with a fan-beam geometry provide accurate electron density information and high spatial resolution required for external beam radiotherapy (EBRT) dose calculations and treatment planning [34]. An example of a fan-beam CT image of the prostate is provided in Figure 1.1. CT scans acquired with a cone-beam geometry (CBCT) can be acquired immediately prior to EBRT delivery using on-board imaging devices to verify treatment setup geometry [35]. CT scans can also be used to verify the placement of interstitial needles and seeds in brachytherapy procedures [36, 37].

At diagnostic X-ray energies ($\sim$140 kV for pelvic imaging), X-ray attenuation coefficients do not vary significantly in pelvic soft tissue, so raw CT scans cannot be used for reliable cancer localization in the prostate [38]. CT demonstrates utility in the identification of bone-lesions in high-risk prostate cancer [39]. Furthermore, iodinated contrast agents can be injected systemically followed by repeated CT imaging of the region of interest to observe contrast agent dynamics, referred to as dynamic-contrast-enhanced (DCE)-CT. DCE-CT can be analyzed to estimate variations in vascular parameters associated with prostate cancer for intra-prostatic tumour localization [40].

1.3.2   Ultrasound

Brightness-mode, or B-mode ultrasound imaging involves the application and detection of mechanical waves at frequencies above 20 kHz to produce images at 10-30 frames per second. Resultant image intensities are related to ultrasound scatter, attenuation, and echogenicity (the ability to return an echo from an applied ultrasound signal). Higher ultrasound frequencies provide higher spatial resolution but also lead to greater signal attenuation. Ultrasound with frequencies of 5-10 MHz can provide high soft tissue contrast over a 5-10 cm field of view, and trans-rectal ultrasound (TRUS) is used routinely for prostate volume measurement [41] and trans-rectal biopsy guidance [31]. TRUS can also be used for radiotherapy guidance [42, 43]. Like CT, B-mode TRUS demonstrates limited sensitivity to intra-prostatic cancer, which can appear relatively hypo-intense compared to normal tissue [44]. Conventional TRUS images are 2D, and modern bi-plane probes incorporate two perpendicular transducers for imaging axial and sagittal planes, which are both employed in this thesis. 2D TRUS spatial resolution varies with distance from the probe and the gain settings, with typical values of 0.3-0.6 mm in-plane (axial and lateral resolution) [45] and 1.5-4.0 mm out-of-plane (elevational resolution or "slice thickness") [46].

Mechanical probe tracking and manipulation enables acquisition and reconstruction of 3D TRUS images using either the axial transducer or sagittal transducer [47, 48]. A bi-plane TRUS probe and a mechatronic device enabling acquisition and axially-reconstructed 3D (AR3D) and sagittally-reconstructed 3D (SR3D) TRUS [49] are shown in Figure 1.2. Schematics of probe manipulation for AR3D and SR3D TRUS reconstruction are provided in Figure 1.3. The axial transducer is used for AR3D acquisition, and the probe is mechanically stepped in the superior/inferior direction. The sagittal transducer is used for SR3D acquisition, and the probe is mechanically rotated. AR3D and SR3D TRUS have spatial resolution components corresponding to the axial, lateral, and elevational resolutions of the 2D images used for reconstruction.
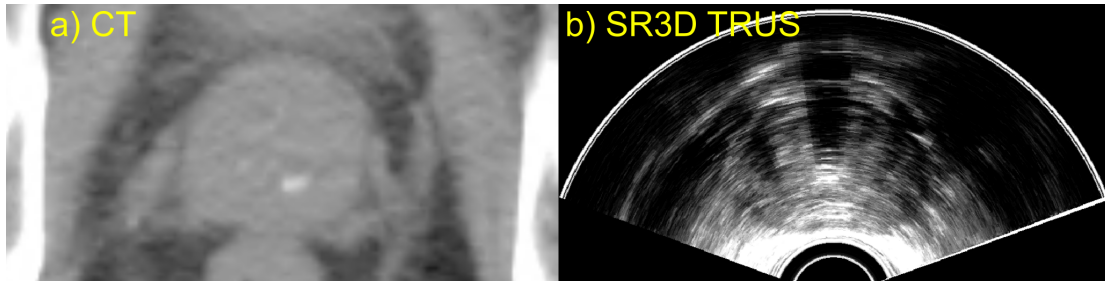
Figure 1.1: Example CT and SR3D trans-rectal ultrasound (TRUS) images from two separate prostate cancer patients acquired for EBRT and brachytherapy treatment planning, respectively.
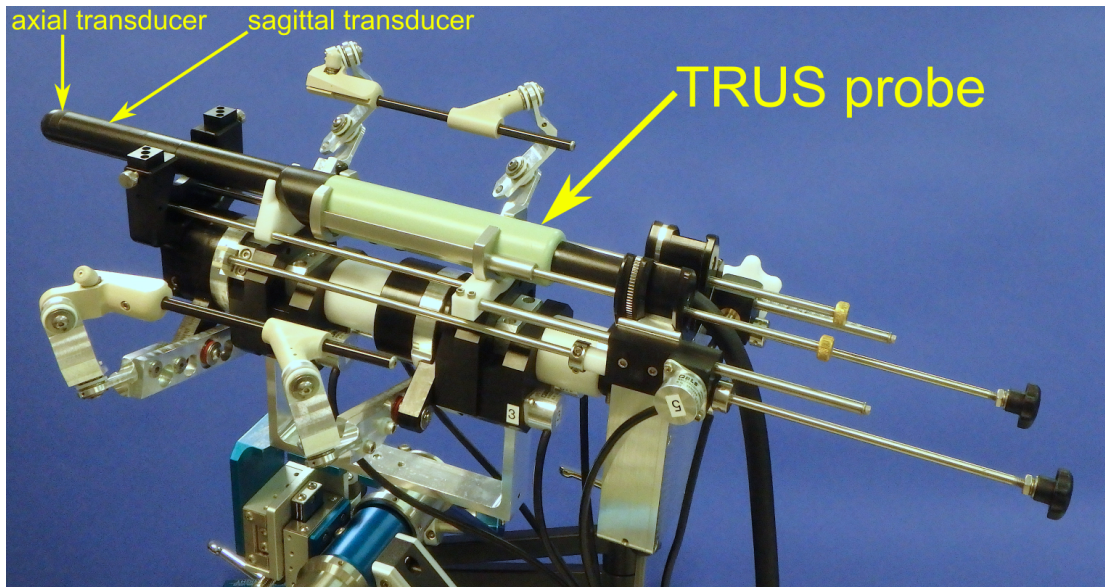
Figure 1.2: A bi-plane 8658 TRUS probe (BK Medical, Boston MA) and mechatronic device for image-guided trans-perineal needle insertions capable of acquiring AR3D and SR3D TRUS. This device is investigated in this thesis. The two transducer locations on the TRUS probe are indicated.

1.3.3 Nuclear Imaging

Nuclear imaging involves the systemic injection of a radiopharmaceutical, referred to as a tracer, followed by the detection of the radioactive emissions to produce an image of the spatial distribution of the tracer in tissue. The most common forms of nuclear imaging techniques are single photon emission computed tomography (SPECT) and positron emission tomograpy (PET), which are produced by detecting emissions from gamma and positron emitting tracers respectively. Tracers have been designed to highlight differences in rates of cellular metabolism, cellular replication, or amino acid transport associated with cancer [50]. Recently developed PET tracers [51, 52] have been designed to target a cellular surface protein that is found to be up-regulated in prostate cancer, referred to as prostate-specific membrane antigen (PSMA) [53]. Preliminary evidence suggests that PSMA-targeted PET probes may have 100% sensitivity to localized prostate cancer [52], and higher sensitivity than existing PET tracers (e.g. fluorocholine) to metastatic disease [54]. While nuclear imaging techniques are sensitive to cancer, PET and SPECT imaging have limited spatial resolution of 4-10 mm. Advances in hybrid PET/MRI scanners may enable the combination of MRI with PSMA-PET to overcome limitations in PET spatial resolution [52, 55]. Figure 1.4a displays an example PSMA-PET image overlaid on T2-weighted (T2w)-MRI acquired using a hybrid PET/MRI scanner. This is promising for the identification of intra-prostatic tumours, but PSMA-PET is still under investigation in ongoing clinical trials.

1.3.4 Magnetic Resonance Imaging

MRI involves the application of magnetic fields and radio-frequency pulses to tissue to produce detectable signals from atomic nuclei possessing a magnetic moment, typically protons. Depending on the characteristics of the pulse sequence chosen, different properties of the local proton environment can be highlighted. Through these mechanisms, MRI can provide unparalleled soft-tissue contrast, and modern scanners can provide

a) axially-reconstructed
3D TRUS

b) sagittally-reconstructed
3D TRUS

axial
transducer

probe translation

sagittal
transducer

probe rotation
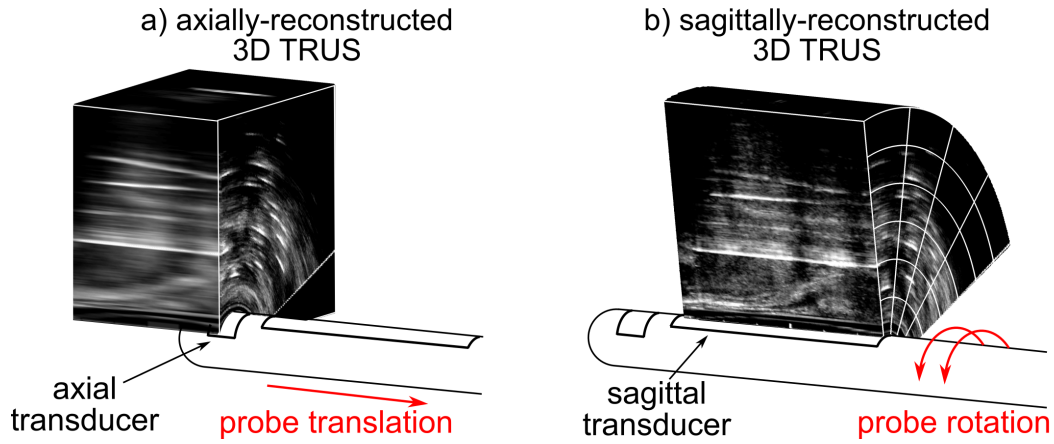
Figure 1.3: Schematic of axially-reconstructed 3D (AR3D) TRUS and sagittally-reconstructed 3D (SR3D) TRUS from a patient with HDR-BT needles *in situ*. Simulated images are cutaway in the sagittal plane to indicate differences in spatial resolution between AR3D and SR3D TRUS in the HDR-BT needle insertion direction.

sub-millimeter spatial resolutions for many pulse sequences [39]. These characteristics make MRI well-suited for prostate cancer detection and localization for diagnosis and treatment planning. For prostate cancer imaging, an endo-rectal coil may be employed. The advantage of an endo-rectal coil is that it leads to improved signal-to-noise ratio (SNR) in the prostate compared to pelvic coils, leading to improved specificity to intra-prostatic tumours [56]. Disadvantages of using an endo-rectal coil include the fact that it is uncomfortable for the patient and deforms the prostate. The following sections describe specific MRI techniques for prostate cancer detection and localization. MRI can also be used for biopsy and treatment delivery guidance [57, 58] and treatment response assessment [59].

T2-weighted MRI

T2-weighted (T2w) image intensities are weighted by the transverse, or T2 relaxation time of protons in tissue, which varies with tissue type [60]. Prostate cancer has been shown to appear hypo-intense on T2w imaging relative to normal prostate tissue [6, 61]. T2w images can be acquired with axial in-plane voxel dimensions <0.5 mm and

slice thickness <1 mm with the use of an endo-rectal coil [62].

Diffusion-weighted MRI

Diffusion-weighted (DW) images have signal intensities weighted by the rate of diffusion (random Brownian motion) of molecules containing protons, primarily water. DW imaging employs spin-echo pulse sequences augmented with diffusion-sensitizing gradients to measure diffusion of water molecules. The strength and timing of these gradients can be adjusted using a parameter called the b-value [units s/mm^2] to modify the sensitivity of the images to diffusion rates [63]. Prostate cancer is characterized by hyper-intensity relative to normal tissue on high b-value images [e.g. b = 1000 s/mm^2][6, 61, 63]. Factors aside from diffusion rates, such as T2 time and proton density, can influence the raw DW image signal intensities, so a common technique to mitigate the impact of these factors is to acquire multiple DW images with differing b-values. These images can be combined to normalize for factors other than diffusion rates, creating maps of apparent diffusion coefficient (ADC) [63]. Prostate cancer has been associated with decreased ADC values relative to normal prostate tissue indicating restricted diffusion in cancerous regions [39]. DW images typically have limited spatial resolution and can suffer from geometric distortions [64].

Dynamic-Contrast-Enhanced MRI

Dynamic-contrast-enhanced (DCE)-MRI detects vascular properties of tissue through the acquisition of multiple sequential MR images before and after injecting a bolus of paramagnetic contrast agent. Prostate cancer has been associated with increased micro-vessel density and area [65] leading to increased rates of contrast agent wash-in and wash-out that can be detected using DCE-MRI [66]. The pulse sequences used for DCE-MRI are weighted by the inverse of the longitudinal proton relaxation time (T1 time), and are associated with increased signal intensity with increased contrast-agent

concentration [67]. Through analysis of a series of T1-weighted (T1w) images over time, contrast agent wash-in and wash-out can be tracked.

Application of pharmacokinetic models to the images enables the calculation of maps of vascular parameters. Specifically, the Tofts two-compartment pharmacokinetic model describes the rate of contrast agent transfer from the vascular space into the extra-vascular extra-cellular space (EES) using the parameter K^{trans}, and the rate of contrast agent transfer from the EES back to the vascular space using the parameter k_{ep}[68]. Prostate cancer is associated with increased K^{trans} values relative to normal tissue [69]. The Tofts model describes the transfer of contrast agent to and from the EES based on passive diffusion driven by concentration gradients, and may be written as

$$C_T(t) = K^{trans} C_A(t) \otimes e^{-k_{ep}t} \tag{1.1}$$

where $C_T(t)$ is the contrast agent concentration measured in tissue at time t, $C_A(t)$ is the arterial contrast agent concentration at time t, and $\otimes$ is a convolution operator. $C_A(t)$ is difficult to measure directly, so the Tofts model is typically applied using a population averaged estimate of $C_A(t)$ [70] or an estimate of $C_A(t)$ based on contrast agent uptake in nearby reference tissue [71].

Since DCE-MRI involves repeated T1w imaging, pulse sequence selection involves a trade-off between spatial and temporal resolutions. Several T1w pulse sequences have been proposed for DCE-MRI with a wide range of acquisition times including 1.4 s/image and 90 s/image with corresponding voxel dimensions of $1.1 \times 1.1 \times 3.0$ mm^3 and $0.55 \times 0.55 \times 2.6$ mm^3 [72–74]. We will compare prostate cancer localization performance of K^{trans} and k_{ep} derived from two pulse sequences with differing temporal and spatial resolution in this thesis. DCE-MRI results can be confounded by variation in vascular parameters caused by non-cancerous conditions such as prostatic intra-epithelial neoplasia (PIN), which has also demonstrated increased levels of vascular growth factors compared to normal tissue, creating the potential for false positive

cancer findings [65].
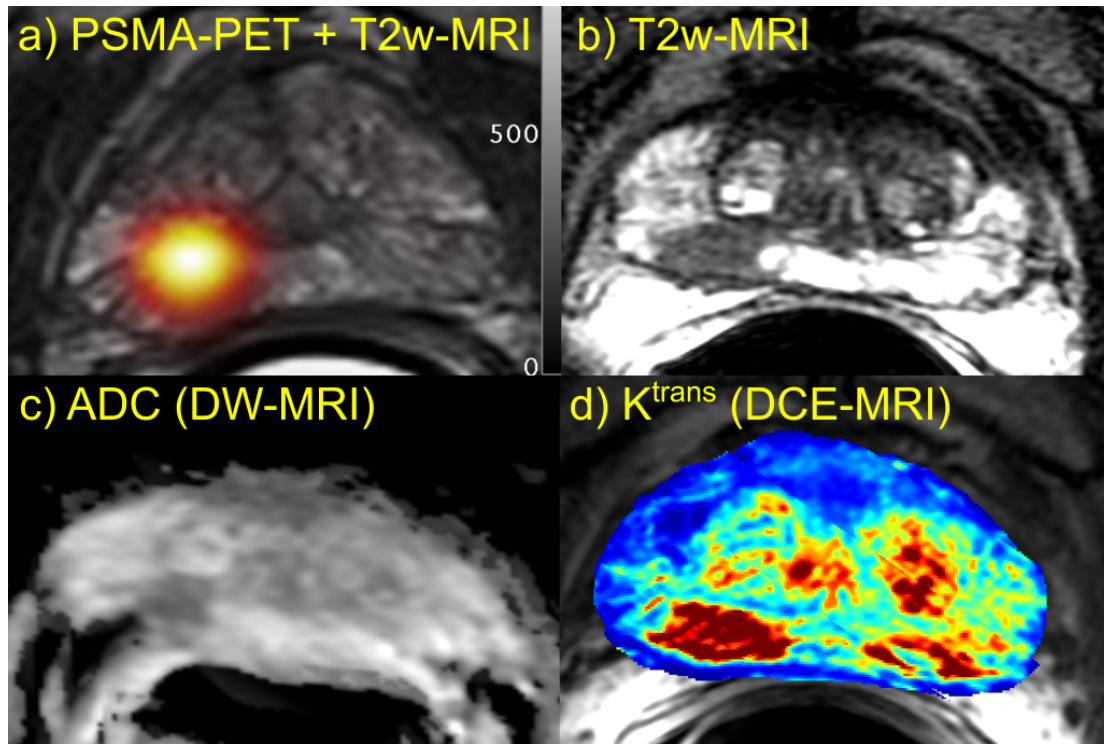
Figure 1.4: a) Example PSMA-PET overlaid T2w-MRI from a prostate cancer patient. b-d) T2w-MRI, ADC derived from DW-MRI, and K^{trans} derived from DCE-MRI from a single prostate cancer patient.

Multi-Parametric MRI

Given the differing mechanisms of contrast generation associated with T2w, DW, and DCE-MRI techniques, consensus guidelines recommend multi-parametric MRI (mpMRI) protocols including all three techniques for optimum prostate cancer localization performance [6, 61]. mpMRI combining T2w, DW, and DCE-MRI has been compared with whole-mount histology [75–78], demonstrating area under the receiver operating characteristic (ROC) curve of 0.71-0.94 for prostate cancer classification [75, 76]. Area under the ROC curve (AUC) values for mpMRI were found to be statistically significantly higher than T2w alone (0.67-0.85), DW alone (0.69-0.90), or DCE-MRI alone (0.59-0.75) when derived from pulse sequences with acquisition times of 10-13

s/image. [75, 76]. Magnetic resonance spectroscopy (MRS) has also been investigated as a component in mpMRI, detecting changes in metabolite concentrations associated with prostate cancer [76]. Due to the low spatial resolution, long scan times, and technical challenges associated with MRS acquisition, T2w+DW+DCE-MRI is increasingly being adopted as the standard components of mpMRI for prostate cancer localization [6]. mpMRI can be used to detect tumours with volumes >0.4 cm^3 and <0.4 cm^3 with sensitivities of 80% and 5% respectively [77], indicating its utility for the detection of clinically-significant tumour volumes >0.5 cm^3 [79] but not sub-clinical spread.

1.4   Prostate Cancer Treatment

Cancer cells tend to have common genotypic and phenotypic qualities that differentiate them from normal tissue cells [12], but selective cancer cell destruction is an ongoing challenge. Treatments can be described qualitatively in terms of therapeutic ratio, referring to the ratio of improvements in patient survival to the severity of treatment side-effects due to normal tissue damage. In accordance with this concept of therapeutic ratio, there are multiple treatment options available to treat prostate cancer with varying degrees of treatment aggressiveness and side-effects that can be selected based on patient-specific risks of mortality, comorbidities, and preferences. The most common curative-intent treatments for prostate cancer are surgery and radiotherapy [80]. These techniques are summarized in the following sections along with results of relevant clinical trials. It should be noted that the results of clinical trials may be subject to factors influencing treatment efficacy such as patient selection bias and clinical trial end-point definitions, such as bDFS.

1.4.1 Surgery

For localized prostate cancer, the standard surgical treatment is radical prostatectomy involving complete removal of the gland. The 5-year bDFS following radical prostatectomy are 80-92%, 66-67%, and 34-50% for low, intermediate, and high-risk patients, respectively [2]. Common toxicities reported 3 years following radical prostatectomy include genitourinary symptoms including incontinence and erectile dysfunction impacting 9% and 42% of patients respectively [81]. Current 10-year follow-up data suggests that radical prostatectomy provides superior cause-specific survival to radiotherapy for intermediate and high-risk patients less than 80 years old [80, 82], but continued superiority of surgery has been disputed based on improvements in radiotherapy achieved in the past 10 years [83]. Radical prostatectomy can be performed using open radical retropubic or robot-assisted laparoscopic techniques with no difference in oncologic or functional outcomes found between techniques [84].

1.4.2 Radiotherapy

Radiotherapy involves the application of ionizing radiation to kill cancer cells. Ionizing radiation is delivered in the form of X-rays produced using x-ray tubes or linear accelerators, emissions produced by radioactive isotopes, or ion beams produced by particle accelerators. Radiation acts to kill cancerous cells through multiple mechanisms depending on the type and amount of radiation delivered, but the primary mechanism for cell-death caused by conventional radiation therapy is deoxyribonucleic acid (DNA) damage [85]. DNA can be damaged by ionizing radiation directly, in which energy is transferred directly from the incident radiation to the DNA itself leading to DNA double strand breaks, or indirectly in which energy is transferred to other molecules to produce reactive chemical species that go on to react with DNA to cause damage [85]. Radiotherapy for prostate cancer can be broadly classified based on whether the radiation source is distant or close to the region to be treated, referred to as external

beam radiotherapy (EBRT) and brachytherapy, respectively.

External Beam Radiotherapy

EBRT involves the exposure of a target to ionizing radiation from a source external to the body. Modern EBRT for prostate cancer typically makes use of X-rays produced by linear accelerators to deliver a prescribed dose. Linear accelerators enable precise orientation and shaping of X-ray beams to deliver a prescribed dose to the prostate while sparing surrounding critical structures. Rotational gantries allow the delivery of beams from multiple angles to minimize entrance and exit dose, and tungsten jaws and multi-leaf-collimators (MLCs) enable beams to be shaped to maximize dose to the target while sparing surrounding tissue. Multiple beams can be combined to create sophisticated dose distributions using planning and delivery techniques such as intensity modulated radiation therapy (IMRT), volumetric modulated arc therapy (VMAT), and helical tomotherapy [86]. Modern linear accelerators incorporate on-board imaging systems for patient alignment, including MV portal imaging, kV projection imaging, CBCT, fan-beam CT, and ultrasound [35]. Furthermore, the ability to create spatially-varying dose distributions allows the use of EBRT to treat the seminal vesicles and pelvic lymph nodes in high-risk patients [87]. The 5-year bDFS following modern EBRT is 85-90%, 70-79%, and 47-55% for low, intermediate, and high-risk patients respectively [2]. Common toxicities reported 5 years following EBRT include genitourinary (e.g. cystitis, hematuria) and rectal toxicities (e.g. proctitis) [17]. Decline in sexual function is also reported, but data are confounded by the frequent use of adjuvant androgen deprivation therapy [17]. Particle accelerators capable of delivering intensity modulated proton therapy (IMPT) are becoming increasingly available. IMPT has been used to treat prostate cancer, potentially enabling higher whole-gland doses than currently possible with photon-based EBRT [4], but is not yet widely available.

Brachytherapy

Brachytherapy, the focus of this thesis, involves bringing a radioactive source in contact with the region to be treated. For the treatment of prostate cancer, this involves inserting one or multiple radioactive seeds into the prostate to deliver a prescribed dose. These seeds may be inserted permanently or temporarily, as in low-dose-rate brachytherapy (LDR-BT) and in high-dose-rate brachytherapy (HDR-BT), respectively.

LDR-BT seeds are placed in the prostate permanently using needles inserted through the perineum, typically containing the radioactive isotope iodine-125 (^{125}I) . ^{125}I primarily undergoes electron capture leading to the release of photons with energy of ~30 keV with a half-life of 59.5 days [88]. LDR-BT needles are typically inserted under TRUS guidance to place seeds into regions of the prostate for whole-gland coverage. A single insertion may involve >80 individual seeds to deliver a prescription dose of 145 Gy [89, 90]. LDR-BT is typically used as whole-gland monotherapy for low-risk patients [89], with one study demonstrating 12-year bDFS following LDR-BT of 91% [91]. The 5-year bDFS following LDR-BT monotherapy is 85-94%, 67-82%, and 52-65% for low, intermediate, and high-risk patients respectively [2]. Results from the ASCENDE-RT clinical trial indicated that LDR-BT combined with EBRT improves disease control for intermediate and high-risk patients combared to EBRT alone [92]. Common toxicities following LDR-BT include urethral obstruction, incontinence, and decline in sexual function impacting 10%, 7%, and 26% of patients, respectively [17].

HDR-BT for prostate cancer involves the temporary insertion of a single high-activity radioactive seed, typically containing iridium-192 (^{192}Ir), into the prostate using hollow needles inserted through the perineum and guided by a rigid template. ^{192}Ir primarily undergoes β^- decay leading to the release of photons with energy of ~0.3 MeV with a half-life of 73.8 days [88]. HDR-BT insertions typically involve 15-20 needles which are all inserted, locked into place, and imaged for final localization relative to anatomy. The locations of needles, prostate, urethra, bladder, and rectum are digitized

and used to optimize the amount of time that the single radioactive source will spend at each position within each needle to deliver a conformal dose. Once these dwell times are determined, they are transferred to a remote after-loader containing the radioactive source attached to the end of a cable. The remote after-loader passes the radioactive source through tubes to positions within each needle for the specified lengths of time to deliver the treatment in 10-20 minutes. Conventional HDR-BT targeting the whole prostate is a routine treatment technique when used as a 15 Gy single fraction dose boost to EBRT primarily for intermediate and high-risk patients [93, 94]. The 5-year bDFS following whole-gland EBRT+HDR-BT boost is 80-98%, 59-96%, and 34-85% for low, intermediate, and high-risk patients respectively [3]. Common toxicities reported with EBRT+HDR-BT boost include genitourinary and rectal toxicities impacting up to 7.7% and 2.8% of patients, respectively [3]. HDR-BT monotherapy has also been proposed, and a recent study indicated that 5-year bDFS following HDR-BT monotherapy is 93%, and 81% for intermediate and high-risk patients, respectively [95].

treatment	low-risk	intermediate-risk	high-risk	ref.
surgery	80-92	66-67	34-50	[2]
EBRT	85-90	70-79	47-55	[2]
LDR-BT monotherapy	85-94	67-82	52-65	[2]
EBRT+HDR-BT boost	80-98	59-96	34-85	[3]

Table 1.2: 5-year biochemical disease-free survival (bDFS) rates (%) associated with treatments for prostate cancer, stratified by patient risk groups. Ranges in values indicate variations across clinical trials included in the cited review articles.

1.5 Current Challenges in Prostate Cancer Radiotherapy

Modern radiotherapy techniques for prostate cancer enable image-guidance and sophisticated spatially-varying dose distributions; however, the competing objectives of

decreasing rates of recurrence while minimizing treatment toxicity represent ongoing challenges.

1.5.1   Rates of Prostate Cancer Recurrence

As outlined in Table 1.2, rates of biochemical recurrence 5 years following treatment remain 4-34% and 15-66% for intermediate and high-risk patients, respectively. Biochemical recurrence is an accepted precursor to prostate cancer metastasis and mortality [96], and rates of cancer-specific mortality 10 years following surgery *versus* radiotherapy are 1.4% *versus* 3.9% and 6.8% *versus* 11.5% for intermediate and high-risk patients, respectively [82]. While there currently appears to be an advantage in cause-specific survival for patients receiving surgery, advances in dose-escalated conformal radiotherapy may lead to benefits over surgery for intermediate and high-risk patients. Clinical trials have indicated that 5-year bDFS is improved from 60% to 71% by increasing EBRT dose from 64 Gy to 74 Gy [17], and is improved further from 74% to 82% by increasing dose from 70 Gy to 86 Gy [97]. A randomized clinical trial demonstrated that augmenting EBRT with a HDR-BT boost led to 5-year bDFS of 75% compared to 61% for EBRT alone [98].

1.5.2   Limitations of Whole-Gland Dose-Escalation

While increasing dose to the whole prostate has demonstrated benefits in bDFS, whole-gland EBRT doses of 64 Gy, 74 Gy, and 86 Gy are associated with rates of grade 2 genitourinary toxicity (e.g. frequent urination, pain) [99] of 8%, 11%, and 22%, respectively [17, 18]. Evidence also suggests that escalating HDR-BT dose reduces risk of biochemical recurrence [100]; however, whole-gland HDR-BT monotherapy dose is limited by grade 3 genitourinary toxicities (e.g. hematuria, severe pain), which increase in frequency at doses of 20 Gy in one fraction [19].

1.6 Motivation for Tumour-Targeted HDR Brachytherapy

Radiotherapy techniques enabling targeted dose-escalation to the site of the largest highest-grade pre-treatment lesion, referred to as the dominant index lesion (DIL), may lead to decreased rates of recurrence in intermediate and high-risk prostate cancer patients while preserving acceptable rates of treatment toxicity, and HDR-BT may be the ideal modality to deliver these tumour-targeted treatments. This clinical hypothesis is justified as follows.

1.6.1 Sites of Prostate Cancer Recurrence

The site of prostate cancer recurrence following radiotherapy tends to be the site of the pre-treatment DIL [101, 102]. Pucar et al. demonstrated that the site of local recurrence following EBRT was the site of the pre-treatment DIL in 9 out of 9 patients who underwent pre-EBRT MRI and salvage prostatectomy [101]. Arrayeh et al. demonstrated the same findings in 8 out of 9 patients who underwent pre-EBRT MRI and follow-up MRI after experiencing biochemical recurrence [102]. This pattern of recurrence suggests that escalating dose to the site of the DIL may lead to decreased risk of recurrence.

1.6.2 Previous Work Escalating Dose to Prostate Tumours

The clinical hypothesis that prostate tumour-targeted dose-escalation improves survival has been investigated in multiple clinical trials making use of varying target volume definition and treatment delivery techniques. The review articles by Bauman et al. and von Eyben et al. provide summaries of clinical trials investigating prostate tumour targeted dose-escalation [103, 104]. Of the 16 studies identified in the reviews, 13 used MRI, two used SPECT, and one used PET for prostate tumour localization and target volume delineation. Two studies used mpMRI incorporating T2w+DW+DCE-

MRI [105, 106]. In terms of treatment modality, 10 studies used EBRT, three studies used EBRT+HDR-BT boost, one study used EBRT+LDR-BT boost, and two studies used LDR-BT monotherapy. Two additional recently reported trials investigated EBRT+HDR-BT boost with mpMRI for tumour localization [59, 107].

Of the five studies investigating tumour-targeted HDR-BT dose boosts [59, 106–109], all used MRI for tumour localization, two performed MRI-guided HDR-BT with open-bore MRI scanners [108, 109], one performed CT-guided HDR-BT [107], one performed AR3D TRUS-guided HDR-BT [106], and one performed SR3D TRUS-guided HDR-BT [59]. Both of the 3D TRUS-guided studies made use of rigid registrations between pre-operative mpMRI and intra-operative 3D TRUS for treatment planning, and did not incorporate planning target volume (PTV) expansions to account for DIL localization or treatment delivery uncertainties [59, 106]. Both of the 3D TRUS-guided studies also made use of mpMRI combining T2w+DW+DCE-MRI for tumour localization. Meta-analysis of the reviewed studies indicated that tumour-targeted treatments incorporating brachytherapy boosts enabled significantly higher dose to the DIL than the EBRT based approaches [104].

1.6.3 Setup Uncertainties and Intra-Treatment Prostate Motion

External Beam Radiotherapy

Modern image-guidance techniques for EBRT include portal imaging, CBCT, fan-beam CT, and ultrasound [35]. Markers can be inserted into the prostate to provide additional tracking information including electromagnetic tracking devices [110] and gold fiducial markers [111]. Despite the use of these image-guidance techniques, setup error for prostate EBRT due to intra-fraction prostate motion has been measured to be 4 mm [111]. The ongoing FLAME trial, investigating prostate tumour-targeted EBRT, incorporated planning target volume (PTV) expansions of 4 mm to account for these setup uncertainties [112]. Hybrid linear accelerator/MRI scanners are becoming increasingly

available, which may reduce EBRT setup uncertainty for prostate treatments through improved soft-tissue motion tracking [113].

Brachytherapy

By bringing radiation sources in contact with the targets to be treated, brachytherapy techniques reduce setup uncertainty and intra-treatment prostate motion compared to EBRT techniques. Uncertainty is reduced by: 1) mitigating motion between the source and target, and 2) enabling the source and target to be imaged in the same field of view.

LDR Brachytherapy   Modern LDR-BT makes use of TRUS to place seeds in the prostate while the patient is immobilized leading to low setup uncertainty during insertion. CT or MRI are used for post-implant seed localization [114]. Post-implant CT and MRI provide LDR-BT seed positions with mean inter-observer variability of 1.1 mm and 3.0 mm respectively [37].

HDR Brachytherapy   The single HDR-BT radiation source is constrained within needle trajectories, and CT, MRI, or TRUS imaging is used to localize needles in their final positions following insertion [36, 43, 57, 115]. For treatment planning and delivery, discrete source positions within each needle are placed relative to the needle tip. Accordingly, the primary component in HDR-BT setup uncertainty is in localizing needle tip positions relative to anatomy. A major focus of this thesis is to reduce this source of uncertainty in HDR-BT.

Fractionated HDR Brachytherapy: Reposition Patient Between Imaging and Treatment   Typically, fractionated HDR-BT involves implanting needles followed by treatment fractions over multiple days during which time the needles remain *in situ*. Fractionated HDR-BT requires relocating the patient between treatment fractions, and potentially between imaging and treatment within fractions [116]. Comparison between

needle tip positions and gold fiducial marker seeds in fractionated CT-guided HDR-BT demonstrated mean±SD inferior tip shifts of 6±4 mm and 12±6 mm at the time of the second and third fractions, respectively [117]. Edema leading to changes in prostate volume between treatment fractions can introduce additional uncertainty [116].

Single Fraction HDR Brachytherapy: Reposition Patient Between Imaging and Treatment   Single fraction CT and MRI-guided HDR-BT requires patient repositioning between imaging and treatment in instances when the imaging suite is not sufficiently shielded for the energy and activity of the HDR-BT radiation source [93, 108]. Holly et al. investigated the shifts in needle tip position between CT imaging and treatment for single fraction HDR-BT using repeated CBCT, and found mean needle tip shifts of 11 mm, and shifts >20 mm in 10% of needles [115]. It is reasonable to expect similar needle shifts for MRI-guided procedures requiring patient relocation.

Single Fraction HDR Brachytherapy: Stationary Patient   Single fraction HDR-BT that does not involve patient repositioning between imaging and treatment eliminates a major component of setup uncertainty. In-bore CT-guided HDR-BT may be performed, with needle tip localization uncertainty limited by CT slice thickness, typically 1-3 mm [93, 118]. In-bore MRI-guided HDR-BT has also been implemented [57, 119], but requires extensive imaging suite modification to facilitate both the MRI scanner and HDR-BT radiation source [120]. In-bore CT and MRI-guided treatments constrain patient position, potentially limiting access to the perineum and increasing pubic arch interference [121].

TRUS-guided HDR-BT has also been implemented, involving the localization of needles using 3D TRUS images [5, 43, 122]. TRUS-guidance allows the HDR-BT insertion, imaging, treatment planning, and delivery to be completed in existing brachytherapy bunkers, and enables unrestricted patient positioning to access the perineum and to mitigate pubic arch interference [43]. Treatment plan comparisons indicate TRUS-

guided HDR-BT can provide equivalent dosimetric characteristics to high-resolution CT-guided HDR-BT [123], suggesting that TRUS-guidance may be an optimal modality for HDR-BT image-guidance due to improved patient positioning and the ability to deliver treatments in existing brachytherapy bunkers. TRUS-guided HDR-BT also allows the use of pre-operative mpMRI for treatment planning through intra-operative image registration [124].

1.6.4   Dosimetric Characteristics

Through treatment planning simulations, it was shown that HDR-BT can deliver a whole-gland prescription dose with decreased dose to surrounding organs when compared to IMRT, intensity modulated proton therapy (IMPT), intensity modulated carbon-ion therapy (IMCT), and LDR-BT [4]. In terms of dosimetric accuracy, whole-gland LDR-BT and HDR-BT can provide uncertainties in dose to the prostate of 11% and 5% , respectively [114]. Lower uncertainty in HDR-BT is primarily attributed to decreased source position uncertainty in optimized single-fraction workflows assuming needle-tip localization uncertainty of 0.7 mm [114], which has been demonstrated in phantoms with TRUS-guidance augmented with calibrated needle end-length measurements [125]. Finally, hypo-fractionated treatments delivered using HDR-BT have been well-tolerated in intermediate and high-risk prostate cancer patients, with multiple centers reporting acceptable acute toxicities at 3-month follow-up when delivering 19 Gy in one fraction [19, 126].

1.6.5   Summary of Motivation for Tumour-Targeted HDR-BT

Prostate cancer tends to recur at the site of the pre-treatment DIL following radiotherapy [101, 102]. Prostate tumour-targeted dose escalation is under active investigation, with evidence suggesting that brachytherapy boosts provide higher DIL dose than EBRT techniques [4, 104]. Single-fraction TRUS-guided HDR-BT mitigates setup un-

certainty leading to decreased dosimetric uncertainty relative to LDR-BT [114], and preliminary evidence suggests the feasibility of dose-escalated single-fraction HDR-BT up to 19 Gy for whole-gland treatments [19, 126]. Two trials have investigated 3D TRUS-guided tumour-targeted HDR-BT with co-registered mpMRI for tumour localization [59, 106]. The objective of the work in this thesis is to translate and evaluate imaging tools for implementation in analogous clinical trials with improved accuracy in prostat tumour localization [78] and needle tip localization [5].

1.7 Challenges for Tumour-Targeted HDR Brachytherapy

1.7.1 Imaging for Needle Tip Localization

Tumour-targeted HDR-BT dosimetry is critically sensitive to uncertainty in needle tip positions relative to anatomy [45]. For whole-gland treatments, Tiong et al. recommend needle tip localization uncertainty within 3 mm for relative tumour control probability of 95% [127], and Kirisits et al. recommend needle tip localization accuracy within 0.7 mm for overall dosimetric uncertainty of 5% [114]. This sensitivity to uncertainty increases for tumour-targeted treatments. Mason et al. demonstrated that a systematic shift of HDR-BT needle tips by 2 mm leads to mean decreases in the dose delivered to 90% of the target volume (D90%) of 0.7% and 8.3% in whole-gland and tumour-targeted treatment plans, respectively [128]. Decrease in target coverage may degrade tumour-targeted treatment efficacy, as decreased prostate D90% has been found to be a predictor of biochemical relapse in patients receiving whole-gland EBRT+HDR-BT boost [129].

For single-fraction HDR-BT involving a stationary patient for imaging and treatment, HDR-BT needle tip localization accuracy depends on the modality used for

image-guidance. AR3D TRUS for HDR-BT is commercially available; however, the spatial resolution of AR3D images in the needle insertion (superior/inferior) direction is limited by the axial transducer's elevational resolution, measured to be up to 4 mm at a distance of 78 mm from the transducer [46]. Therefore, AR3D TRUS is typically augmented with live-2D sagittal TRUS acquired at the time of needle insertion. 2D sagittal TRUS has sub-millimeter spatial resolution in the needle insertion direction leading to tip localization uncertainty <1 mm [45]. Probe motion required for AR3D acquisition, as indicated in Figure 1.3a, has the potential to introduce anatomical motion that could lead to systematic shifts in needle tip positions. Finally, the TRUS probe also must be moved to combine live-2D sagittal imaging for needle tip identification with AR3D images, introducing another potential source of prostate motion. Despite these limitations, AR3D TRUS has been used in a recently reported tumour-targeted HDR-BT study [106]. Implementing and characterizing 3D TRUS techniques for improved HDR-BT needle tip localization accuracy is the first focus of this thesis.

1.7.2   Image Processing To Reduce HDR-BT Treatment Time

Patients are often placed under general anesthesia for the duration of single-fraction HDR-BT procedures including needle insertion, imaging, treatment planning, and delivery. Increasing the complexity of HDR-BT workflows for tumour-targeted treatment planning may add time to the procedure, and tools that reduce the time required for manual image analysis may be required to mitigate the risks of anesthesia [130]. Automating the localization of needles following insertion may be an effective approach to reduce the time required for TRUS-guided HDR-BT, increasing the feasibility of tumour-targeted HDR-BT.

Existing automatic needle segmentation algorithms have not been designed to handle images containing multiple needles with inter-needle spacing ~5 mm as required for HDR-BT [131–144]. Typical HDR-BT insertion templates have holes spaced 5 mm

apart, and needle deflection beyond the template can lead to adjacent needle spacing <5 mm within the patient [145]. The application of existing algorithms designed primarily for prostate biopsy to images containing multiple needles would require manual cropping of regions containing a single needle each, which is not feasible for HDR-BT insertions containing 15-20 needles. Needle deflection between the insertion template and prostate also makes template-based image cropping infeasible [145]. An algorithm is required to overcome these limitations, enabling the segmentation of all needles in an HDR-BT insertion using a single SR3D image. Implementing and validating such an algorithm is the second focus of this thesis.

1.7.3   Imaging for Tumour Localization

Tumour-targeted HDR-BT depends critically on accurate DIL localization in the intra-operative image space for treatment planning. Currently, the recommended imaging technique for DIL detection and localization is mpMRI [6, 61], which is used in the majority of ongoing tumour-targeted dose-escalation studies [103, 104]. In the case of MRI-guided HDR-BT, it is possible to acquire mpMRI during treatment for tumour localization, but this requires an MR compatible operating room. In the case of CT or TRUS-guided HDR-BT, mpMRI must be acquired prior to treatment and registered to the intra-operative image-set. Deformable registration of MRI of the prostate with CT and SR3D TRUS has been investigated and assessed *in vivo*, demonstrating target-registration-errors of 1.9 and 2.0 mm respectively when using advanced registration techniques [124, 146]. mpMRI can be used to define clinical target volumes (CTVs) reliably encompassing 95% of high-grade cancer by adding a 6 mm isotropic margin to the gross tumour volume (GTV) visible on mpMRI [78]. As previously noted, two recent trials investigating tumour-targeted HDR-BT made use of mpMRI incorporating T2w+DW+DCE-MRI for tumour localization [59, 106].

MRI involves an inherent trade-off between the amount of time required to acquire

each image and the resultant spatial resolution and SNR. This trade-off is critical to DCE-MRI, since identification of heterogeneous tumour vasculature may require high-spatial resolution [147], but current mpMRI guidelines recommend DCE-MRI acquisition times of ≤7 s/image for differentiation between contrast agent uptake rates in cancerous and normal tissues [6]. Recent simulation studies have demonstrated insensitivity of prostate cancer localization performance using DCE-MRI to image acquisition times from 1.4-15 s/image [72], creating the potential for improved prostate cancer localization performance through improved spatial resolution achievable at longer acquisition times [73]. Direct comparisons of DCE-MRI pulse sequences emphasizing high spatial and temporal resolutions are required to determine optimal parameters for prostate cancer localization. Comparing DCE-MRI parameters derived from two pulse sequences to whole-mount histology to assess relative cancer localization performance is the final focus of this thesis.

1.8 Previous Work Addressing Challenges for Tumour-Targeted HDR Brachytherapy

1.8.1 Techniques for HDR-BT Needle Tip Localization

CT provides high needle-to-tissue contrast and high spatial accuracy, but limited soft tissue contrast for prostate and urethra localization [38]. MRI provides high spatial-resolution and high soft tissue contrast, but is susceptible to geometric distortion caused by interventional devices [148]. As mentioned previously, in-bore treatments may decrease access to the perineum and increase pubic arch interference.

Comparisons between HDR-BT needle tip positions identified using commercially available AR3D TRUS and CBCT images for single-fraction treatments have indicated needle tip position differences within 3 mm for 97% of needles *in vivo*; however, this

validation required a registration between the TRUS and CBCT images by aligning a reference needle tip visible in both images [5]. This registration eliminates the ability to measure absolute needle tip positions and assess uncertainty relative to anatomy. Mean needle tip localization accuracy of 0.7 mm has been demonstrated in phantoms using AR3D TRUS-guidance augmented with measurements of needle end-lengths protruding from the insertion template and related back to the image coordinates using a pre-treatment calibration, but has not been demonstrated *in vivo* [125]. All TRUS techniques can suffer from shadow artifacts caused by complete attenuation of signal by air bubbles, calcifications, or the HDR-BT needles themselves. Even et al. have proposed augmenting AR3D TRUS-guidance with CBCT to overcome current limitations, leading to a potentially optimal trade-off between the needle-to-tissue contrast provided by CT and the soft tissue contrast provided by TRUS [122].

SR3D TRUS preserves sub-millimeter spatial resolution in the needle insertion direction, and eliminates the need to step the probe in the superior/inferior direction, mitigating the potential for anatomical motion as indicated in Figure 1.3b [47]. A custom mechatronic device has been developed by our group enabling SR3D image acquisition for transperineal-guided procedures shown in Figure 1.2 [49], and was previously validated in phantoms for LDR-BT guidance involving the insertion of a single needle at a time [149]. Major vendors including Varian Medical Systems (Palo Alto, CA) and Elekta (Stockholm, SE) offer devices and software with similar SR3D reconstruction capabilities. SR3D imaging has the potential to significantly reduce the uncertainty in HDR-BT needle tip localization, but has not been fully validated for this purpose *in vivo*. Despite uncertainty in true HDR-BT needle tip localization accuracy of SR3D TRUS, it has been employed in a recent tumour-targeted HDR-BT study [59]. SR3D TRUS for HDR-BT needle tip localization is implemented and characterized in this thesis.

Electromagnetic (EM) tracking techniques have also been proposed for HDR-BT

needle tip localization, demonstrating tip localization error of <1 mm [150, 151]. EM tracking systems for needle tip localization still require intra-operative imaging to localize anatomy, and EM tracking coordinate systems must be registered to *in vivo* image coordinate systems for treatment planning.

1.8.2   Automatic Needle Segmentation using 3D TRUS

Investigators have proposed line-detection algorithms to segment single needles in 3D ultrasound images. Ding et al. proposed constructing orthogonal 2D projections of the image followed by two 2D line-fitting steps for the identification of straight needles [134], which was extended to the identification of curved needles [131]. Barva et al. employed a parallel integral projection (PIP) to project feature points onto oriented 2D planes using a hierarchical mesh-grid algorithm until a peak corresponding to the most likely trajectory was identified [132]. The 3D Hough transform (3DHT) describes transformations from 3D image coordinates to line parameters. By exploring ranges of 3DHT parameter values either systematically [137, 138] or randomly [139, 144, 152] and calculating the number of feature point inliers corresponding to each set of parameters, the most likely line in 3D space is given by the parameters with the largest number of feature point inliers. Novotny et al. [137] describe this class of line detection methods using the generalized Radon transform [135], enabling extension to more complex line parameterizations such as Bezier curves for the identification of curved needles [136].

All of these methods depend on classification of voxels as needle feature points or background based on either filtered intensity [132, 138], local morphology metrics such as gradient magnitude or phase [139, 140, 143], or temporal information caused by needle manipulation [133]. Random sample consensus (RANSAC) algorithms are similar to the generalized Radon transform techniques, but iteratively update a line trajectory location and corresponding set of feature points by modeling voxel intensities

as a function of both intensity and distance from the line using analytical probability distributions [141] or supervised machine learning algorithms [142]. While these line detection algorithms have shown promise for specific image-guidance tasks, they have not been been validated using SR3D TRUS images containing multiple needles like those acquired for HDR-BT treatment planning. The 3DHT may be augmented with additional regularization steps enabling adjacent needles to be distinguished from one another. This approach is implemented and characterized in this thesis.

1.8.3   Spatial *versus* Temporal Resolution of DCE-MRI

Aerts et al. performed temporal frequency analysis of the two-compartment pharmacokinetic model used for DCE-MRI analysis, and demonstrated that image acquisition times >10 s/image led to aliasing of high temporal frequency components in the contrast-agent *versus* time curves leading to increased noise in the resultant K^{trans} and k_{ep} values [153]. Alternatively, Ream et al. temporally down-sampled DCE-MRI acquired at 1.4 s/image to 15 s/image and did not observed a change in prostate cancer localization performance over this range of simulated acquisition times [72]. Investigators have also proposed the use of non-parametric models such as washout gradient (WG) [154] and the three time point (3TP) method [155] involving the analysis of only three images acquired minutes apart. DCE-MRI analysis methods applicable to images with longer acquisition times may enable improvements in prostate cancer localization performance through improved DCE-MRI spatial resolution; however, this potential benefit can only be assessed fully through MR imaging with longer acquisition times. T1w pulse sequences for DCE-MRI with acquisition times of 6.4 s/image and 92.5 s/image are implemented and compared in this thesis.

1.9   Summary

Prostate cancer remains the second leading cause of cancer-related death in developed countries [1]. Radiotherapy for prostate cancer improves local control, but evidence of recurrence recurrence 5 years following treatment remains 4-41% for patients with localized disease[2, 3], and whole-gland treatment aggressiveness is currently limited by toxicities. HDR-BT is an image-guided radiotherapy technique for prostate cancer with lower setup uncertainty and lower dose to surrounding organs relative to other radiotherapy techniques [4, 114], and is well-tolerated when delivering single fraction doses up to 19 Gy to the whole prostate [19, 126]. TRUS-guided single-fraction HDR-BT enables unparalleled access to the perineum without requiring relocation of the patient for imaging, and shows promise for enabling time-efficient and accurate HDR-BT in existing brachytherapy bunkers [43]. mpMRI makes use of multiple mechanisms of image contrast to localize prostate tumours [6, 61]. mpMRI may be combined with TRUS-guided HDR-BT using existing deformable image registration techniques [124], enabling tumour-targeted HDR-BT. Tumour-targeted HDR-BT has the potential to improve the therapeutic ratio of prostate cancer radiotherapy by improving local control without increasing treatment toxicities, but the efficacy of these treatments depends on the ability to: 1) accurately localize HDR-BT needles using 3D TRUS to minimize dosimetric uncertainty for treating prostate sub-volumes, 2) efficiently localize HDR-BT needles using 3D TRUS for intra-operative implementation, and 3) accurately localize prostate tumours using mpMRI.

1.10   Specific Objectives

The work in this thesis is motivated by the long-term clinical goal of decreasing rates of prostate cancer recurrence through tumour-targeted HDR-BT. Tumour-targeted HDR-BT accuracy and efficiency may be improved through increased needle localization accuracy using SR3D TRUS, increased needle localization efficiency using an automatic segmentation algorithm, and selection of optimal DCE-MRI pulse sequence parameters in terms of temporal and spatial resolution. To this end, the specific objectives of Chapters 2-5 are:

Chapter 2 To implement and characterize manual HDR-BT needle segmentation using SR3D TRUS, and to compare accuracy with clinically standard AR3D TRUS.

Chapter 3 To implement and validate an automatic needle segmentation algorithm enabling the localization of multiple needle trajectories and tips in an HDR-BT insertion.

Chapter 4 To overcome limitations in needle tip localization accuracy using SR3D TRUS identified in Chapters 2 and 3 that would inhibit clinical implementation of SR3D-guided HDR-BT.

Chapter 5 To compare prostate tumour localization accuracy using parameters derived from DCE-MRI acquired using two pulse sequences designed to highlight the inherent trade-off in MRI temporal and spatial resolution.

References

1. Torre, L. A. *et al.* Global cancer statistics, 2012. *CA Cancer Journal for Clinicians* **65,** 87–108 (2015).

2. Peschel, R. E. & Colberg, J. W. Surgery, brachytherapy, and external-beam radiotherapy for early prostate cancer. *Lancet Oncology* **4,** 233–241 (2003).

3. Zaorsky, N. G. *et al.* High dose rate brachytherapy boost for prostate cancer: A systematic review. *Cancer treatment reviews* **40,** 414–425 (2014).

4. Georg, D. *et al.* Dosimetric considerations to determine the optimal technique for localized prostate cancer among external photon, proton, or carbon-ion therapy and high-dose-rate or low-dose-rate brachytherapy. *International Journal of Radiation Oncology Biology Physics* **88,** 715–722 (2014).

5. Batchelar, D. *et al.* Validation study of ultrasound-based high-dose-rate prostate brachytherapy planning compared with CT-based planning. *Brachytherapy* **13,** 75–79 (2014).

6. Weinreb, J. C. *et al.* PI-RADS Prostate Imaging - Reporting and Data System: 2015, Version 2. *European Urology* **69,** 16–40 (2016).

7. Statistics Canada. Canadian Cancer Statistics 2016. *Canadian Cancer Society,* 1–132 (2016).

8. Siegel, R., Miller, K. & Jemal, A. Cancer statistics, 2016. *CA Cancer Journal for Clinicians* **66,** 7–30 (2016).

9. Drake, R. L., Vogl, A. W. & Mitchell, A. W. *Gray's Anatomy for Students* 3rd ed., 473 (Churchill Livingstone, 2015).

10. Silverthorn, D. U. *Human Physiology: An Integrated Approach* 7th ed., 805–815 (Pearson Education Inc., 2016).

11. Epstein, J. I., Allsbrook, W. C. J., Amin, M. B. & Egevad, L. L. The 2005 International Society of Urological Pathology (ISUP) Consensus Conference on Gleason Grading of Prostatic Carcinoma. *The American Journal of Surgical Pathology* **29,** 1228–1242 (2005).

12. Hanahan, D. & Weinberg, R. A. Hallmarks of cancer: The next generation. *Cell* **144,** 646–674 (2011).

13. Feldman, B. J. & Feldman, D. The development of androgen-independent prostate cancer. *Nature Reviews. Cancer* **1,** 34–45 (2001).

14. Pond, G. R. *et al.* The prognostic importance of metastatic site in men with metastatic castration-resistant prostate cancer. *European Urology* **65,** 3–6 (2014).

15. Beemsterboer, P. M., de Koning, H. J., Birnie, E., van der Maas, P. J. & Schroder, F. H. Advanced prostate cancer: course, care, and cost implications. *Prostate* **40,** 97–104 (1999).

16. Reeve, B. B. *et al.* Impact of diagnosis and treatment of clinically localized prostate cancer on health-related quality of life for older Americans: A population-based study. *Cancer* **118,** 5679–5687 (2012).

17. Dearnaley, D. P. *et al.* Escalated-dose versus standard-dose conformal radiotherapy in prostate cancer: first results from the MRC RT01 randomised controlled trial. *Lancet Oncology* **8,** 475–487 (2007).

18. Cahlon, O. *et al.* Ultra-high dose (86.4 Gy) IMRT for localized prostate cancer: toxicity and biochemical outcomes. *International Journal of Radiation Oncology Biology Physics* **71,** 330–337 (2008).

19. Hoskin, P. *et al.* High-dose-rate brachytherapy alone given as two or one fraction to patients for locally advanced prostate cancer: acute toxicity. *Radiotherapy and Oncology* **110,** 268–271 (2014).

20. Mohler, J. L. *et al.* Prostate Cancer, Version 2.2014 Clinical Practice Guidelines in Oncology. *Journal of the National Comprehensive Cancer Network* **12,** 686–718 (2014).

21. Catalona, W. J. *et al.* Comparison of digital rectal examination and serum prostate specific antigen in the early detection of prostate cancer: results of a multicenter clinical trial of 6,630 men. *The Journal of Urology* **197,** 1283–1290 (1994).

22. Stamey, T. A. *et al.* Prostate-specific antigen as a serum marker for adenocarcinoma of the prostate. *The New England Journal of Medicine* **317,** 909–916 (1987).

23. Rao, A. R., Motiwala, H. G. & Karim, O. M. A. The discovery of prostate-specific antigen. *BJU International* **101,** 5–10 (2008).

24. Moyer, V. Screening for Prostate Cancer: US Preventive Services Task force Recommendation Statement. *Annals of Internal Medicine* **157,** 120–134 (2012).

25. Roach, M. *et al.* Defining biochemical failure following radiotherapy with or without hormonal therapy in men with clinically localized prostate cancer: Recommendations of the RTOG-ASTRO Phoenix Consensus Conference. *International Journal of Radiation Oncology Biology Physics* **65,** 965–974 (2006).

26. Stephenson, A. J. *et al.* Defining biochemical recurrence of prostate cancer after radical prostatectomy: A proposal for a standardized definition. *Journal of Clinical Oncology* **24,** 3973–3978 (2006).

27. Scher, H. I. *et al.* Eligibility and outcomes reporting guidelines for clinical trials for patients in the state of a rising prostate-specific antigen: recommendations from the Prostate-Specific Antigen Working Group. *Journal of Clinical Oncology* **22,** 537–556 (2004).

28. Pepe, P. *et al.* Prediction by quantitative histology of pathological stage in prostate cancer. *European Journal of Surgical Oncology* **31,** 309–313 (2005).

29. D'Amico, A. V. *et al.* Biochemical outcome after radical prostatectomy, external beam radiation therapy, or interstitial radiation therapy for clinically localized prostate cancer. *Journal of the American Medical Association* **280,** 969–74 (1998).

30. Schröder, F. H. *et al.* Screening and prostate-cancer mortality in a randomized European study. *The New England Journal of Medicine* **360,** 1320–1328 (2009).

31. Rabbani, F., Stroumbakis, N., Kava, B. R., Cookson, M. S. & Fair, W. R. Incidence and clinical significance of false-negative sextant prostate biopsies. *Journal of Urology* **159,** 1247–1250 (1998).

32. Cool, D. W. *et al.* Fusion of MRI to 3D TRUS for mechanically-assisted targeted prostate biopsy: system design and initial clinical experience. *Prostate Cancer Imaging* **6963,** 121–133 (2011).

33. Velez, E. *et al.* Pathologic correlation of transperineal in-bore 3-Tesla magnetic resonance imaging-guided prostate biopsy samples with radical prostatectomy specimen. *Abdominal Radiology, in Press* (2017).

34. Seco, J. & Evans, P. M. Assessing the effect of electron density in photon dose calculations. *Medical Physics* **33,** 540–552 (2006).

35. Yartsev, S. & Bauman, G. Target margins in radiotherapy of prostate cancer. *British Journal of Radiology* **89** (2016).

36. Kolotas, C., Baltas, D. & Zamboglou, N. CT-based interstitial HDR brachytherapy. *Strahlentherapie und Onkologie* **175,** 419–427 (1999).

37. De Brabandere, M. *et al.* CT- and MRI-based seed localization in postimplant evaluation after prostate brachytherapy. *Brachytherapy* **12,** 580–588 (2013).

38. Rasch, C. *et al.* Definition of the prostate in CT and MRI: A multi-observer study. *International Journal of Radiation Oncology Biology Physics* **43,** 57–66 (1999).

39. Marko, J., Gould, C. F., Bonavia, G. H. & Wolfman, D. J. State-of-the-art imaging of prostate cancer. *Urologic Oncology: Seminars and Original Investigations* **34,** 134–146 (2016).

40. Korporaal, J. G., van Vulpen, M., van den Berg, C. a. T. & van der Heide, U. a. Tracer kinetic model selection for dynamic contrast-enhanced computed tomography imaging of prostate cancer. *Investigative Radiology* **47,** 41–48 (2012).

41. Hu, N., Downey, D. B., Fenster, A. & Ladak, H. M. Prostate boundary segmentation from 3D ultrasound images. *Medical Physics* **30,** 1648–1659 (2003).

42. Li, M. *et al.* A comparative assessment of prostate positioning guided by three-dimensional ultrasound and cone beam CT. *Radiation Oncology* **10** (2015).

43. Morton, G. C. Prostate high-dose-rate brachytherapy: Transrectal ultrasound based planning, a technical note. *Practical Radiation Oncology* **5,** 238–240 (2015).

44. Clements, R. The role of transrectal ultrasound in diagnosing prostate cancer. *Current Urology Reports* **3,** 194–200 (2002).

45. Siebert, F.-A. A., Hirt, M., Niehoff, P. & Kovács, G. Imaging of implant needles for real-time HDR-brachytherapy prostate treatment using biplane ultrasound transducers. *Medical Physics* **36,** 3406–3412 (2009).

46. Peikari, M. *et al.* Characterization of ultrasound elevation beamwidth artifacts for prostate brachytherapy needle insertion. *Medical Physics* **39,** 246–256 (2012).

47. Tong, S., Downey, D. B., Cardinal, H. N. & Fenster, A. A three-dimensional ultrasound prostate imaging system. *Ultrasound in Medicine and Biology* **22,** 735–746 (1996).

48. Schmid, M. *et al.* A phantom study to assess accuracy of needle identification in real-time planning of ultrasound-guided high-dose-rate prostate implants. *Brachytherapy* **12,** 56–64 (2013).

49. Bax, J. *et al.* A compact mechatronic system for 3D ultrasound guided prostate interventions. *Medical Physics* **38,** 1055–1069 (2011).

50. Yu, C. Y., Desai, B., Ji, L., Groshen, S. & Jadvar, H. Comparative performance of PET tracers in biochemical recurrence of prostate cancer: A critical analysis of literature. *American Journal of Nuclear Medicine and Molecular Imaging* **4,** 580–601 (2014).

51. Afshar-Oromieh, A., Haberkorn, U., Eder, M., Eisenhut, M. & Zechmann, C. M. [68Ga]Gallium-labelled PSMA ligand as superior PET tracer for the diagnosis of prostate cancer: comparison with 18F-FECH. *European Journal of Nuclear Medicine and Molecular Imaging* **39,** 1085–1086 (2012).

52. Bauman, G. *et al.* [18F]-DCFPyL Positron Emission Tomography/Magnetic Resonance Imaging for Localization of Dominant Intraprostatic Foci: First Experience. *European Urology Focus, in Press* (2016).

53. Sweat, S. D., Pacelli, A., Murphy, G. P. & Bostwick, D. G. Prostate-specific membrane antigen expression is greatest in prostate adenocarcinoma and lymph node metastases. *Urology* **52,** 637–640 (Oct. 1998).

54. Afshar-Oromieh, A. *et al.* Comparison of PET imaging with a (68)Ga-labelled PSMA ligand and (18)F-choline-based PET/CT for the diagnosis of recurrent prostate cancer. *European Journal of Nuclear Medicine and Molecular Imaging* **41,** 11–20 (2014).

55. Afshar-Oromieh, A. *et al.* Comparison of PET/CT and PET/MRI hybrid systems using a 68Ga-labelled PSMA ligand for the diagnosis of recurrent prostate cancer: initial experience. *European Journal of Nuclear Medicine and Molecular Imaging* **41,** 887–897 (2014).

56. Fütterer, J. J. *et al.* Prostate cancer: Comparison of local staging accuracy of pelvic phased-array coil alone versus integrated endorectal-pelvic phased-array coils. *European Radiology* **17,** 1055–1065 (2007).

57. Ménard, C. *et al.* MRI-guided HDR prostate brachytherapy in standard 1.5T scanner. *International Journal of Radiation Oncology Biology Physics* **59,** 1414–1423 (2004).

58. Ménard, C. *et al.* MR-guided prostate biopsy for planning of focal salvage after radiation therapy. *Radiology* **274,** 181–191 (2015).

59. Gomez-Iturriaga, A. *et al.* Dose escalation to dominant intraprostatic lesions with MRI-transrectal ultrasound fusion high-dose-rate prostate brachytherapy. Prospective phase II trial. *Radiotherapy and Oncology* **119,** 91–96 (2016).

60. Stanisz, G. J. *et al.* T1, T2 relaxation and magnetization transfer in tissue at 3T. *Magnetic Resonance in Medicine* **54,** 507–512 (2005).

61. Barentsz, J. O. *et al.* ESUR prostate MR guidelines 2012. *European Radiology* **22,** 746–757 (2012).

62. Westphalen, A. C. *et al.* High-resolution 3-T endorectal prostate MRI: A multireader study of radiologist preference and perceived interpretive quality of 2D and 3D T2-weighted fast spin-echo MR images. *American Journal of Roentgenology* **206,** 86–91 (2016).

63. Koh, D. M. & Collins, D. J. Diffusion-weighted MRI in the body: Applications and challenges in oncology. *American Journal of Roentgenology* **188,** 1622–1635 (2007).

64. Donato, F. *et al.* Geometric distortion in diffusion-weighted MR imaging of the prostate-Contributing factors and strategies for improvement. *Academic Radiology* **21,** 817–823 (2014).

65. Pallares, J. *et al.* Study of microvessel density and the expression of the angiogenic factors VEGF, bFGF and the receptors Flt-1 and FLK-1 in benign, premalignant and malignant prostate tissues. *Histology and Histopathology* **21,** 857–865 (2006).

66. Van Niekerk, C. G. *et al.* Correlation between dynamic contrast-enhanced MRI and quantitative histopathologic microvascular parameters in organ-confined prostate cancer. *European Radiology* **24,** 2597–2605 (2014).

67. Donahue, K. M. & Donahue, K. M. Studies of Gd-DTPA relaxivity and proton exchange rates in tissue with implications for MR imaging of regional myocardial perfusion. *Magnetic Resonance in Medicine* **32,** 66–76 (1993).

68. Tofts, P. S. *et al.* Estimating kinetic parameters from dynamic contrast-enhanced T1-weighted MRI of a diffusable tracer: Standardized quantities and symbols. *Journal of Magnetic Resonance Imaging* **10,** 223–232 (1999).

69. Kozlowski, P. *et al.* Combined diffusion-weighted and dynamic contrast-enhanced MRI for prostate cancer diagnosis - Correlation with biopsy and histopathology. *Journal of Magnetic Resonance Imaging* **24,** 108–113 (2006).

70. Parker, G. J. M. *et al.* Experimentally-derived functional form for a population-averaged high-temporal-resolution arterial input function for dynamic contrast-enhanced MRI. *Magnetic Resonance in Medicine* **56,** 993–1000 (2006).

71. Kovar, D. a., Lewis, M. & Karczmar, G. S. A new method for imaging perfusion and contrast extraction fraction: Input functions derived from reference tissues. *Journal of Magnetic Resonance Imaging* **8,** 1126–1134 (1998).

72. Ream, J. M. *et al.* Dynamic contrast-enhanced MRI of the prostate: An intra-individual assessment of the effect of temporal resolution on qualitative detection and quantitative analysis of histopathologically proven prostate cancer. *Journal of Magnetic Resonance Imaging, in Press* (2016).

73. Eyal, E. *et al.* Principal component analysis of dynamic contrast enhanced MRI in human prostate cancer. *Investigative Radiology* **45,** 174–181 (2010).

74. Rosenkrantz, A. B. *et al.* Dynamic contrast-enhanced MRI of the prostate with high spatiotemporal resolution using compressed sensing, parallel imaging, and continuous golden-angle radial sampling: Preliminary experience. *Journal of Magnetic Resonance Imaging* **41,** 1365–1373 (2014).

75. Langer, D. L. *et al.* Prostate cancer detection with multi-parametric MRI: Logistic regression analysis of quantitative T2, diffusion-weighted imaging, and dynamic contrast-enhanced MRI. *Journal of Magnetic Resonance Imaging* **30,** 327–334 (2009).

76. Selnæs, K. M. *et al.* Peripheral zone prostate cancer localization by multiparametric magnetic resonance at 3 T. *Investigative Radiology* **47,** 624–633 (2012).

77. Steenbergen, P. *et al.* Prostate tumor delineation using multiparametric magnetic resonance imaging: Inter-observer variability and pathology validation. *Radiotherapy and Oncology* **115,** 186–190 (2015).

78. Gibson, E. *et al.* Toward prostate cancer contouring guidelines on magnetic resonance imaging: Dominant lesion gross and clinical target volume coverage via accurate histology fusion. *International Journal of Radiation Oncology Biology Physics* **96,** 188–196 (2016).

79. Epstein, J. I., Walsh, P. C., Carmichael, M. & Brendler, C. B. Pathologic and clinical findings to predict tumor extent of nonpalpable (stage T1c) prostate cancer. *Journal of the American Medical Association* **271,** 368–374 (1994).

80. Abdollah, F. *et al.* A competing-risks analysis of survival after alternative treatment modalities for prostate cancer patients: 1988-2006. *European Urology* **59,** 88–95 (2011).

81. Adam, M. *et al.* Functional outcomes and quality of life after radical prostatectomy only versus a combination of prostatectomy with radiation and hormonal therapy. *European Urology* **71,** 330–336 (2016).

82. Abdollah, F. *et al.* Comparison of mortality outcomes after radical prostatectomy versus radiotherapy in patients with localized prostate cancer: a population-based analysis. *International Journal of Urology* **19,** 836–844 (2012).

83. Moghanaki, D., Freedland, S. J. & Anscher, M. Re: Comparison of mortality outcomes after radical prostatectomy versus radiotherapy in patients with localized prostate cancer: A population-based analysis. *International Journal of Urology* **20,** 547–548 (2013).

84. Yaxley, J. W. *et al.* Robot-assisted laparoscopic prostatectomy versus open radical retropubic prostatectomy: early outcomes from a randomised controlled phase 3 study. *The Lancet* **388,** 1057–1066 (2016).

85. Mazeron, J. J., Scalliet, P., Van Limbergen, E. & Lartigau, E. Radiobiology of brachytherapy and the dose-rate effect. *The GEC-ESTRO handbook of brachytherapy,* 95–121 (2002).

86. Wolff, D. *et al.* Volumetric modulated arc therapy (VMAT) vs. serial tomotherapy, step-and-shoot IMRT and 3D-conformal RT for treatment of prostate cancer. *Radiotherapy and Oncology* **93,** 226–233 (2009).

87. Yoo, S., Wu, Q. J., Lee, W. R. & Yin, F. F. Radiotherapy treatment plans with RapidArc for prostate cancer involving seminal vesicles and lymph nodes. *International Journal of Radiation Oncology Biology Physics* **76,** 935–942 (2010).

88. Unterweger, M. P., Hoppes, D. D., Schima, F. J. & Coursey, J. S. *Radionuclide Half-Life Measurements Data* 2016. `https://www.nist.gov/pml/radionuclide-half-life-measurements-data` (2017).

89. Nag, S., Beyer, D., Friedland, J., Grimm, P. & Nath, R. American brachytherapy society (ABS) recommendations for transperineal permanent brachytherapy of prostate cancer. *International Journal of Radiation Oncology Biology Physics* **44,** 789–799 (1999).

90. Kovács, G. & Hoskin, P. *Interstitial prostate brachytherapy* 1–260 (Springer Berlin Heidelberg, 2013).

91. Potters, L. *et al.* 12-year outcomes following permanent prostate brachytherapy in patients with clinically localized prostate cancer. *The Journal of Urology* **173,** 1562–1566 (2005).

92. Morris, W. *et al.* Androgen Suppression Combined with Elective Nodal and Dose Escalated Radiation Therapy (the ASCENDE-RT Trial): An Analysis of Survival Endpoints for a Randomized Trial Comparing a Low-Dose-Rate Brachytherapy Boost to a Dose-Escalated External Beam Boost. *International Journal of Radiation Oncology Biology Physics* **in Press** (2017).

93. Yamada, Y. *et al.* American Brachytherapy Society consensus guidelines for high-dose-rate prostate brachytherapy. *Brachytherapy* **11,** 20–32 (2012).

94. Helou, J. *et al.* High dose-rate brachytherapy boost for intermediate risk prostate cancer: Long-term outcomes of two different treatment schedules and early biochemical predictors of success. *Radiotherapy and Oncology* **115,** 84–89 (2015).

95. Yoshioka, Y. *et al.* High-dose-rate brachytherapy as monotherapy for intermediate- and high-risk prostate cancer: Clinical results for a median 8-year follow-up. *International Journal of Radiation Oncology Biology Physics* **94,** 675–682 (2016).

96. Scher, H. I. & Heller, G. Clinical states in prostate cancer: toward a dynamic model of disease progression. *Urology* **55,** 323–327 (2000).

97. Zelefsky, M. J. *et al.* Long-term results of conformal radiotherapy for prostate cancer: impact of dose escalation on biochemical tumor control and distant metastases-free survival outcomes. *International Journal of Radiation Oncology Biology Physics* **71,** 1028–1033 (July 2008).

98. Hoskin, P. J. *et al.* Randomised trial of external beam radiotherapy alone or combined with high-dose-rate brachytherapy boost for localised prostate cancer. *Radiotherapy and Oncology* **103,** 217–222 (2012).

99. Cox, J. D., Stetz, J. & Pajak, T. F. Toxicity criteria of the Radiation Therapy Oncology Group (RTOG) and the European Organization for Research and Treatment of Cancer (EORTC). *International Journal of Radiation Oncology Biology Physics* **31,** 1341–1346 (1995).

100. Galalae, R. M. *et al.* Hypofractionated conformal HDR brachytherapy in hormone naive men with localized prostate cancer: Is Escalation to very high biologically equivalent dose beneficial in all prognostic risk groups? *Strahlentherapie und Onkologie* **182,** 135–141 (2006).

101. Pucar, D. *et al.* Clinically significant prostate cancer local recurrence after radiation therapy occurs at the site of primary tumor: Magnetic resonance imaging and step-section pathology evidence. *International Journal of Radiation Oncology Biology Physics* **69,** 62–69 (2007).

102. Arrayeh, E. *et al.* Does local recurrence of prostate cancer after radiation therapy occur at the site of primary tumor? Results of a longitudinal MRI and MRSI study. *International Journal of Radiation Oncology Biology Physics* **82,** 787–793 (Apr. 2012).

103. Bauman, G., Haider, M., Van Der Heide, U. A. & Ménard, C. Boosting imaging defined dominant prostatic tumors: A systematic review. *Radiotherapy and Oncology* **107,** 274–281 (2013).

104. Von Eyben, F. E. *et al.* Radiotherapy boost for the dominant intraprostatic cancer lesion - A systematic review and meta-analysis. *Clinical Genitourinary Cancer* **14,** 189–197 (2016).

105. Singh, A. K. *et al.* Simultaneous integrated boost of biopsy proven, MRI defined dominant intra-prostatic lesions to 95 Gray with IMRT: early results of a phase I NCI study. *Radiation Oncology* **2** (2007).

106. Crook, J. *et al.* Ultrasound-planned high-dose-rate prostate brachytherapy: Dose painting to the dominant intraprostatic lesion. *Brachytherapy* **13,** 433–441 (2014).

107. Vigneault, E. *et al.* Image-guided high-dose-rate brachytherapy boost to the dominant intraprostatic lesion using multiparametric magnetic resonance imaging including spectroscopy: Results of a prospective study. *Brachytherapy* **15,** 746–751 (2016).

108. Ares, C. *et al.* Hypofractionated boost with high-dose-rate brachytherapy and open magnetic resonance imaging-guided implants for locally aggressive prostate cancer: A sequential dose-escalation pilot study. *International Journal of Radiation Oncology Biology Physics* **75,** 656–663 (2009).

109. Schick, U. *et al.* High-dose-rate brachytherapy boost to the dominant intra-prostatic tumor region: hemi-irradiation of prostate cancer. *The Prostate* **71,** 1309–1316 (2011).

110. Kupelian, P. *et al.* Multi-institutional clinical experience with the Calypso System in localization and continuous, real-time monitoring of the prostate gland during external radiotherapy. *International Journal of Radiation Oncology Biology Physics* **67,** 1088–1098 (2007).

111. Van der Heide, U. A. *et al.* Analysis of fiducial marker-based position verification in the external beam radiotherapy of patients with prostate cancer. *Radiotherapy and Oncology* **82,** 38–45 (2007).

112. Lips, I. M. *et al.* Single blind randomized phase III trial to investigate the benefit of a focal lesion ablative microboost in prostate cancer (FLAME-trial): study protocol for a randomized controlled trial. *Trials* **12** (2011).

113. Yun, J. *et al.* First demonstration of intrafractional tumor-tracked irradiation using 2D phantom MR images on a prototype linac-MR. *Medical Physics* **40,** 051718 (2013).

114. Kirisits, C. *et al.* Review of clinical brachytherapy uncertainties: Analysis guidelines of GEC-ESTRO and the AAPM. *Radiotherapy and Oncology* **110,** 199–212 (2014).

115. Holly, R. *et al.* Use of cone-beam imaging to correct for catheter displacement in high dose-rate prostate brachytherapy. *Brachytherapy* **10,** 299–305 (2011).

116. Kim, Y., Hsu, I.-C. C., Lessard, E., Vujic, J. & Pouliot, J. Dosimetric impact of prostate volume change between CT-based HDR brachytherapy fractions. *International Journal of Radiation Oncology Biology Physics* **59,** 1208–1216 (2004).

117. Kawakami, S. *et al.* Catheter displacement prior to the delivery of high-dose-rate brachytherapy in the treatment of prostate cancer patients. *Journal of Contemporary Brachytherapy* **6,** 161–166 (2014).

118. Rylander, S., Buus, S., Pedersen, E., Bentzen, L. & Tanderup, K. Dosimetric impact of contouring and needle reconstruction uncertainties in US-, CT- and MRI-based high-dose-rate prostate brachytherapy treatment planning. *Radiotherapy and Oncology* **in Press** (2017).

119. Murgic, J. *et al.* Lessons learned using an MRI-only workflow during high-dose-rate brachytherapy for prostate cancer. *Brachytherapy* **15,** 147–155 (2016).

120. Jaffray, D. A. *et al.* A facility for magnetic resonance-guided radiation therapy. *Seminars in Radiation Oncology* **24,** 193–195 (2014).

121. Cepek, J. *et al.* Mechatronic system for in-bore MRI-guided insertion of needles to the prostate: An in vivo needle guidance accuracy study. *Journal of Magnetic Resonance Imaging* **42,** 48–55 (2015).

122. Even, A. J. G. *et al.* High-dose-rate prostate brachytherapy based on registered transrectal ultrasound and in-room cone-beam CT images. *Brachytherapy* **13,** 128–136 (2014).

123. Batchelar, D. L. *et al.* Intraoperative ultrasound-based planning can effectively replace postoperative CT-based planning for high-dose-rate brachytherapy for prostate cancer. *Brachytherapy* **15,** 399–405 (2016).

124. Sun, Y., Qiu, W., Romagnoli, C. & Fenster, A. 3D non-rigid surface-based MR-TRUS registration for image-guided prostate biopsy. *Progress in Biomedical Optics and Imaging - Proceedings of SPIE,* 90362 (2014).

125. Zheng, D. & Todor, D. A. A novel method for accurate needle-tip identification in trans-rectal ultrasound-based high-dose-rate prostate brachytherapy. *Brachytherapy* **10,** 466–473 (2011).

126. Morton, G. *et al.* Prostate high dose-rate brachytherapy as monotherapy for low and intermediate risk prostate cancer: Early toxicity and quality-of life results from a randomized phase II clinical trial of one fraction of 19 Gy or two fractions of 13.5 Gy. *Radiotherapy and Oncology* **122,** 323–330 (2016).

127. Tiong, A. *et al.* A small tolerance for catheter displacement in high-dose rate prostate brachytherapy is necessary and feasible. *International Journal of Radiation Oncology Biology Physics* **76,** 1066–1072 (2010).

128. Mason, J., Al-Qaisieh, B., Bownes, P., Thwaites, D. & Henry, A. Dosimetry modeling for focal high-dose-rate prostate brachytherapy. *Brachytherapy* **13,** 611–617 (2014).

129. Hoskin, P. J. *et al.* Dosimetric predictors of biochemical control of prostate cancer in patients randomised to external beam radiotherapy with a boost of high dose rate brachytherapy. *Radiotherapy and Oncology* **110,** 110–113 (2014).

130. Reich, D. L. *et al.* Predictors of hypotension after induction of general anesthesia. *Anesthesia and Analgesia* **101,** 622–628 (2005).

131. Aboofazeli, M., Abolmaesumi, P., Mousavi, P. & Fichtinger, G. A new scheme for curved needle segmentation in threedimensional ultrasound images. *Proceedings - 2009 IEEE International Symposium on Biomedical Imaging,* 1067–1070 (2009).

132. Barva, M., Uherčík, M. & Mari, J. Parallel integral projection transform for straight electrode localization in 3-D ultrasound images. *IEEE Transactions on Ultrasonics, Ferroelectrics, and Frequency Control* **55,** 1559–1569 (2008).

133. Beigi, P., Rohling, R., Salcudean, T., Lessoway, V. A. & Ng, G. C. Needle trajectory and tip localization in real-time 3D ultrasound using a moving stylus. *Ultrasound in Medicine and Biology* **41,** 2057–2070 (2015).

134. Ding, M. & Fenster, A. A real-time biopsy needle segmentation technique using Hough transform. *Medical Physics* **30,** 2222–2233 (2003).

135. Luengo Hendriks, C. L., Van Ginkel, M., Verbeek, P. W. & Van Vliet, L. J. The generalized Radon transform: Sampling, accuracy and memory considerations. *Pattern Recognition* **38,** 2494–2505 (2005).

136. Neshat, H. R. S. & Patel, R. V. Real-time parametric curved needle segmentation in 3D ultrasound images. *Proceedings of the 2nd International Conference on Biomedical Robotics and Biomechatronics,* 670–675 (2008).

137. Novotny, P. M. *et al.* GPU based real-time instrument tracking with three-dimensional ultrasound. *Medical Image Analysis* **11,** 458–464 (2007).

138. Qiu, W., Yuchi, M., Ding, M., Tessier, D. & Fenster, A. Needle segmentation using 3D Hough transform in 3D TRUS guided prostate transperineal therapy. *Medical Physics* **40,** 042902 (2013).

139. Qiu, W., Ding, M. & Yuchi, M. Electrode localization in 3D ultrasound images using 3D phase grouping and randomized Hough transform. *Proceedings - 4th International Conference on Genetic and Evolutionary Computing,* 202–205 (2010).

140. Qiu, W., Yuchi, M. & Ding, M. Phase grouping-based needle segmentation in 3-D trans-rectal ultrasound-guided prostate trans-perineal therapy. *Ultrasound in Medicine and Biology* **40,** 804–816 (2014).

141. Uherčík, M., Kybic, J., Liebgott, H. & Cachard, C. Model fitting using ransac for surgical tool localization in 3D ultrasound images. *IEEE Transactions on Biomedical Engineering* **57,** 1907–1916 (2010).

142. Uherčík, M., Kybic, J., Zhao, Y., Cachard, C. & Liebgott, H. Line filtering for surgical tool localization in 3D ultrasound images. *Computers in Biology and Medicine* **43,** 2036–2045 (2013).

143. Zhao, S., Qiu, W., Ming, Y. & Ding, M. Needle segmentation in 3D ultrasound images based on phase grouping. *Progress in Biomedical Optics and Imaging - Proceedings of SPIE,* 7497 (2009).

144. Zhou, H., Qiu, W., Ding, M. & Zhang, S. Automatic needle segmentation in 3D ultrasound images using 3D improved Hough transform. *Progress in Biomedical Optics and Imaging - Proceedings of SPIE,* 6918 (2008).

145. Wan, G., Wei, Z., Gardi, L., Downey, D. B. & Fenster, A. Brachytherapy needle deflection evaluation and correction. *Medical Physics* **32,** 902–909 (2005).

146. Yang, X. *et al.* A MRI-CT prostate registration using sparse representation technique. *Progress in Biomedical Optics and Imaging - Proceedings of SPIE,* 9786 (2016).

147. Furman-Haran, E., Grobgeld, D., Kelcz, F. & Degani, H. Critical role of spatial resolution in dynamic contrast-enhanced breast MRI. *Journal of Magnetic Resonance Imaging* **13,** 862–867 (2001).

148. Cepek, J., Chronik, B. A. & Fenster, A. The effects of magnetic field distortion on the accuracy of passive device localization frames in MR imaging. *Medical Physics* **41,** 052301 (2014).

149. Ryu, B. *et al.* Prostate brachytherapy with oblique needles to treat large glands and overcome pubic arch interference. *International Journal of Radiation Oncology Biology Physics* **83,** 1463–1472 (2012).

150. Bharat, S. *et al.* Electromagnetic tracking for catheter reconstruction in ultrasound-guided high-dose-rate brachytherapy of the prostate. *Brachytherapy* **13,** 640–650 (2014).

151. Poulin, E., Racine, E., Binnekamp, D. & Beaulieu, L. Fast, automatic, and accurate catheter reconstruction in HDR brachytherapy using an electromagnetic 3D tracking system. *Medical Physics* **42,** 1227–1232 (2015).

152. Qiu, W., Ding, M. & Yuchi, M. Needle segmentation using 3D quick randomized hough transform. *Proceedings - The 1st International Conference on Intelligent Networks and Intelligent Systems,* 449–452 (2008).

153. Aerts, H., Jaspers, K. & Backes, W. The precision of pharmacokinetic parameters in dynamic contrast-enhanced magnetic resonance imaging: The effect of sampling frequency and duration. *Physics in Medicine and Biology* **56** (2011).

154. Chen, Y. J. *et al.* Washout gradient in dynamic contrast-enhanced MRI is associated with tumor aggressiveness of prostate cancer. *Journal of Magnetic Resonance Imaging* **36,** 912–919 (2012).

155. Degani, H., Gusis, V., Weinstein, D., Fields, S. & Strano, S. Mapping pathophysiological features of breast tumors by MRI at high spatial resolution. *Nature Medicine* **3,** 780–782 (1997).

Chapter 2

Three-dimensional transrectal ultrasound guided high-dose-rate prostate brachytherapy: a comparison of needle segmentation accuracy with two-dimensional image-guidance

HDR-BT treatment plans are critically sensitive to uncertainty in needle tip positions, and SR3D TRUS may decrease this uncertainty. The purpose of Chapter 2 is to measure HDR-BT needle insertion depth errors provided by SR3D TRUS, to compare these errors with those provided by conventional imaging which uses AR3D TRUS, and to determine the impact of insertion depth errors of each imaging technique on whole-gland treatment dosimetry.

The contents of this chapter have previously been published in *Brachytherapy*: WT Hrinivich, DA Hoover, K Surry, C Edirisinghe, J Montreuil, D D'Souza, A Fenster, E Wong. Brachytherapy 2016; 15(2):231-239. Permission to reproduce this article was granted by Elsevier and is provided in Appendix E.

2.1 Introduction

High-dose-rate brachytherapy (HDR-BT) has been shown to be an effective method of

dose escalation when used in combination with external beam radiation therapy (EBRT)

for the treatment of intermediate to high-risk prostate cancer [1–4]. Clinical trials have

shown an improvement in biochemical disease free survival (bDFS) using HDR-BT

dose-escalated EBRT *versus* EBRT alone [5, 6]. Furthermore, with the recent report of positive results from the ASCENDE-RT randomized trial [7], there will likely be an increase in the number of intermediate and high-risk prostate cancer patients who will undergo brachytherapy.

While it is well-known that HDR-BT techniques offer improved conformity and normal tissue sparing [8, 9], this presupposes that the needles used to guide the high-activity gamma source have been segmented accurately on imaging, with one study finding that the source must be localized to within 3 mm for acceptable dosimetric uncertainty [10]. Because of the high spatial resolution and high needle-to-tissue contrast in CT imaging, image-guided HDR-BT was originally performed using CT scans acquired following TRUS-guided needle insertion [11]. Unfortunately, patient repositioning and swelling that occurs during patient setup for CT imaging has been found to cause shifts in needle positions as evidenced by studies reporting mean (range) shifts of 11.5 (0-42) mm [12], 10 (5-23) mm [13], and 5.4 (-4-18) mm [14] between treatment fractions. For patients undergoing single fraction CT-guided HDR-BT, mean shifts of 11 mm have been found between the planning CT and time of treatment delivery, with 10% of needles shifting inferiorly by more than 20 mm [15].

In an effort to eliminate the need to reposition patients during treatment, intra-operative TRUS imaging has been proposed for needle and organ segmentation. Using a tracked probe stepper and compatible segmentation software, TRUS images may be used for needle insertion guidance and segmentation while the patient remains in the operating room. The prostate and nearby organs may be localized by stepping the probe in the superior/inferior direction to create a stack of axial images for segmentation; however, limited image sampling in the needle insertion direction (typically 1-5 mm) introduces uncertainty in needle tip positions [16–18]. Siebert et al. investigated the ability to identify needle tips in water phantoms and found that sub-millimeter accuracy was achievable when using the sagittal crystal of a bi-plane TRUS probe [16].

With these imaging characteristics in mind, HDR-BT workflows have been proposed that involve segmenting the prostate and nearby organs using an image volume reconstructed from axial images, segmenting needle tips using live 2D sagittal images, and combining the views by manually aligning the axial organ segmentations on a mid-gland sagittal image, using anatomical landmarks such as the bladder as indicated in Figure 2.1. Schmid et al. investigated the accuracy of this 2D sagittally-assisted axially-reconstructed (SAAR) approach in phantoms by comparing TRUS and CT-based segmentations, and demonstrated that tip localization accuracy within 1.9 mm is achievable in phantoms with up to 18 needles [17]. Batchelar et al. investigated the accuracy of the TRUS-based approach *in vivo* by comparing SAAR-guided needle segmentations with in-room cone-beam CT-based needle segmentations from 37 HDR-BT procedures [18]. Relative needle segmentation error was measured by selecting a posterior needle tip on both the SAAR-guided segmentation and the cone-beam CT-based segmentation and aligning the remaining needle segmentations using this corresponding point. Results indicated relative tip localization error was less than 3 mm in 97% of all needles when using the SAAR technique. While the relative needle tip localization accuracy for TRUS-guided HDR-BT is promising, potential systematic shifts in tip positions introduced during the axial-to-sagittal image registration step have not been fully investigated and may contribute to absolute needle tip localization uncertainty. Alternative needle tip localization workflows have also been proposed by vendors such as Elekta (Stolkholm, SE), making use of measurements of needle ends protruding from the insertion template combined with encoder calibrations and the physical needle length to calculate the needle insertion depth within the axially-reconstructed 3D image. This technique mitigates registration uncertainty between axial and sagittal views using the probe tracking information provided by the encoders, but stepping the probe in the inferior direction for axial image acquisition may still introduce shifts in anatomy relative to the needle tip positions calculated using the end-length measurements.

Our lab has previously developed TRUS imaging techniques that allow the reconstruction of a 3D image using the sagittal crystal of a bi-plane probe by rotating the probe using a motor while simultaneously capturing images [19]. This method of acquiring sagittally-reconstructed 3D (SR3D) images maintains high spatial resolution in the needle insertion direction while providing a complete 3D image for prostate and organ segmentation, thereby eliminating the need to move the probe in the superior/inferior direction for sagittal and axial imaging and eliminating the axial-to-sagittal segmentation alignment step [20]. Variants of this SR3D image reconstruction technique also have been made commercially available, including the Twister[TM] image acquisition feature available in Variseed[TM] 8.0 (Varian Medical Systems Inc., Palo Alto CA, USA) and Oncentra[TM] Brachy (Elekta, Stolkholm, SE). Our lab has also developed a compact mechatronic device designed for SR3D image-guided transperineal needle insertions that enables superior/inferior probe position tracking relative to an external frame of reference [21]. Through calibration, the position of each image relative to the insertion template is determined. Tracking this position enables the use of needle end-length measurements [22] to estimate absolute insertion depth errors in each image as indicated in Figure 2.2. The purpose of this study is to compare needle tip localization accuracy between SAAR and SR3D-guided approaches using calibrated end length measurements as the gold standard, and to estimate the dosimetric impact of measured needle insertion depth errors on clinical treatment plans.

2.2 Materials and Methods

2.2.1 Image Acquisition and Segmentation

Twelve intermediate-risk prostate cancer patients underwent HDR-BT using the conventional SAAR-guided technique. The brachytherapy prescription dose of 15 Gy was delivered in a single fraction and after a two-week break, all patients went on to re-
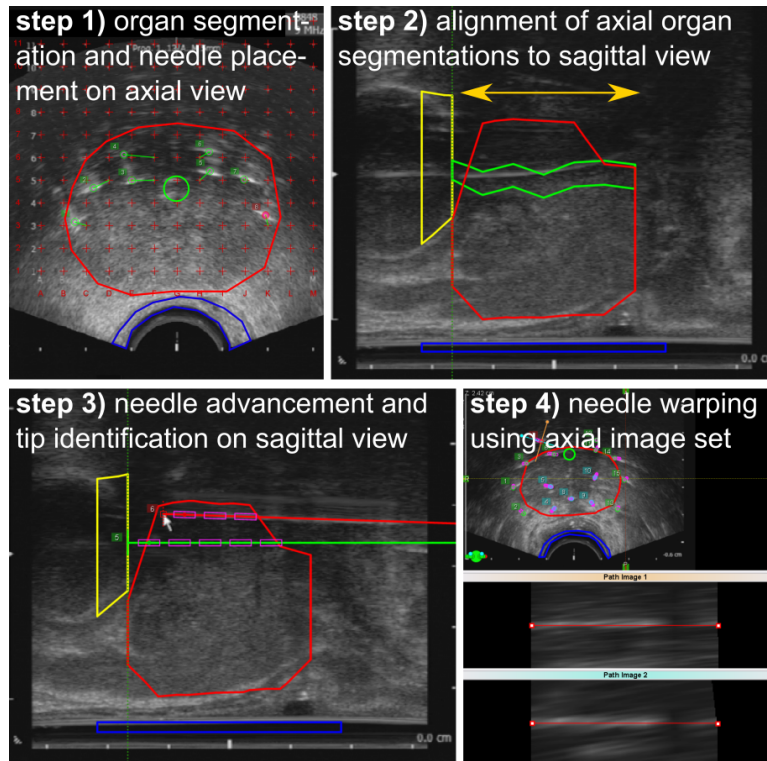
Figure 2.1: Screenshots taken from Vitesse treatment planning software during SAAR-guided HDR-BT needle insertion. The prostate, urethra, rectum, and bladder, are indicated in red, green, blue, and yellow, respectively. Major steps of the imaging and segmentation procedure are highlighted. Among the differences between the SAAR and SR3D-guided segmentation techniques described in this study, the SR3D-guided technique would eliminate the need for the axial-to-sagittal segmentation alignment indicated in step 2).

ceive 37.5 Gy of EBRT delivered in 15 daily fractions (5 week total treatment duration) [23]. A BK Medical ProFocus 2202 ultrasound system and 8848 bi-plane transducer (BK Medical, Boston MA, USA) were used for imaging at 9 MHz and 6.3 cm field of view. Vitesse software (Varian Medical Systems Inc., Palo Alto CA, USA) was used for intra-operative SAAR-guided organ and needle segmentation. The probe and HDR-BT template were supported using the compact mechatronic device, which was affixed to the operating table using an RTP 6000 Precision stabilizer (Brachytherapy Services Inc. Fullerton VA, USA). Before and after needle insertion, sets of contiguous 2D axial images were acquired in 5 mm steps beginning at the bladder and moving towards the

prostate apex for SAAR-guided organ segmentations, immediately followed by SR3D images spanning 140° reconstructed from sagittal images acquired at 0.5° angular intervals. Major steps of the intra-operative SAAR workflow are indicated in Figure 2.1, and details are included in Appendix A.1. All SR3D needle segmentations were performed post-operatively in this study for comparison with the standard clinical SAAR method, and were not used for intra-operative treatment planning or delivery. The University of Western Ontario Health Sciences Research Ethics Board approved the use of the device with patients for comparison with conventional image-guided brachytherapy needle insertions.

2.2.2   3D TRUS Guided Mechatronic Device

The compact mechatronic device for SR3D-guided transperineal needle insertions previously developed in our lab [21] was modified to include a manual probe stepper required in the conventional SAAR-guided HDR-BT procedure. An HDR-BT template mounting point and haptic feedback at 5 mm increments were incorporated in the design, similar to the manual stepper regularly used in our clinic (Classic stepper, CIVCO Medical, Coralville IA, USA). These modifications permitted the acquisition of co-registered axial and SR3D images with minimal disruption to the conventional HDR-BT workflow. An encoder was employed to track the superior/inferior probe position, and a string phantom calibration was performed allowing the use of these encoder values to calculate the position of all axial and SR3D images relative to the HDR-BT template face. This calibration procedure is discussed in the Appendix A.2, along with estimates of mechanical uncertainty.

2.2.3   Post-Operative Image Segmentation and Registration

Following the HDR-BT procedure, the SR3D images were imported into BrachyVision (Varian Medical Systems Inc., Palo Alto CA, USA) for retrospective analysis. To en-

able comparison of needle segmentations produced using the two imaging techniques, post-needle insertion SR3D images were rigidly registered to the post-needle insertion SAAR axial image sets for each patient as follows. Longitudinal encoder positions recorded for each image along with the sagittal-to-axial crystal distance were used to align the SAAR axial image set and SR3D images in the superior/inferior direction. Measurements of these calibrated encoder values are discussed in the Appendix. Encoder values corresponding to the axial image set for one patient were not recorded, so anatomical landmarks were used to register the axial image set with the SR3D image. The imaged probe cover was used to align the images in the anterior/posterior and left/right directions. Ultrasound machine image-lag has previously been found to cause small angular shifts in SR3D images about the probes axis of rotation [21]. These angular rotations were found to be on the order of $2.5°$ in this study and were manually corrected based on anatomical landmarks.

All needles were manually segmented in BrachyVision as they appeared on the post-insertion SR3D images by a medical physicist (DH). A single mid-gland axial image from the intra-operative treatment plan was cross-referenced during this retrospective needle segmentation for the sole purpose of assigning identical needle labels between SAAR and SR3D image sets. All data were anonymized and exported from Eclipse as DICOM files for geometric analysis using MATLAB 2015a (Mathworks, Natick MA, USA). All statistical tests were performed using SPSS 21 (IBM, Armonk NY, USA).

2.2.4 Experimental Methods: Comparing SAAR and SR3D-Guided Segmentations

Needle Tip Position Comparison Between SAAR and SR3D-Guided Segmentations

Needle tip positions were compared between imaging techniques by bringing both sets of segmentations to a common coordinate system using the transformation matrix produced by the rigid registration. Box plots of tip position differences were produced for each patient individually to determine whether tip differences were distributed evenly amongst all patients, or whether patient-specific differences existed.

Insertion Depth Comparison Between Segmentations and Physical Measurements

Needle insertion depths determined using the two imaging techniques were compared to physical end length measurements in order to estimate the insertion depth error as shown schematically in Figure 2.2. The length of each segmented needle within the SR3D image was determined from the needle tip to where the needle exited the SR3D image at the inferior edge (d_{image}). The distance between the inferior edge of the SR3D image and the inferior face of the insertion template on the mechatronic device ($d_{encoder}$) was calculated based on the encoder positions recorded intra-operatively. The encoder position values were calibrated to give $d_{encoder}$ using the string phantom as discussed in the Appendix. From the string phantom measurements, we estimated the uncertainty of $d_{encoder}$ to be ±0.5 mm. The needle free-end lengths (d_{end}) were physically measured intra-operatively using a graduated ruler during the procedure with estimated ±0.5 mm uncertainty. By comparing this needle length to the physical length of the needle (d_{phys}), an insertion depth error (IDE) could be estimated, as indicated in Eq. 2.1.

$$IDE = (d_{end} + d_{encoder} + d_{image}) - d_{physical} \qquad (2.1)$$

This process was performed for all needles using both the intra-operative SAAR-guided segmentations and post-operative SR3D-guided segmentations enabling comparison of insertion depth errors between imaging methods. Insertion depth accuracy was assessed by comparing patient-specific median insertion depth errors, and insertion depth precision was assessed by comparing patient specific inter-quartile ranges and full-ranges. Patient-specific metrics were compared using Wilcoxon signed-rank tests.
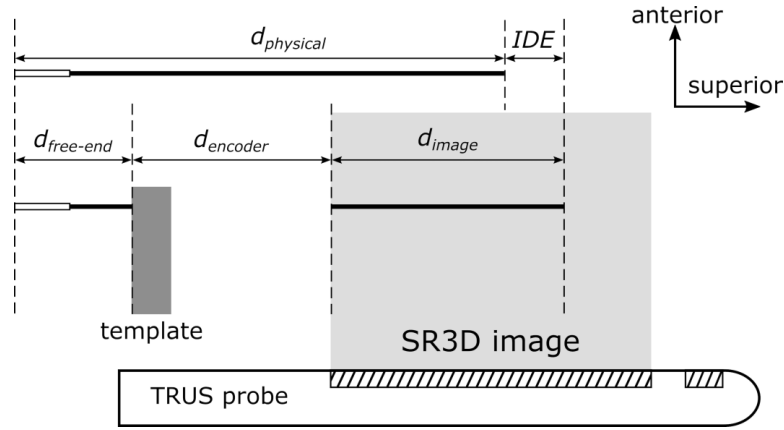
Figure 2.2: Schematic of measurements used to calculate needle insertion depth error (*IDE*). *IDE* was determined using the physical needle length ($d_{physical}$), needle free-end length measurements (d_{end}), distance from the template face to the inferior edge of the image volume determined by calibrated encoder positions ($d_{encoder}$), and the length of the image-defined needle (d_{image}). IDE was then calculated as $IDE = (d_{end} + d_{encoder} + d_{image}) - d_{physical}$.

Effect of Image Artifacts on Insertion Depth Errors

Needles present in TRUS images strongly reflect ultrasound signal, creating shadow artifacts that may obstruct the view of some of the more anterior needle tips. Since the SR3D needle segmentations were performed using an image acquired after all needles are inserted, we determine the prevalence of needles obstructed by shadow artifacts and their impact on tip localization accuracy. The medical physicist performing the SR3D segmentations qualitatively classified needle tips as unobstructed, partially obstructed,

or obstructed based on needle tip signal intensity relative to background signal intensity. Unobstructed needles were classified as having high apparent needle tip contrast, whereas obstructed needles were those where the needle appeared to enter a signal void, beyond which the trajectory and tip could no longer be identified. Partially obstructed needles were those that could not be clearly categorized as obstructed or unobstructed; typically having low needle tip contrast but without an obvious signal void at the needle tip. Example needle tip appearances are provided in the Appendix Figure A.3. A one-way ANOVA and Tukeys post hoc tests were used to compare insertion depth errors between needle tip appearance groups for the SR3D-guided segmentations.

Dosimetric Impact of Insertion Depth Errors

The dosimetric impact of insertion depth errors was determined as follows: starting with the clinical treatment plan, two new plans were generated per patient in Brachyvision based on the SAAR and SR3D insertion depth errors. The clinical intra-operatively planned dwell positions were shifted in the superior/inferior direction by each needle's insertion depth errors measured for SAAR-guidance and for SR3D-guidance. The volume of the prostate receiving 100% of the prostate prescription dose (V100%) and volume of the urethra receiving 120% of the prostate prescription dose (V120%) were compared between the clinical and simulated treatment plans for each patient. The mean changes in dosimetric parameters attributed to the SAAR and SR3D-guided insertion depth errors were compared using two-sided paired t-tests.

2.3 Results

2.3.1 Needle Tip Position Comparison Between SAAR and SR3D-Guided Segmentations

In total, 194 needles were inserted among all 12 patients. Eleven needles were excluded from analysis including three steel needles used during one HDR-BT procedure, two needles that were moved following SR3D image acquisition, five anterior needles that could not be detected in SR3D images from 4 patients, and one needle that appeared to extend beyond the edge of the SR3D image. The 5 needles that could not be visualized are addressed further in the Discussion. This resulted in 183 needles included in the segmentation analysis. Figure 2.3 displays 3D renderings of the co-registered needle segmentations of two patients intersecting an axial slice of the post-insertion SR3D image. Figure 2.4a-c displays boxplots of the tip distance components individually for each patient, and for all patients combined. In terms of Euclidean distance, the position of the needle tips identified using the two imaging methods differed by less than 3 mm in 33% of the cases, and by less than 5 mm in 64% of the cases. The largest difference components were noted to be in the superior/inferior direction.

2.3.2 Insertion Depth Comparison Between Segmentations and Physical Measurements

Figures 2.4d-e shows boxplots of the insertion depth errors determined by the SAAR and SR3D-guided approaches individually for each patient, and summarized over all patients. Mean standard deviation (SD) values of insertion depth errors over all 183 needles were found to be 2.8±3.2 mm and -0.6±3.2 mm for the SAAR and SR3D-guided approaches respectively. This difference was found to be statistically significant (p <.001). The box plots indicate statistically significantly larger systematic errors in
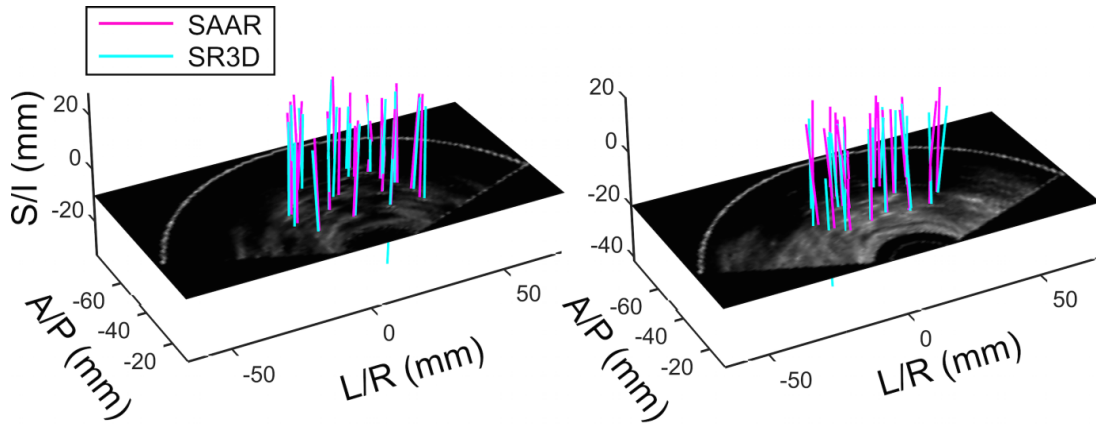
Figure 2.3: 3D renderings of the co-registered needle segmentations produced using SAAR and SR3D-guided needle segmentation approaches of two patients as an indication of needle density in the region of interest. Needle renderings are shown intersecting axial views of the SR3D images for each patient.

the SAAR *versus* SR3D-guided approach, with patient-specific median value ranges of [-1.1 mm, 6.4 mm] *versus* [-2.1 mm, 3.7 mm] respectively (p <.01). The box plots also indicate statistically significantly larger patient-specific inter-quartile ranges determined using the SAAR-guided approach with inter-patient ranges of [1.3 mm, 5.9 mm] *versus* [0.8 mm, 2.2 mm] determined with the SR3D-guided approach (p <.01). Examining the maximum insertion depth errors by looking at the full range of patient-specific needle insertion depth errors (indicated by the maximum and minimum dots for each patient), there was no statistical difference between the SR3D-guided and the SAAR-guided approach, with median values of 9.8 mm and 8.3 mm respectively (p >0.05),

	Unobstructed	Partially Obstructed	Obstructed	All
# (%) of Needles	143 (78)	22 (12)	18 (10)	183 (100)
Mean (SD) IDE (mm)	-0.47 (1.84)	-0.22 (5.98)	-2.23 (5.92)	-0.63 (3.22)

Table 2.1: Needle tip appearance and insertion depth errors (IDEs) determined using SR3D-guided segmentation
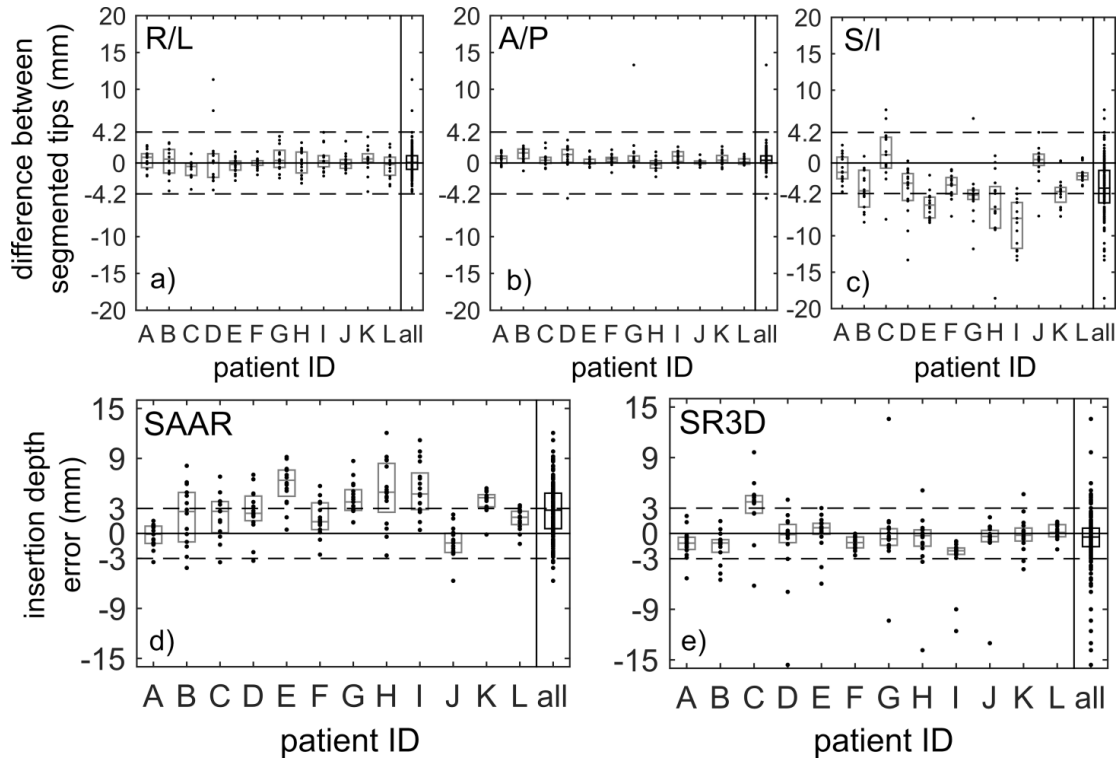
Figure 2.4: a-c) Plots of components of the differences between needle tips identified using the SAAR and SR3D-guided needle segmentation approaches. In a-c), horizontal lines indicate difference thresholds of ±4.2 mm, which are obtained by adding the ±3 mm error threshold for each segmentation method [10] in quadrature. This difference threshold was indicated for each difference component for visual comparison. d-e) Plots of insertion depth errors estimated from needle free-end length measurements for needles tips identified using SAAR and SR3D-guided needle segmentation approaches. The data is plotted separately for each patient as well as for all 12 patients combined. In a-e), boxes indicate inter-quartile range and centre lines indicate median value.

2.3.3 Effect of Image Artifacts on Insertion Depth Errors

Figure 2.5 shows a box plot of insertion depth errors from all 183 needles segmented using the SR3D-guided approaches, and grouped based on the tip appearance on the SR3D-image. Table 2.1 summarizes mean insertion depth errors for each group displayed in Figure 2.5. 78% percent of needles were considered unobstructed, 12% were considered partially obstructed, and 10% were considered obstructed. Over all 183 needles analyzed, the SR3D-guided approaches provided insertion depth errors of ±3 mm for 83% of needles and ±5 mm for 92% of needles. Within the unobstructed group, the SR3D-guided approach provided insertion depth errors within ±3 mm for 91% of needles and ±5 mm for 98% of needles; however, needle tip appearance on the SR3D image was not found to have a statistically significant effect on mean insertion depth error based on a one-way ANOVA (p >.05).
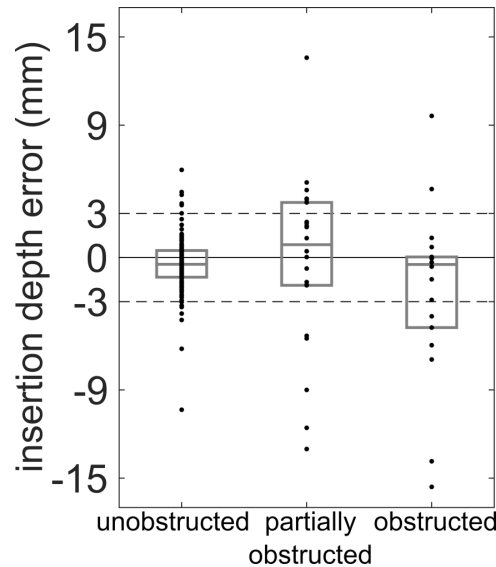
Figure 2.5: Plot of insertion depth errors estimated from needle free-end length measurements for needles from all 12 patients using SR3D-guided needle segmentation. Needles were qualitatively classified as unobstructed, partially obstructed, or obstructed based on needle tip intensity relative to background intensity on the SR3D images to determine the prevalence and impact of the ultrasound shadow artifacts on insertion depth error. 78% of needle tips appeared unobstructed, 12% appeared partially obstructed, and 10% appeared obstructed. Boxes indicate inter-quartile range and centre lines indicate median value.

2.3.4 Dosimetric Impact of Insertion Depth Errors

Dosimetric parameters corresponding to the intra-operatively produced treatment plans are listed in Table 2.2, along with the changes in parameters associated with the insertion depth errors from the SAAR and SR3D-guided needle segmentation approaches, indicated by ΔSAAR and ΔSR3D respectively. In terms of target coverage, the SAAR-guided insertion depth errors tended to produce greater decreases in prostate V100% than the SR3D-guided insertion depth errors with mean±SD of -6.5±6.7% and -1.2±1.3% respectively. This difference was found to be statistically significant (p <.01). In the SR3D-guided case, prostate V100% decreases of less than 3% were found in 11 out of 12 patients, and decreases of less than 5% were found in all patients. Loss of target coverage in the SAAR-guided case tended to occur at the prostate base attributed to systematic superior shifts in SAAR-imaging identified needle tips. Changes in urethral dose due to both the SAAR and SR3D-guided insertion depth errors depended on patient anatomy. Mean±SD changes in urethra V120% were found to be -2.1±6.6% and -0.2±3.8% for the SAAR and SR3D-guided insertion depth errors respectively, but this difference was not found to be statistically significant.

2.4 Discussion

The focus of this study was to compare needle tip localization accuracy of SAAR and SR3D-guided HDR-BT. Our results indicate that the SR3D-guided approach provides more accurate and precise insertion depths than the SAAR-guided approach for the majority of needles, leading to improvements in prostate V100%. Both techniques rely on the sagittal transducer for tip identification. The observed decrease in systematic errors in the SR3D-guided segmentations is attributed to eliminating the need to move the probe in the superior/inferior direction for axial image acquisition following needle tip identification with the sagittal ultrasound crystal, thereby mitigating organ motion and

	Prostate V100%			Urethra V120%		
Patient	Intra-op %	ΔSAAR	ΔSR3D	Intra-op %	ΔSAAR	ΔSR3D
A	97.1	0.6	0.6	1.8	-0.6	0.3
B	97.0	-2.8	-1.1	2.3	-1.3	1.9
C	91.5	-1.5	-4.0	19.1	-6.9	7.0
D	95.9	-9.6	-2.7	8.3	-7.2	-7.2
E	92.2	-13.5	-0.8	29.5	-19.3	-6.7
F	96.1	-3.0	0.5	9.2	7.0	-2.1
G	95.3	-6.7	-1.5	0.0	0.0	0.0
H	95.6	-21.8	-1.6	0.0	0.0	0.0
I	96.2	-11.0	-1.1	0.0	0.0	1.4
J	93.9	-0.3	-2.2	1.8	-0.2	-0.7
K	96.6	-8.3	-0.7	0.0	1.3	2.5
L	96.6	-0.7	0.1	0.1	2.3	0.8
Mean	95.3	-6.5	-1.2	6.0	-2.1	-0.2
SD	1.8	6.7	1.3	9.4	6.6	3.8

Table 2.2: Dosimetric impact of needle insertion depth errors

eliminating the axial-to-sagittal alignment step necessary in the SAAR procedure. By eliminating the dependence on axial image stacks for organ segmentation, the SR3D-guided procedure could replace the clinical SAAR-guided procedure by making use of the pre- and post-needle insertion SR3D images for organ segmentation. After the pre-insertion SR3D image acquisition, the live 2D axial view may be used to monitor initial needle insertions to ensure mid-gland coverage, but would not be necessary otherwise. SR3D image acquisition takes less than 15 seconds, and the images have been shown to enable prostate segmentations with intra-operator variability on the order of 1 mm. [24] This procedure may improve overall segmentation accuracy while improving efficiency over conventional methods. Furthermore, the increased superior/inferior spatial resolution of the SR3D images may ease needle segmentation quality assurance, which currently must be performed using an axial image stack.

While this study did find advantages in SR3D over SAAR in terms of decreases in systematic insertion depth error, we identified a limitation of the method: a single post-needle insertion SR3D image volume is prone to shadow artifacts created by posterior

needles. The impact of these artifacts is evidenced by the 5 needles (3%) that needed to be excluded from analysis due to the inability to be detected, and the 10% of needles appearing obstructed in the SR3D images. We have shown that a user may manually detect a subset of unobstructed needles with insertion depth errors within 3 mm for 91% of needles. Our center is currently evaluating needle tip segmentation on live 2D sagittal images, which may be automatically transferred to the SR3D image coordinate system based on the current probe angle. This tool would provide the benefits of the live sagittal needle tip identification step, including the ability to identify tips working anteriorly-to-posteriorly and incorporating the dynamic information of the live 2D-view, while still eliminating the need to move the probe in the superior/inferior direction for final image acquisition. This method will also eliminate the possibility of needles being undetectable or extending beyond the edge of the SR3D image as observed in this study, since needles may be re-positioned at the time of tip identification to avoid these errors.

The mean±(standard error of the mean) insertion depth error of 2.8±0.2 mm corresponding to the SAAR-guided needle segmentation approach indicates a systematic shift of needle segmentations superior to the actual needle tip location within the axial image set. All needle tips are positioned relative to the final axial image set based on the axial-to-sagittal alignment step, which is performed using anatomical landmarks. It is possible that systematic errors in the axial-to-sagittal alignment are introduced by anatomical shifts caused by the insertion of HDR-BT needles. To assess the direction and degree of anatomical shifts created during the procedure, encoder positions of the pre-and post-insertion axial image sets were recorded for the last eight patients in the study. The post-insertion images were acquired to capture the same anatomical features as the pre-insertion images, so the difference in encoder values approximated anatomical shifts introduced between the imaging time points. Encoder values indicated a superior anatomical shift for all eight patients, with mean±SD of 12.6±5.4 mm. A su-

perior anatomical shift occurring between axial-to-sagittal alignment step and needle tip identification step may create a superior needle tip shift consistent with the observations in this study; however, further investigation into this effect is required.

In addition to superior/inferior anatomical motion observed in this study, the retraction of the TRUS probe required for the SAAR technique leads to the prostate shifting posteriorly (i.e. "drooping") over the tip of the probe as it is pulled from the rectum. This posterior shift could be partially observed in the co-registered axially- and sagitally-reconstructed 3D images in this study because the probe cover is thinner over the axial transducer than the sagittal transducer, leading to a small posterior shift in the axially-reconstructed images. Once the probe is fully retracted, this shift could be on the order of 2 cm (the probe diameter) and may lead to further needle tip localization uncertainty in the anterior/posterior direction for the SAAR technique, which was not measured in this study. The SR3D technique also eliminates this source of uncertainty in anterior/posterior needle tip positions.

A limitation of this study was the dependence on an external frame of reference (the insertion template) for comparison of needle insertion depth errors, when in actuality the needle tip position relative to the superior prostate border is the most critical distance for treatment planning accuracy. We did not investigate this distance in the current study due to a lack of consistent prostate segmentations produced using each imaging method. The external frame of reference allowed the use of the mechatronic device encoders for image and segmentation registration, and allowed the use of needle end-length measurements as a gold standard for insertion depths. Prior to final image acquisition, the needles were locked into place using a set screw on the template to prevent any further movement. The final axial image stack and SR3D volume were acquired consecutively for all patients; however it is possible that organ motion may have been introduced by moving the probe in the superior/inferior direction to acquire the final axial image stack.

A limitation of the dosimetric simulation conducted in this study is related to the lack of ground truth for needle tip positions and treatment dosimetry for both SAAR and SR3D techniques. We perturbed the SAAR-based needle tip positions and associated optimized dwell positions by the measured IDEs to illustrate the sensitivity of dosimetric covereage parameters on both SAAR and SR3D-based needle tip position uncertainty. In reality, dwell times and positions would need to be re-optimized based on the needle tip positions identified using SR3D imaging, which would lead to differences in the dosimetric parameters reported. However, this simulation does provide an estimate of the relative dosimetric impact of the IDEs measured using each imaging technique in this study.

Fianlly, another limitation of this study was the 5 mm sampling used to acquire the axial image sets for the SAAR-guided segmentations. Previous studies have investigated manual steppers that provide superior/inferior indexing in 1 mm steps in an effort to improve resolution in the sagittal plane [17, 18]. Resolution in this plane is fundamentally limited by the elevational resolution of the axial transducer. The transverse aperture of the BK 8848 transducer, which is related to this minimum resolution, is specified as 5.5 mm. Mechanical focusing may create a focal zone with finer elevational resolution; however, Peikari et al. showed that this thickness is highly sensitive to distance from the transducer, signal gain, and the presence of side-lobe artifacts produced by the transducer aperture [25]. While the elevational resolution of the sagittal transducer also limits the axial resolution of the SR3D reconstruction investigated in this study [19], the improved spatial resolution in the sagittal plane while maintaining acceptable resolution in the axial plane enables segmentation of the needles and organs respectively.

2.5   Conclusions

This study compared HDR-BT needle tip location, insertion depth errors, and the dosimetric impact of insertion depth errors on clinical treatment plans between SAAR and SR3D-guidance. The mechatronic device used for image acquisition enables the reconstruction of a 3D image by rotating the sagittal crystal, thereby eliminating the need to move the probe in the superior/inferior direction following needle tip identification. With current SAAR approaches, this probe movement must be compensated by performing an axial-to-sagittal registration introducing systematic uncertainty in needle tip location. Through comparison with calibrated needle end-length measurements, we have found that SR3D-guidance provides improved needle tip localization accuracy for the majority of needles relative to SAAR-guidance, leading to statistically significant improvements in dosimetric uncertainty. Ultrasound artifacts present in post-needle insertion SR3D images may limit segmentation accuracy for a subset of needles, and we have proposed a method to overcome this limitation for clinical implementation. These TRUS-based segmentation techniques also eliminate the need to adjust patient position for CT imaging, thereby decreasing patient discomfort and eliminating the probability of needle shifts occurring prior to treatment delivery.

References

1. Heidenreich, A. *et al.* EAU guidelines on prostate cancer. Part 1: Screening, diagnosis, and local treatment with curative intent - Update 2013. *European Urology* **65,** 124–137 (2014).

2. Hoskin, P. J. *et al.* GEC/ESTRO recommendations on high dose rate afterloading brachytherapy for localised prostate cancer: An update. *Radiotherapy and Oncology* **107,** 325–332 (2013).

3. Podder, T. *et al.* AAPM and ESTRO Guidelines for Image-Guided Robotic Brachytherapy : Report of Task Group 192. *Medical Physics* **41,** 101501 (2014).

4. Yamada, Y. *et al.* American Brachytherapy Society consensus guidelines for high-dose-rate prostate brachytherapy. *Brachytherapy* **11,** 20–32 (2012).

5. Marina, O. *et al.* Comparison of dose-escalated, image-guided radiotherapy vs. dose-escalated, high-dose-rate brachytherapy boost in a modern cohort of intermediate-risk prostate cancer patients. *Brachytherapy* **13,** 59–67 (2014).

6. Hoskin, P. J. *et al.* Randomised trial of external beam radiotherapy alone or combined with high-dose-rate brachytherapy boost for localised prostate cancer. *Radiotherapy and Oncology* **103,** 217–222 (2012).

7. Morris, W. J. *et al.* Low-dose-rate brachytherapy is superior to dose-escalated EBRT for unfavourable risk prostate cancer: The results of the ASCENDE-RT randomized control trial. *Brachytherapy* **14,** S12 (2015).

8. Hermesse, J. *et al.* A dosimetric selectivity intercomparison of HDR brachytherapy, IMRT and helical tomotherapy in prostate cancer radiotherapy. *Strahlentherapie und Onkologie* **185,** 736–742 (2009).

9. Georg, D. *et al.* Dosimetric considerations to determine the optimal technique for localized prostate cancer among external photon, proton, or carbon-ion therapy and high-dose-rate or low-dose-rate brachytherapy. *International Journal of Radiation Oncology Biology Physics* **88,** 715–722 (2014).

10. Tiong, A. *et al.* A small tolerance for catheter displacement in high-dose rate prostate brachytherapy is necessary and feasible. *International Journal of Radiation Oncology Biology Physics* **76,** 1066–1072 (2010).

11. Kolotas, C., Baltas, D. & Zamboglou, N. CT-based interstitial HDR brachytherapy. *Strahlentherapie und Onkologie* **175,** 419–427 (1999).

12. Hoskin, P. J., Bownes, P. J., Ostler, P., Walker, K. & Bryant, L. High dose rate afterloading brachytherapy for prostate cancer: catheter and gland movement between fractions. *Radiotherapy and Oncology* **68,** 285–288 (2003).

13. Mullokandov, E. & Gejerman, G. Analysis of serial CT scans to assess template and catheter movement in prostate HDR brachytherapy. *International Journal of Radiation Oncology Biology Physics* **58,** 1063–1071 (2004).

14. Kim, Y., Hsu, I. C. & Pouliot, J. Measurement of craniocaudal catheter displacement between fractions in computed tomography-based high dose rate brachytherapy of prostate cancer. *Journal of Applied Clinical Medical Physics* **8,** 2415 (2007).

15. Holly, R. *et al.* Use of cone-beam imaging to correct for catheter displacement in high dose-rate prostate brachytherapy. *Brachytherapy* **10,** 299–305 (2011).

16. Siebert, F.-A. A., Hirt, M., Niehoff, P. & Kovács, G. Imaging of implant needles for real-time HDR-brachytherapy prostate treatment using biplane ultrasound transducers. *Medical Physics* **36,** 3406–3412 (2009).

17. Schmid, M. *et al.* A phantom study to assess accuracy of needle identification in real-time planning of ultrasound-guided high-dose-rate prostate implants. *Brachytherapy* **12,** 56–64 (2013).

18. Batchelar, D. *et al.* Validation study of ultrasound-based high-dose-rate prostate brachytherapy planning compared with CT-based planning. *Brachytherapy* **13,** 75–79 (2014).

19. Tong, S., Downey, D. B., Cardinal, H. N. & Fenster, A. A three-dimensional ultrasound prostate imaging system. *Ultrasound in Medicine and Biology* **22,** 735–746 (1996).

20. Fenster, A., Downey, D. B. & Cardinal, H. N. Three-dimensional ultrasound imaging. *Physics in Medicine and Biology* **46,** R67–R99 (2001).

21. Bax, J. *et al.* A compact mechatronic system for 3D ultrasound guided prostate interventions. *Medical Physics* **38,** 1055–1069 (2011).

22. Damore, S. J., Syed, a. M. N., Puthawala, A. A. & Sharma, A. Needle displacement during HDR brachytherapy in the treatment of prostate cancer. *International Journal of Radiation Oncology Biology Physics* **46,** 1205–1211 (2000).

23. Helou, J. *et al.* High dose-rate brachytherapy boost for intermediate risk prostate cancer: Long-term outcomes of two different treatment schedules and early biochemical predictors of success. *Radiotherapy and Oncology* **115,** 84–89 (2015).

24. Hu, N., Downey, D. B., Fenster, A. & Ladak, H. M. Prostate boundary segmentation from 3D ultrasound images. *Medical Physics* **30,** 1648–1659 (2003).

25. Peikari, M. *et al.* Characterization of ultrasound elevation beamwidth artifacts for prostate brachytherapy needle insertion. *Medical Physics* **39,** 246–256 (2012).

Chapter 3

Simultaneous automatic segmentation of multiple needles using 3D ultrasound for high-dose-rate prostate brachytherapy

Automatic needle segmentation may decrease HDR-BT treatment times, thereby increasing the clinical feasibility of tumour-targeted treatments. The purpose of Chapter 3 is to present and characterize an algorithm designed to automatically segment all needles in an HDR-BT insertion using SR3D TRUS.

3.1   Introduction

High-dose-rate prostate brachytherapy (HDR-BT) dose distributions are critically sensitive to uncertainty in radiation source positions relative to the prostate and surrounding organs, which in turn depend on uncertainty in needle positioning [1–3]. For this reason, modern intra-operatively planned HDR-BT involves imaging needles in their final positions to localize trajectories and tips relative to anatomy [4]. Intra-operative imaging was originally performed using CT [5], but patient repositioning required for

CT acquisition was found to cause mean needle shifts of 11 mm between imaging and treatment delivery, and shifts of >20 mm in 10% of needles [6]. MRI-guided HDR-BT insertions have been proposed, but require patient repositioning for treatment [7, 8] or modified MRI suites for in-bore treatment [9, 10]. Trans-rectal ultrasound (TRUS)-guided HDR-BT techniques have been developed, enabling the segmentation of needles using multiple live 2D sagittal images and volumetric segmentation of organs using contiguous sets of axial images [11] thereby eliminating the need for patient repositioning between imaging and treatment [12, 13]. We recently completed a study investigating 3D TRUS-guided HDR-BT based on robotic sagittally-reconstructed 3D (SR3D) images [14], which are acquired by rotating the probe using a motor while simultaneously tracking probe position and acquiring sagittal images in a fan geometry [15, 16]. This method of image reconstruction mitigates tip localization uncertainty by eliminating the need to switch between sagittal and axial transducers or move the probe in the superior/inferior direction [14]. Increasing needle and organ segmentation accuracy remains a primary objective in HDR-BT imaging, but all imaging and segmentation must be performed intra-operatively, typically while the patient is under general anesthesia, adding a time constraint to the procedure. Since we have demonstrated that HDR-BT needles may be manually segmented accurately on a static SR3D image [14], an automatic HDR-BT needle segmentation algorithm may further decrease overall treatment time.

A number of investigators have proposed line detection algorithms for the segmentation of single needles in 3D ultrasound images *in vivo* showing promising performance for specific needle-guidance tasks [17–30]. Techniques have been proposed based on orthogonal projections [17, 20], geometric transformations such as parallel integral projections (PIP) [18], the 3D Hough transform (3DHT) [19, 24, 29, 30] and the generalized Radon transform [21–23], and iterative methods such as random sample consensus (RANSAC) [27, 28]. These techniques have all been validated using image

regions containing single needles; however, the algorithm requirements for HDR-BT needle segmentation, as discussed by Buzurovic et al. [31], have not been fully investigated. HDR-BT procedures involve multiple needles inserted through a rigid template placed on the perineum. Typical spacing between adjacent template holes is 5 mm, and needle and probe deflection between the template and imaged region can lead to uncertainty in needle placement greater than this spacing [32]. This uncertainty makes extrapolation from calibrated template hole positions infeasible for trajectory identification or sub-volume cropping to isolate regions containing individual needles, making existing algorithms unsuitable for HDR-BT needle segmentation.

The purpose of this study is to expand upon previous work by describing a needle segmentation algorithm designed for SR3D images containing multiple needles based on a version of the randomized 3DHT with additional regularization steps. The segmentation algorithm is validated using SR3D images from twelve prostate cancer patients that underwent HDR-BT including 190 needles. Algorithm-based segmentation results are compared geometrically to manual segmentation results, and the impact of SR3D image artifacts on algorithm performance is investigated.

3.2 Methods

3.2.1 Image Acquisition and Segmentation

Twelve intermediate-risk prostate cancer patients underwent conventional sagittally-assisted axially reconstructed (SAAR) ultrasound-guided HDR-BT using a compact mechatronic device to support the ultrasound probe and insertion template [15], enabling the acquisition of SR3D images of the prostate with all needles inserted. The imaging study was approved by the University of Western Ontario Health Sciences research ethics board. A Profocus 2202 ultrasound machine and 8848 bi-planar TRUS probe (BK Medical, Peabody MA, USA) operating at 9 MHz and 6.3 cm imaging depth

were used for image acquisition. Sagittal images were acquired over 140° at 0.5° angular intervals, resulting in images with size $870 \times 441 \times 408$ and $0.16 \times 0.16 \times 0.16$ mm^3 reconstructed voxel dimensions. SR3D image spatial resolution varies with distance from the probe, with the highest spatial resolution component in the direction radial from the transducer (r), and the lowest spatial resolution component in the reconstructed direction tangential to the direction of probe rotation (t). The device calibration and HDR-BT workflow have been described previously [14]. Following the procedure, a medical physicist manually segmented and labelled all needles present in the SR3D images using Brachyvision treatment planning software (Varian Medical Systems, Palo Alto CA, USA). The needle segmentations produced intra-operatively using SAAR-guidance were used for treatment planning and delivery, and were referenced during the manual SR3D segmentation procedure to ensure that each needle was labelled correctly. We limited our consideration to straight needle detection; however, in cases where needles appeared to bend, only the needle tip and most inferior observable point along the trajectory were selected to approximate a linear best-fit. These manual linear SR3D segmentations were then used as the gold-standard for validation of the segmentation algorithm.

The algorithm was used to segment all needles present in the SR3D images. The algorithm was implemented in MATLAB 2015a (MathWorks, Natick MA, USA) on a desktop PC running Windows 10 (Microsoft, Redmond WA, USA) with a 3.4 GHz Core i7-3770 CPU (Intel, Santa Clara CA, USA), 16 GB of RAM, and a GeForce GTX 660 graphics card (NVIDIA, Santa Clara CA, USA) with 2 GB of memory. As input, the algorithm required the post-insertion SR3D image and the number of needles inserted. Needle labelling also required manually identified axial needle intersection points to create correspondences between template hole labels and automatically identified trajectories. The execution times of each major algorithm component were recorded for each patient.

3.2.2   Segmentation Algorithm

Major steps of the algorithm are outlined in Figure 3.1. The 5 major assumptions of the algorithm are 1) needles appear brighter in the image than the local background, 2) all needles enter the image from the inferior edge, 3) needle trajectories are within 10° of being normal to the axial plane, 4) needle trajectories are separated from one another by ≥3 mm in the axial plane and therefore do not cross, and 5) for a given patient, all needles will have insertion depths within the range [-12 mm, 10 mm] relative to the median insertion depth for that patient. It should be noted that clinical practice may vary, leading to violations of assumptions 3-5); however, these parameter limits reflected our institutional practice and experience. Specific parameter limits were selected based on geometric analysis of the manual segmentations, provided in Appendix B.1. Major algorithm components are described in further detail in the following sections.
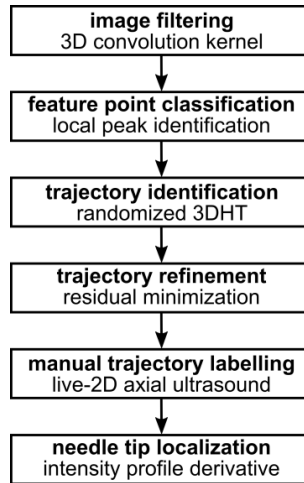
Figure 3.1: Flowchart indicating the major steps of the segmentation algorithm.

Image Filtering

A convolution filter was applied to the SR3D images based on the method proposed by Perona and Malik [33] designed to enhance edges with the same width as the needle cross section. The image is convolved with the second partial derivative of a Gaus-

sian distribution with the same width as the expected edge width. The primary needle insertion component is in the superior direction, so needles appear as edges in directions along the axial plane. The two primary spatial resolution components in the axial plane of the SR3D image are radial (r) and tangential (t) to the axis of probe rotation, corresponding to the axial and elevational resolution components of the sagittal transducer. The elevational spatial resolution is lower than the axial spatial resolution [34], resulting in the needles appearing smeared along the t direction as shown in Figure 3.2a. To account for this smearing, SR3D images were transformed to r, t coordinates as shown in Figure 3.2c, and two 3D convolution kernels were applied corresponding to second partial derivatives in the r and t directions respectively. The z component of both kernels was a uniform distribution, and the r and t directions were second partial derivatives of a 2D Gaussian distribution ($\Theta(r, t)$) with standard deviations of 0.4 mm and 1.2 mm, matching the typical r and t components of an axial needle cross section as shown in Figure 3.2d-e. The kernels had (r, t, z) dimensions of $1.2 \times 2.4 \times 10.0$ mm^3, and were applied in 0.16 mm steps in the r and t directions and 2 mm steps in the z direction. The results of the two convolutions were combined in quadrature to produce the final filtered signal intensities. The filter can be expressed as

$$I_{filtered}(r, t, z) = \sqrt{\sum_{i=1,2} \left(\frac{\partial^2}{\partial x_i^2} \Theta(r, t, z) \otimes I_{raw}(r, t, z) \right)^2} \tag{3.1}$$

where I_{raw} and $I_{filtered}$ are the unfiltered and filtered signal intensities, x_1 and x_2 are r and t directions, Θ is the convolution kernel, and $\otimes$ represents the convolution. Although SR3D image spatial resolution varies with distance from the probe (r), the convolution kernel dimensions were kept constant throughout the entire image.

Feature Point Classification

In order to isolate the centers of intensity peaks as needle feature points while minimizing the inclusion of additional surrounding points, local intensity peaks were identified
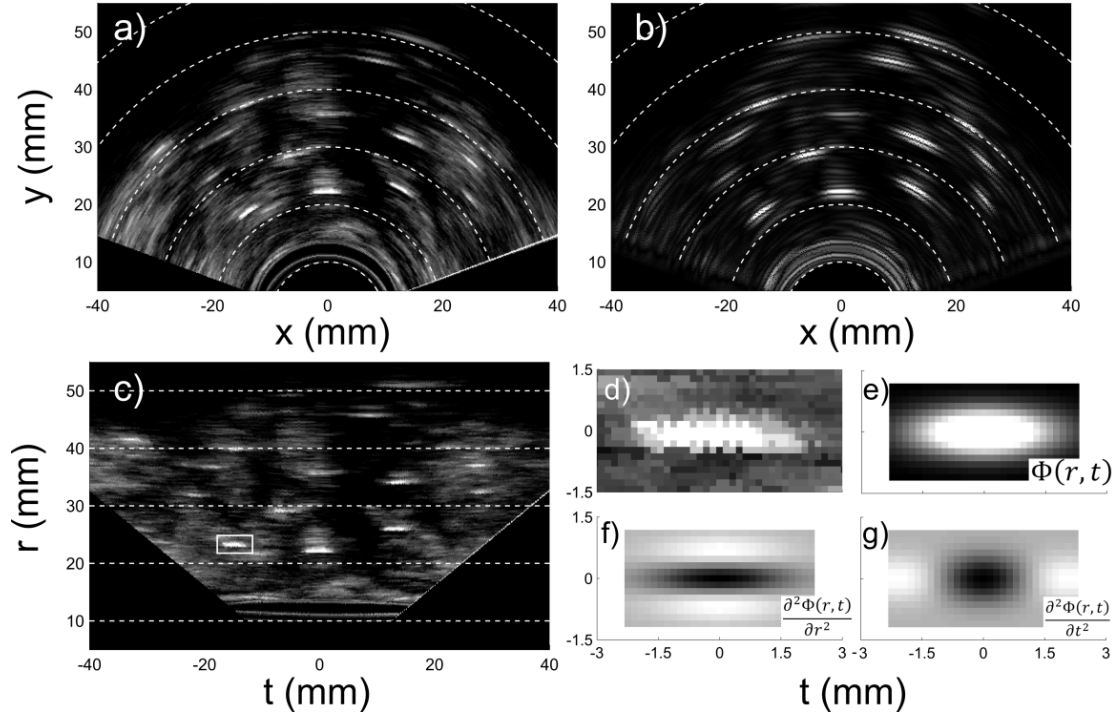
Figure 3.2: a-b) Example axial slice from an SR3D image before and after filtering. c) The unfiltered axial slice from a) transformed to the radial-tangential (r, t) coordinate system. Dotted grid-lines in a-c) indicate the t-direction in the image. d) Magnified view of the needle intersection point indicated by the white box in c). e) 2D Gaussian distribution with standard deviations in the r- and t-directions of 0.4 mm and 1.2 mm. f-g) Second partial derivatives of the 2D Gaussian distributions in the r- and t-directions.

in each axial slice while enforcing a minimum distance in the axial plane of 3 mm be-
tween adjacent peaks. First, an intensity threshold was selected as the 98th percentile
of the filtered image intensity values, and was applied to generate a set of candidate
feature points. Next, pairs of candidate feature points with separation distance in the
axial plane <3 mm were compared, and the voxel with the lowest signal intensity was
eliminated. This regularization step was parallelized and executed using a GPU.

Trajectory Identification

Needle trajectories were identified using the randomized 3DHT, similar to the method
described by Qiu et al. [35] extended to distinguish feature points corresponding to
multiple needles. The method involves randomly selecting pairs of feature points, cal-
culating the parameters of the line in 3D space that those feature points define, and
indexing an accumulator using those parameters. For our application, we chose the
point-orientation representation, which defines the line's orientation using the azimuthal
and elevational angles (ϕ, θ), and the line's position using a point along the line, specif-
ically the coordinates of the lines intersection point with a 2D axial plane (x_{int}, y_{int}) at
the inferior image face defined as $z = 0$. This parameterization is sufficient to charac-
terize all possible lines which intersect the inferior plane of the image volume using the
ordered 4-tuple $(\phi, \theta, x_{int}, y_{int})$.

Given a randomly selected pair of feature points $p_1[x_1, y_1, z_1]$ and $p_2[x_2, y_2, z_2]$, a
unit vector in the direction of the line defined by these points was calculated as $\hat{b} = (p_2 - p_1)/|p_2 - p_1|$. A minimum distance threshold of 10 mm in the z direction was
applied to point pairs to exclude highly oblique orientations, and $\hat{b}$ was multiplied by
the sign of the $\hat{b}_z$ component to ensure that $\hat{b}$ was oriented in the positive z direction.
The ordered 4-tuple $(\phi, \theta, x_{int}, y_{int})$ describing the line can be calculated according to
Eqs. 3.2-3.5.

$$\phi = tan^{-1}\left(\frac{b_x}{b_y}\right) \tag{3.2}$$

$$\theta = tan^{-1}\left(\frac{b_z}{\sqrt{b_x^2 + b_y^2}}\right) \tag{3.3}$$

$$x_{int} = x_1 - b_x z_1 \tag{3.4}$$

$$y_{int} = y_1 - b_y z_1 \tag{3.5}$$

The azimuthal angle ϕ could take any value from [180°, 180°], but the elevational angle was limited to the range [0°, 10°] from the z-axis. The x_{int} and y_{int} parameter values were limited to ranges of [-40 mm, 40 mm] and [10 mm, 60 mm], encompassing the area occupied by the template hole range used for all 12 patients plus lateral and anterior margins of 15 mm. Any lines with parameters outside of these limits were not entered in the accumulator. To index the accumulator, ϕ and θ were binned at 1° angular intervals and x_{int} and y_{int} were binned at 1 mm intervals. At these intervals, the 4D accumulator had a size of $360 \times 11 \times 81 \times 51$. Random point pair selection and accumulator indexing were parallelized and executed using the GPU, employing a constant 10^8 point pairs for each patient.

All feature points representing all lines in the 3D image were used as input in the 3DHT, leading to multiple accumulator peaks corresponding to multiple lines. The point-orientation line representation enabled the direct interpretation of the parameters x_{int} and y_{int} in terms of the image coordinate system, which could then be used to enforce a minimum distance in the axial plane between lines when identifying these peaks. This was accomplished by first only considering the x_{int} and y_{int} accumulator components, and identifying any local peaks with index values that were greater than an empirically selected threshold of 0.02% of the total number of random point pairs chosen. Next, local peaks were refined by comparing pairs of peak values with separa-

tion distance in the axial plane <3 mm and only retaining peaks with the greater index value; identical to the method used for axial feature point regularization. For each of the peaks identified using the x_{int} and y_{int} accumulator components, the corresponding ϕ and θ values were extracted as a secondary 2D accumulator, and the ϕ and θ values with the highest index were selected to define the line's orientation.

Trajectory Refinement

Trajectory orientations were refined using the method described by Qiu et al. [24], outlined in Figure 3.3. Feature points within 2 mm of each trajectory were identified, and the line that minimized the sum of the squared residuals with that set of feature points was determined by solving a set of derivative equations [24]. The trajectory identification step tended to identify a greater number of needle-like features than the true number of needles present in the image. To refine the set of candidate trajectories, the trajectories were sorted in descending order based on the number of feature points within 2 mm. Only the $1.5n$ trajectories with the greatest number of feature points were retained, where n was the number of needles physically inserted for that patient.

Manual Trajectory Labelling

Since the needle labelling step of the HDR-BT procedure is critical for treatment delivery, needles are inserted individually while monitoring a live 2D axial view of the prostate mid-gland. The dynamic view of each needle entering the image allows a user to reliably label each needle at the point of intersection with this axial slice. These intra-operatively identified intersection points were used to label the final set of needle trajectories identified by the algorithm as outlined in Figure 3.3. For this study, the manual label points were extracted from the SAAR needle segmentations produced intra-operatively, which were labelled using the live 2D axial view as described. 2D points were taken from a mid-gland axial slice of the SAAR segmentations, and these

manual label points were transferred to the SR3D image based on a rigid registration calculated using mechatronic device encoder positions. The intersection points of the candidate needle trajectories with the same axial slice were found, and the distances between each manual label point and candidate trajectory were calculated. Each candidate trajectory was labelled according to the nearest manual label point only if the manual label point was within 5 mm of the trajectory, ensuring that each label was only assigned to a single trajectory. Trajectories that were not labelled were discarded, and labels without a trajectory identified within 5 mm were reported as segmentation failures. This labelling procedure resulted in a final set of $\leq n$ trajectories, where n was the number of needles physically inserted for that patient.

Needle Tip Localization

Needle tip positions were determined using a two-step procedure based on the signal intensity profile along each needle trajectory and the practice of inserting needles to the prostate-bladder interface, limiting the range of insertion depths expected for each patient. First, drops in signal intensity corresponding to the needle tip were identified based on peaks in the derivative of the signal intensity profile as indicated in Figure 3.4. This involved cropping and filtering a small sub-volume oriented along each trajectory, then averaging intensity values normal to the trajectory to create a 1D intensity profile. The derivative of this profile was calculated and normalized by the maximum value. Peaks in the normalized derivative profile with values greater than a threshold of 0.7 were identified, and the needle tip was selected as the most superior of these peaks. The insertion depth of each needle was calculated as the distance along the trajectory from the inferior image edge to the identified tip. Details of the oriented sub-volume cropping, sub-volume filtering, and signal intensity profile analysis are provided in Appendix section B.2.

Next, the median value of these insertion depths was calculated, and a valid in-
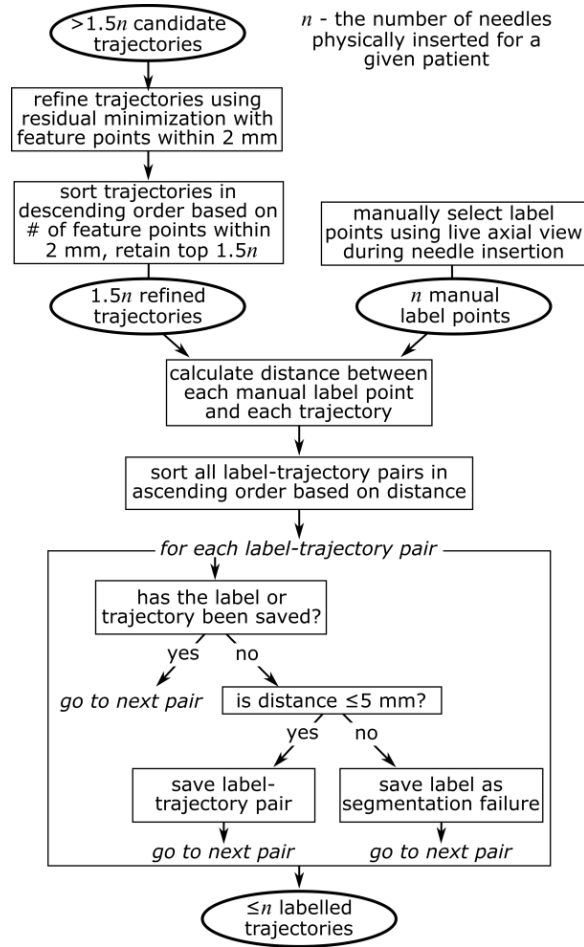
Figure 3.3: Process diagram of the trajectory refinement and manual label assignment steps. The input candidate trajectories were identified using the randomized 3DHT.

sertion depth search space was limited to the range [-12 mm, 10 mm] relative to this median value. The tip identification procedure was repeated for all needles over this limited search space to identify the final tip positions. The selection of these asymmetric search space limits was based on the observed insertion depth ranges of manual segmentations, as provided in Appendix section B.1.
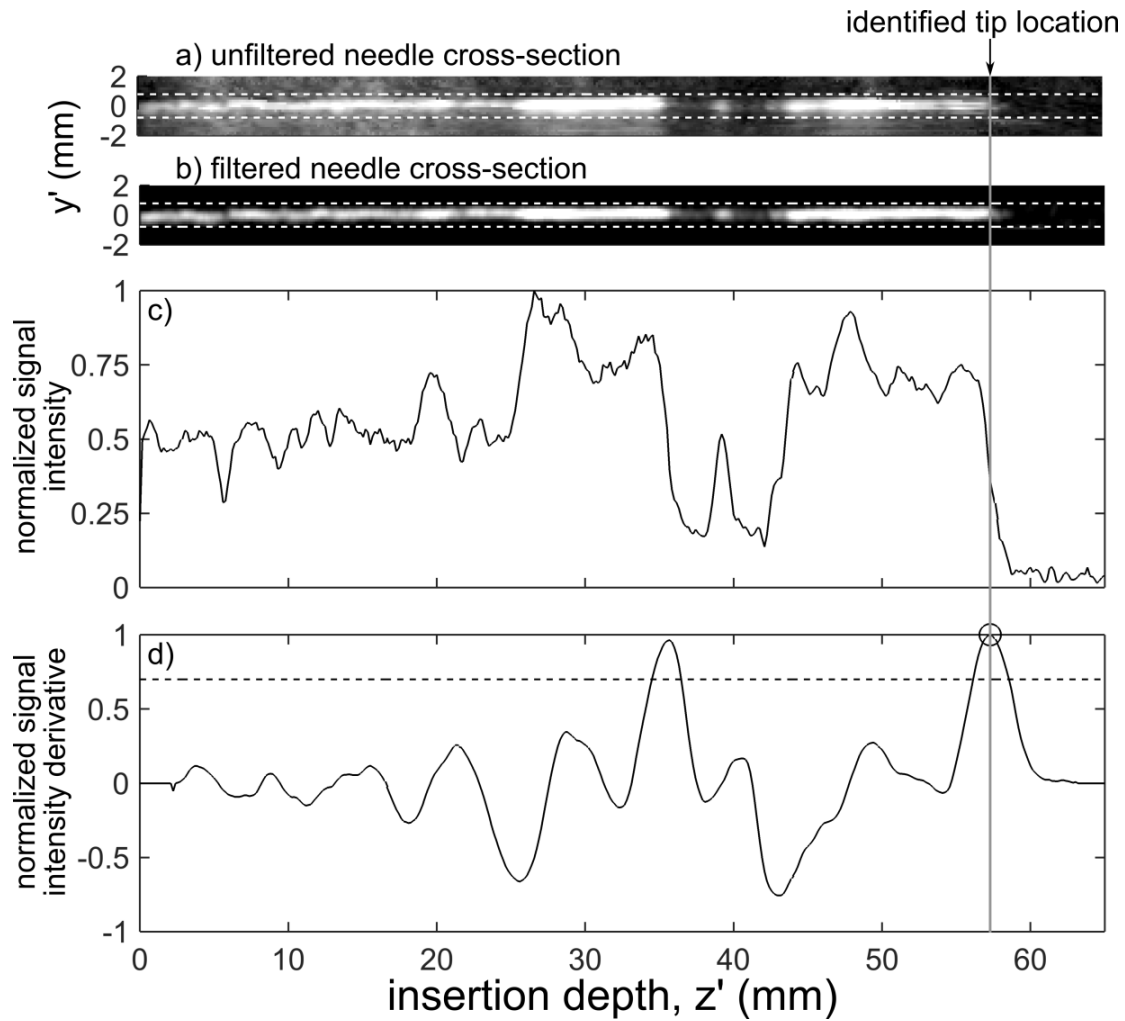
Figure 3.4: a-b) Example cropped needle cross section expressed in local line coordinates before and after filtering. The horizontal white dotted lines in a-b) indicate the y cropping limits used to create the 1D signal intensity profile. c) Normalized 1D signal intensity profile. d) Normalized signal intensity derivative profile. The horizontal dotted line indicates the derivative threshold used for selecting the tip location, which is indicated by the vertical grey line.

3.2.3 Segmentation Accuracy

Trajectory Localization Accuracy

Needle trajectories identified by the algorithm were compared with manual segmentations in terms of location and orientation. Let $p_m[p_{m,x}, p_{m,y}]$ and $p_a[p_{a,x}, p_{a,y}]$ be the 2D intersection points of the manual and algorithm-based segmentations with the inferior SR3D image face respectively. The trajectory location errors were characterized in terms of the 2D Euclidean distance in the axial plane $|\vec{d}_{traj}|$, where $d_{traj} = p_a - p_m$. This definition was chosen since $\vec{d}_{traj}$ is independent of needle insertion depth, and is the farthest point along the needle from the tip while remaining within the SR3D image. $\vec{d}_{traj}$ components were expressed in terms of r and t components at the point p_m. The rotation matrix used to calculate these components is described in Appendix B.3. Principal component analysis was used to determine the primary directions of trajectory error variance and 95% prediction interval ellipses (ellipse containing 95% of the points) [36, 37].

Let $\hat{b}_m$ and $\hat{b}_a$ be unit vectors pointing in the directions of the manual and algorithm-based segmentations respectively. Angular trajectory errors were defined as the angle α between $\hat{b}_m$ and $\hat{b}_a$, calculated using

$$\alpha = cos^{-1}(\hat{b}_m \cdot \hat{b}_a) \tag{3.6}$$

Tip Localization Accuracy

Let $t_m[t_{m,x}, t_{m,y}, t_{m,z}]$ and $t_a[t_{a,x}, t_{a,y}, t_{a,z}]$ be the needle tip positions of the manual and algorithm-based segmentations respectively. Needle tip errors were defined as the 3D Euclidean distance $|\vec{d}_{tip}|$, where $\vec{d}_{tip} = t_a - t_m$. The x and y components of $\vec{d}_{tip}$ were also rotated to be expressed in terms of r and t components at point t_m. Principal component analysis was used to determine the primary directions of tip error variance and 95%

prediction interval ellipsoids [36, 37].

Impact of Image Artifacts on Segmentation Accuracy

The medical physicist performing the manual segmentations subjectively classified each needle tip as obstructed, partially-obstructed, or unobstructed by shadow artifacts based on needle tip appearance. Unobstructed needles had a high needle tip-to-background contrast, and did not appear to enter any signal voids. Obstructed needles had low needle tip-to-background contrast in the vicinity of obvious signal voids. Partially-obstructed needles did not fit clearly into the other two categories, and typically had low tip-to-background contrast but did not enter any obvious signal voids. 3D tip errors of the automatic segmentations were stratified based on needle tip appearance, and median values were compared between groups. Statistical tests were performed in SPSS 23 (IBM, Armonk NY, USA).
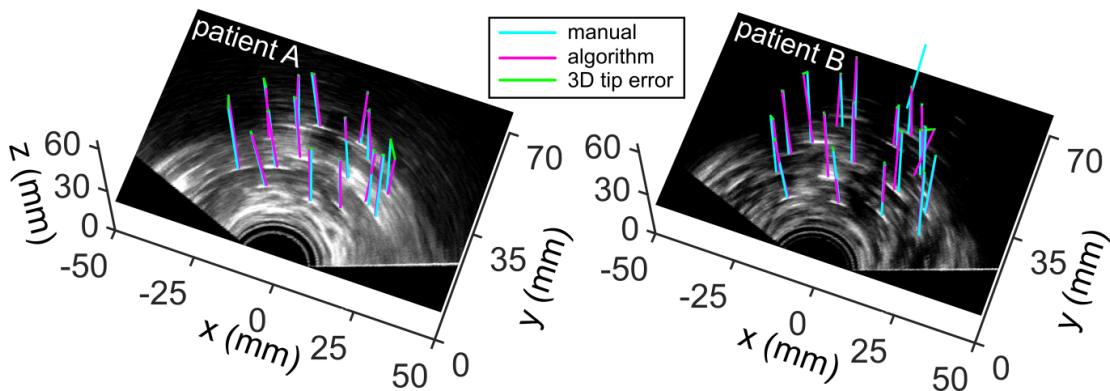
Figure 3.5: Example segmentations from two patients intersecting an axial slice of the SR3D image. The algorithm did not identify a trajectory for the most anterior needle from patient B indicated by the absence of a 3D tip error vector.

3.3 Results

Between 14 and 20 needles were inserted in each of the 12 patients for a total of 194. 191 of these needles were plastic FlexiGuide needles (Eckert and Ziegler Group, Berlin,

DE) with 2.00 mm diameter, and three were metal interstitial needles with 1.65 mm diameter. All 194 needles were used as input in the segmentation algorithm, but four needles were excluded from geometric analysis including the three non-plastic needles, and one needle that extended beyond the edge of the SR3D image due to incorrect probe placement prior to image acquisition. All 194 needle tips were detectable intra-operatively using 2D ultrasound imaging incorporated in the clinical SAAR procedure, so were included in the treatment plans. Execution times of the algorithm are listed in Table 3.1. The mean execution time was 11.0 s per patient, or 0.7 s per needle. Figure 3.5 shows example segmentations produced for two patients, indicating the 3D needle tip distances between manual and automatic segmentations. Treatment planning studies recommend needle tip localization accuracy within 3 mm [3] and previous HDR-BT imaging studies described tip errors in terms of 3 mm and 5 mm thresholds [12, 14] The geometric performance of the algorithm is summarized in terms of these thresholds in Table 3.2.

Algorithm component	Mean (SD) execution time per patient (s)
Image filtering	3.44 (0.08)
Image binarization	1.13 (0.07)
Trajectory identification	3.23 (0.14)
Trajectory refinement	0.013 (0.001)
Needle tip localization	3.23 (0.28)
Manual trajectory labeling*	0.003 (0.001)
Total	11.04 (0.22)

Table 3.1: Algorithm execution times. *Only includes computational time required to label candidate trajectories using manually identified points; does not include user interaction time required to identify points.

3.3.1   Trajectory Localization Accuracy

Figure 3.6a displays a histogram of the angular trajectory errors of the automatic segmentations. Of the 190 needle trajectories, 83%were identified by the algorithm within

3° of the corresponding manual segmentation. Figure 3.6b displays a histogram of 2D axial trajectory errors of the automatic segmentations. 91% of needle trajectories were segmented within 3 mm error. Figure 3.6c displays a 2D plot of r and t trajectory error components along with the 95% prediction interval ellipse. The mean [95% prediction intervals] of the distribution in (t, r) were 0.28 [-1.74, 2.30] mm and -0.08 [-0.89, 0.73] mm respectively. Two image artifacts incorrectly identified as needles had 2D trajectory errors >5 mm and were excluded from all 95% prediction interval calculations.

Error metric	% (#) of Needles
2D Axial trajectory error $\leq$ 3 mm	91 (173)
Trajectory angular error $\leq$ 3°	83 (157)
2D Axial tip error $\leq$ 3 mm	91 (172)
3D Tip error $\leq$ 3 mm	82 (155)
3D Tip error $\leq$ 5 mm	85 (161)
Reported failed segmentations*	6 (12)

Table 3.2: Algorithm performance for 190 needles. *Reported when no candidate needle trajectory is identified within 5 mm of the manually selected label point.
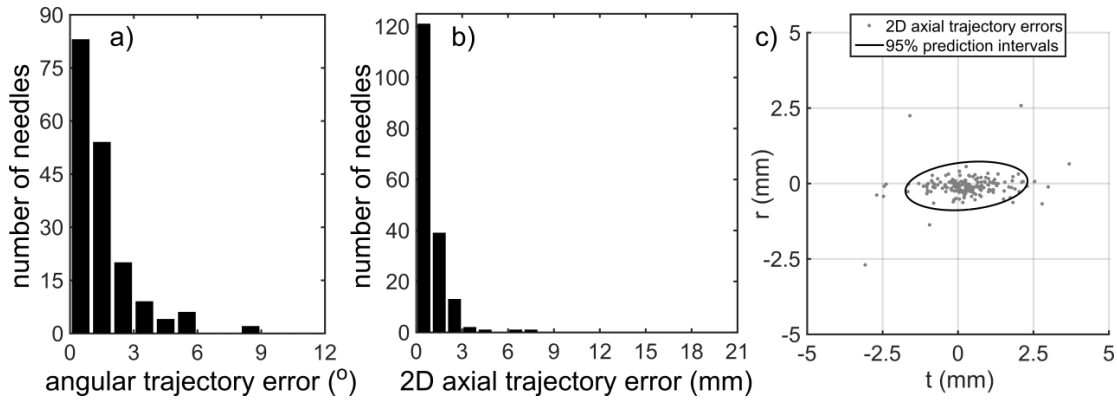
Figure 3.6: a)-b) Histograms of angular trajectory error and 2D axial trajectory error of automatically segmented needles relative to the corresponding manual segmentations. c) Plot of 2D axial trajectory error components expressed in terms of radial (r) and tangential (t) directions along with 95% prediction intervals. Two artifacts incorrectly identified as needles resulted in 2D axial trajectory errors >5 mm, so were excluded from c) and excluded from the 95% prediction interval calculation.

3.3.2 Tip Localization Accuracy

Figure 3.7a displays a histogram of 3D tip errors for the automatic segmentations. 82% of needle tips were segmented within 3 mm error and 85% were segmented within 5 mm error. Figure 3.7b displays a 3D plot of t, r, and z tip error components along with the 95% prediction interval ellipsoid. The mean [95% prediction intervals] of the distribution in (t, r, z) were 0.05 [-1.58, 1.67] mm, -0.07 [-0.65, 0.51] mm, and 0.35 [-6.23, 6.93] mm respectively. Figure 3.7c displays a highlighted view of the 2D tip error components in the r and t directions. 91% of needle tips were identified with 2D errors in the axial plane within 3 mm.

3.3.3 Impact of Image Artifacts on Segmentation Accuracy

Of the 178 automatically segmented needles, 143 (80%) needles were classified as un-obstructed, 20 (11%) as partially obstructed, and 15 (8%) as obstructed. Of the 12 needles reported as automatic segmentation failures, 1 (8%) was classified as unobstructed, 3 (25%) as partially obstructed, and 3 (25%) as obstructed. The remaining 5 (42%) were completely obstructed so could not be identified manually. Figure 3.8 displays histograms of 3D tip errors stratified by tip appearance for the automatic segmentations. Shapiro-Wilk tests indicated that the 3D tip errors were not normally distributed, with p <.001 for all groups. Medians (inter-quartile ranges) of the unobstructed, partially obstructed, and obstructed groups were 0.87 (1.03) mm, 1.49 (2.87) mm, and 1.54 (4.68) mm respectively. A non-parametric independent-samples Kruskal-Wallis test indicated a significant effect of tip appearance on median 3D tip error (p = .013), and post hoc Mann-Whitney U tests indicated a significant pairwise difference between the unobstructed and partially obstructed groups (p = .013) but not between the unobstructed and obstructed groups (p = .068), or obstructed and partially obstructed groups (p = .77). The percentage of needles segmented within 3 mm error in the unobstructed, partially obstructed, and obstructed groups was 92%, 65%, and 67% respectively.
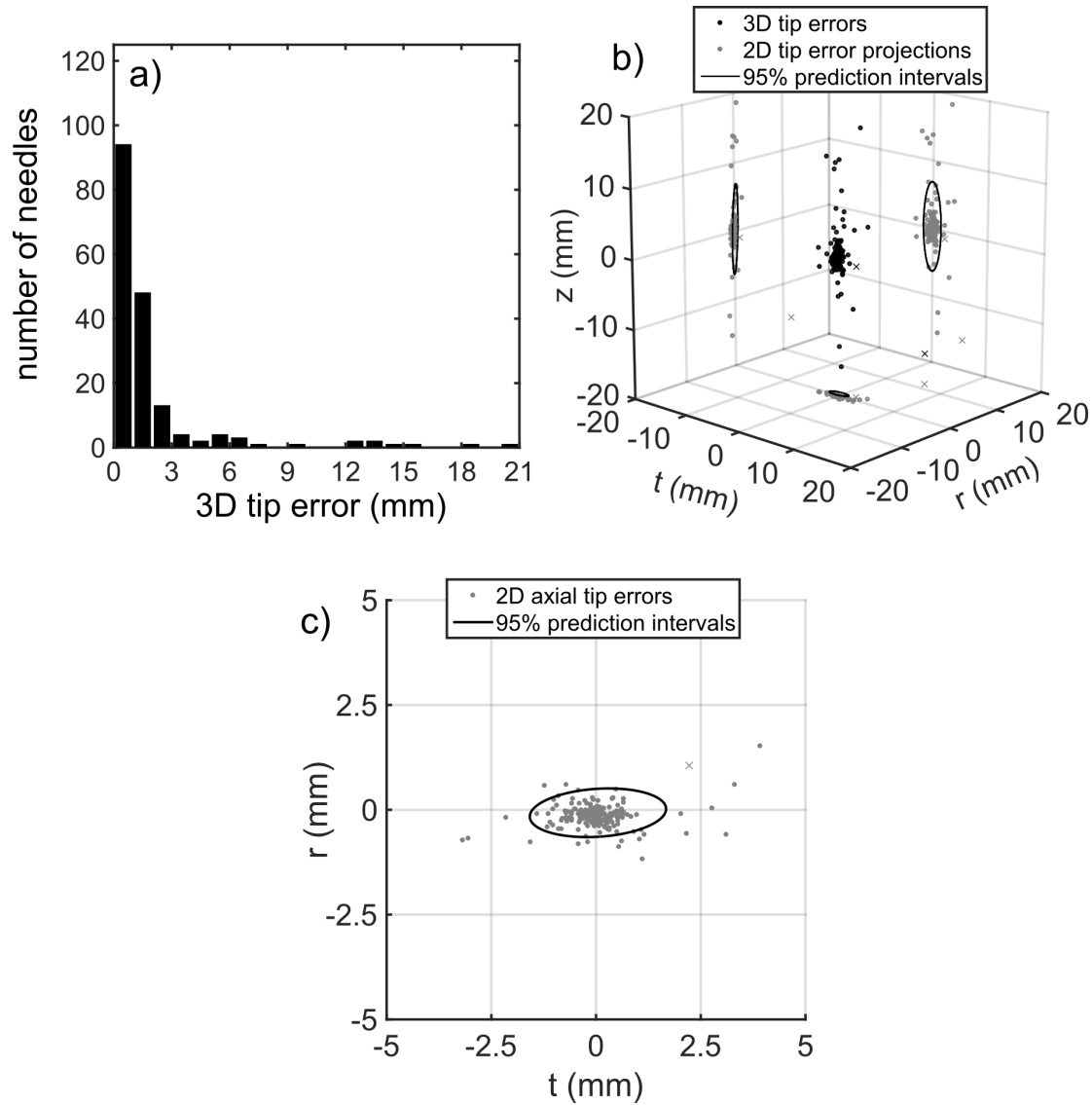
Figure 3.7: a) Histogram of 3D needle tip errors of automatically segmented needles relative to the corresponding manual segmentations. b) Plot of 3D needle tip error components expressed in terms of radial (r), tangential (t), and superior/inferior (z) directions along with 2D error projections and 95% prediction interval ellipsoid projections. c) Highlight of 2D axial needle tip error components along with 95% prediction interval ellipse. Two artifacts incorrectly identified as needles resulted 2D axial trajectory errors >5 mm, so are indicated by x-marks and were excluded from the 95% prediction interval calculations in b) and c).
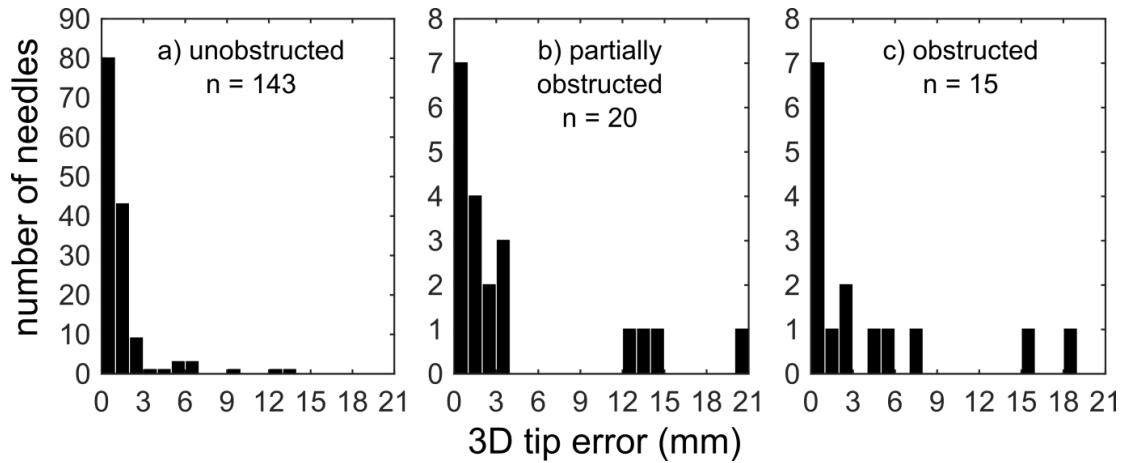
Figure 3.8: Histograms of 3D tip errors stratified by needle tip appearance manually classified by a medical physicist. The number of needles included in each histogram (*n*) is indicated.

3.4   Discussion

We have presented an algorithm designed to segment multiple needles present in a 3D ultrasound image simultaneously without requiring the user to crop regions of interest containing one needle each. The segmentation algorithm identified 82% and 85% of needle tips with 3D tip error ≤3 mm and ≤5 mm respectively, and results may be considered in the context of manual tip localization, which was found to lead to 1D insertion depth errors ≤3 mm and ≤5 mm in 83% and 92% of needles respectively when compared to needle end-length measurements [14]. The average algorithm execution time of 11.0 s per patient is sufficient for implementation in clinical HDR-BT workflows which typically take 1.5-3 hours. This algorithm was validated using sagittally-recontructed 3D ultrasound images, which have sub-millimeter resolution in the needle insertion direction. It would be possible to apply the trajectory localization portion of the algorithm to axially-reconstructed 3D ultrasound images; however, the accuracy of needle tip localization would likely decrease using these images due to decreased spatial resolution in the superior/inferior direction [34].

The 95% prediction intervals for the 3D tip errors were significantly larger in the

z-direction than the *r* or *t* directions, corresponding to the primary direction of needle insertion. This result suggests that tip localization remains a weakness of the algorithm. The *z* direction is also the primary error component for manual needle segmentation [14], suggesting that image quality may also limit current tip localization performance. The 95% prediction intervals for both the 2D axial tip errors and 2D axial trajectory errors were also larger in the *t* direction than the *r* direction. This result corresponds to the differences in spatial resolution in these two directions, which are limited by the axial and elevational spatial resolutions of the sagittal transducer, and suggests that segmentation performance could be improved in the *t*-direction by improving the transducers elevational resolution.

A limitation of the current algorithm is the potential for large segmentation errors in the presence of nearby hyper-echoic features and image artifacts such as reflections and shadows. For instance, three needles considered unobstructed had 3D tip errors >9 mm as shown in Figure 3.8a. Examination of these cases revealed that incorrect tip positions were identified due to calcifications superior to the tip in two cases, and the presence of a reflection artifact near the tip in one case. These segmentations errors indicate the need for manual quality assurance, which would add time intra-operatively. However, it would be possible to automatically display image cross-sections containing each needle trajectory using the algorithm results to expedite the manual quality assurance procedure. More advanced image-filtering techniques such as artificial neural networks may enable the distrinction between needles and calcifications by incorporating additional image features beyond those identified using the two convolution kernels employed in this study. [38]

The algorithm failed to identify 12 needles, representing an overall false negative rate of 6.3% of the 190 needles analyzed. Five of these needles (2.6%) also could not be detected manually due to the presence of shadow artifacts. The algorithm also incorrectly identified two image artifacts as needles representing a false positive rate of

1.0%. Altogether, the segmentation failure rate is 7.3%. Previous studies investigating automatic needle segmentation only evaluated single needles. One study employed filtered intensity based feature point classification and trajectory localization using the 3DHT, and reported segmentation failures for 30% of *in vivo* images containing single needles [24]. More recently, studies investigating phase grouping-based segmentation have reported failure rates as low as 4% for in vivo images containing single needles with optimized gain settings [26]. In the future, improvements in SR3D image-quality will likely be required to mitigate the potential for manual and automatic segmentation failures as observed for 2.6% and 7.3% of needles respectively in this study. The ability to segment all needles using 2D ultrasound during the clinical SAAR procedure suggests that incorporating these dynamic 2D images into the segmentation workflow may provide improvements in robustness. Previous investigators have proposed the use of 2D ultrasound for automatic segmentation of HDR-BT needles, but did not report results for images containing multiple needles [31] Based on observed limitations in SR3D image quality, a useful comparator of automatic segmentation variability would also be inter-observer variability, and manual segmentations averaged among observers would represent a superior gold standard to the segmentations from a single observer used in this study.

Another limitation of the algorithm is the set of physical constraints on the shape, orientation, and distribution of needles that can be segmented. In terms of shape, the current algorithm only models straight needles. Brachytherapy needles can deflect when inserted in tissue [32], and extensions of this algorithm may be required to model curvilinear needles to improve robustness. In terms of needle orientation, trajectories were limited to $\leq 10°$ from the axis of probe rotation (z-axis). This constraint reflected the needle trajectories we observed across patients, but may be violated when using an insertion template that allows larger insertion angles. In terms of needle distribution, a minimum 3 mm distance in the axial plane was enforced between adjacent needles,

which also may be violated depending on the insertion template used. Finally, the tip localization procedure constrained insertion depths to the range [-12 mm, 10 mm] relative to the median insertion depth for that patient. Insertion depths may vary significantly depending on practice; for instance, needles may be inserted into the seminal vesicles and extend superiorly beyond the prostate base. In these instances, insertion depth limits may need to be relaxed, creating the potential for larger insertion depth errors than observed in this study. It may be possible to accommodate a wider range of insertion depths using measurements of needle end-lengths protruding from the insertion template to calculate patient-specific insertion depth constraints. A calibration can also be performed to enable the direct calculation of insertion depths within the image using needle end-lengths, rather than relying solely on the SR3D image intensities [14, 39]. These measurements would add to the algorithm execution time, but have been shown to provide tip localization uncertainty of 0.7 mm in tissue mimicking phantoms [39], and are currently incorporated in commercially available imaging systems such as Oncentra Brachy (Elekta, Stockholm, SE). Other non-image-based techniques for brachytherapy needle localization include fiber Bragg gratings for curved trajectory reconstruction [40], and electromagnetic tracking for trajectory and tip localization [41]. Combining data from these techniques with image-based automatic needle segmentation may result in significant improvements in accuracy and robustness.

This study did not explicitly investigate the sensitivity of algorithm execution time and segmentation performance to algorithm parameter values. Beyond selecting parameter limits based on observed ranges, no further parameter optimization was performed for this patient cohort, limiting potential parameter over-fitting. The thresholds used to initialize the local peak identification algorithms used to identify feature points, accumulator peaks, and needle tips in section 3.2.2 were chosen empirically based on observed parameter ranges. In our experience, the local peak identification algorithms demonstrated low sensitivity to the thresholds used for initialization, but in the future

these specific threshold values should be validated using an independent image set.

3.5   Conclusions

We have presented an automatic needle segmentation algorithm for 3D ultrasound images containing multiple needles for high-dose-rate prostate brachytherapy treatment planning, and demonstrated the algorithm's geometric performance with images from 12 patients containing 190 needles. Accurate needle localization is critical for HDR-BT treatment planning. Automatic segmentation approaches will not replace manual approaches until equivalence or superiority in geometric accuracy and robustness can be demonstrated. However, segmentation algorithms that add negligible time to the procedure may still be of significant use for either manual segmentation initialization or quality assurance. The speed and geometric accuracy of the presented algorithm indicate that it may provide improvements in clinical workflow efficiency for modern 3D ultrasound-guided high-dose-rate prostate brachytherapy.

References

1. Mason, J., Al-Qaisieh, B., Bownes, P., Thwaites, D. & Henry, A. Dosimetry modeling for focal high-dose-rate prostate brachytherapy. *Brachytherapy* **13,** 611–617 (2014).

2. Siebert, F.-A. A., Hirt, M., Niehoff, P. & Kovács, G. Imaging of implant needles for real-time HDR-brachytherapy prostate treatment using biplane ultrasound transducers. *Medical Physics* **36,** 3406–3412 (2009).

3. Tiong, A. *et al.* A small tolerance for catheter displacement in high-dose rate prostate brachytherapy is necessary and feasible. *International Journal of Radiation Oncology Biology Physics* **76,** 1066–1072 (2010).

4. Hoskin, P. J. *et al.* GEC/ESTRO recommendations on high dose rate afterloading brachytherapy for localised prostate cancer: An update. *Radiotherapy and Oncology* **107,** 325–332 (2013).

5. Kolotas, C., Baltas, D. & Zamboglou, N. CT-based interstitial HDR brachytherapy. *Strahlentherapie und Onkologie* **175,** 419–427 (1999).

6. Holly, R. *et al.* Use of cone-beam imaging to correct for catheter displacement in high dose-rate prostate brachytherapy. *Brachytherapy* **10,** 299–305 (2011).

7. Ares, C. *et al.* Hypofractionated boost with high-dose-rate brachytherapy and open magnetic resonance imaging-guided implants for locally aggressive prostate cancer: A sequential dose-escalation pilot study. *International Journal of Radiation Oncology Biology Physics* **75,** 656–663 (2009).

8. Schick, U. *et al.* High-dose-rate brachytherapy boost to the dominant intraprostatic tumor region: hemi-irradiation of prostate cancer. *The Prostate* **71,** 1309–1316 (2011).

9. Ménard, C. *et al.* MRI-guided HDR prostate brachytherapy in standard 1.5T scanner. *International Journal of Radiation Oncology Biology Physics* **59,** 1414–1423 (2004).

10. Murgic, J. *et al.* Lessons learned using an MRI-only workflow during high-dose-rate brachytherapy for prostate cancer. *Brachytherapy* **15,** 147–155 (2016).

11. Schmid, M. *et al.* A phantom study to assess accuracy of needle identification in real-time planning of ultrasound-guided high-dose-rate prostate implants. *Brachytherapy* **12,** 56–64 (2013).

12. Batchelar, D. *et al.* Validation study of ultrasound-based high-dose-rate prostate brachytherapy planning compared with CT-based planning. *Brachytherapy* **13,** 75–79 (2014).

13. Morton, G. C. Prostate high-dose-rate brachytherapy: Transrectal ultrasound based planning, a technical note. *Practical Radiation Oncology* **5,** 238–240 (2015).

14. Hrinivich, W. T. *et al.* Three-dimensional transrectal ultrasound guided high-dose-rate prostate brachytherapy: A comparison of needle segmentation accuracy with two-dimensional image guidance. *Brachytherapy* **15,** 231–239 (2016).

15. Bax, J. *et al.* A compact mechatronic system for 3D ultrasound guided prostate interventions. *Medical Physics* **38,** 1055–1069 (2011).

16. Fenster, A. & Downey, D. B. Three-dimensional ultrasound imaging. *Annual Review of Biomedical Engineering* **2,** 457–475 (2000).

17. Aboofazeli, M., Abolmaesumi, P., Mousavi, P. & Fichtinger, G. A new scheme for curved needle segmentation in threedimensional ultrasound images. *Proceedings - 2009 IEEE International Symposium on Biomedical Imaging,* 1067–1070 (2009).

18. Barva, M., Uherčík, M. & Mari, J. Parallel integral projection transform for straight electrode localization in 3-D ultrasound images. *IEEE Transactions on Ultrasonics, Ferroelectrics, and Frequency Control* **55,** 1559–1569 (2008).

19. Beigi, P., Rohling, R., Salcudean, T., Lessoway, V. A. & Ng, G. C. Needle trajectory and tip localization in real-time 3D ultrasound using a moving stylus. *Ultrasound in Medicine and Biology* **41,** 2057–2070 (2015).

20. Ding, M. & Fenster, A. A real-time biopsy needle segmentation technique using Hough transform. *Medical Physics* **30,** 2222–2233 (2003).

21. Luengo Hendriks, C. L., Van Ginkel, M., Verbeek, P. W. & Van Vliet, L. J. The generalized Radon transform: Sampling, accuracy and memory considerations. *Pattern Recognition* **38,** 2494–2505 (2005).

22. Neshat, H. R. S. & Patel, R. V. Real-time parametric curved needle segmentation in 3D ultrasound images. *Proceedings of the 2nd International Conference on Biomedical Robotics and Biomechatronics,* 670–675 (2008).

23. Novotny, P. M. *et al.* GPU based real-time instrument tracking with three-dimensional ultrasound. *Medical Image Analysis* **11,** 458–464 (2007).

24. Qiu, W., Yuchi, M., Ding, M., Tessier, D. & Fenster, A. Needle segmentation using 3D Hough transform in 3D TRUS guided prostate transperineal therapy. *Medical Physics* **40,** 042902 (2013).

25. Qiu, W., Ding, M. & Yuchi, M. Electrode localization in 3D ultrasound images using 3D phase grouping and randomized Hough transform. *Proceedings - 4th International Conference on Genetic and Evolutionary Computing,* 202–205 (2010).

26. Qiu, W., Yuchi, M. & Ding, M. Phase grouping-based needle segmentation in 3-D trans-rectal ultrasound-guided prostate trans-perineal therapy. *Ultrasound in Medicine and Biology* **40,** 804–816 (2014).

27. Uherčík, M., Kybic, J., Liebgott, H. & Cachard, C. Model fitting using ransac for surgical tool localization in 3D ultrasound images. *IEEE Transactions on Biomedical Engineering* **57,** 1907–1916 (2010).

28. Uherčík, M., Kybic, J., Zhao, Y., Cachard, C. & Liebgott, H. Line filtering for surgical tool localization in 3D ultrasound images. *Computers in Biology and Medicine* **43,** 2036–2045 (2013).

29. Zhao, S., Qiu, W., Ming, Y. & Ding, M. Needle segmentation in 3D ultrasound images based on phase grouping. *Progress in Biomedical Optics and Imaging - Proceedings of SPIE,* 7497 (2009).

30. Zhou, H., Qiu, W., Ding, M. & Zhang, S. Automatic needle segmentation in 3D ultrasound images using 3D improved Hough transform. *Progress in Biomedical Optics and Imaging - Proceedings of SPIE,* 6918 (2008).

31. Buzurovic, I., Misic, V. & Yu, Y. Needle identification in high-dose-rate prostate brachytherapy using ultrasound imaging modality. *Proceedings of the Annual International Conference of the IEEE Engineering in Medicine and Biology Society,* 476–479 (2012).

32. Wan, G., Wei, Z., Gardi, L., Downey, D. B. & Fenster, A. Brachytherapy needle deflection evaluation and correction. *Medical Physics* **32,** 902–909 (2005).

33. Perona, P. & Malik, J. Scale-space and edge detection using anisotropic diffusion. *IEEE Transactions on Pattern Analysis and Machine Intelligence* **12,** 629–639 (1990).

34. Peikari, M. *et al.* Characterization of ultrasound elevation beamwidth artifacts for prostate brachytherapy needle insertion. *Medical Physics* **39,** 246–256 (2012).

35. Qiu, W., Ding, M. & Yuchi, M. Needle segmentation using 3D quick randomized hough transform. *Proceedings - The 1st International Conference on Intelligent Networks and Intelligent Systems,* 449–452 (2008).

36. Irwin, M. R., Downey, D. B., Gardi, L. & Fenster, A. Registered 3-D ultrasound and digital stereotactic mammography for breast biopsy guidance. *IEEE Transactions on Medical Imaging* **27,** 391–401 (Mar. 2008).

37. Karnik, V. V. *et al.* Evaluation of inter-session 3D-TRUS to 3D-TRUS image registration for repeat prostate biopsies. *Medical Physics* **38,** 1832–1843 (2011).

38. Jiang, J., Trundle, P. & Ren, J. Medical image analysis with artificial neural networks. *Computerized Medical Imaging and Graphics* **34,** 617–631 (2010).

39. Zheng, D. & Todor, D. A. A novel method for accurate needle-tip identification in trans-rectal ultrasound-based high-dose-rate prostate brachytherapy. *Brachytherapy* **10,** 466–473 (2011).

40. Borot De Battisti, M. *et al.* Fiber Bragg gratings-based sensing for real-time needle tracking during MR-guided brachytherapy. *Medical Physics* **43,** 5288–5297 (2016).

41. Poulin, E., Racine, E., Binnekamp, D. & Beaulieu, L. Fast, automatic, and accurate catheter reconstruction in HDR brachytherapy using an electromagnetic 3D tracking system. *Medical Physics* **42,** 1227–1232 (2015).

Chapter 4

Improved high-dose-rate prostate brachytherapy needle tip localization using live two-dimensional and sagittally-reconstructed three-dimensional ultrasound

Manual and automatic HDR-BT needle tip localization accuracy using SR3D TRUS is limited by shadow artifacts. The purpose of Chapter 4 is to present and characterize a needle segmentation technique combining live-2D sagittal and SR3D TRUS to mitigate the impact of shadow artifacts on needle tip localization.

The contents of this chapter have been submitted for publication in *Brachytherapy* and are currently under peer-review. Permission to reproduce this article for the purpose of this thesis is retained under the Elsevier author copyright agreement.

4.1   Introduction

High-dose-rate prostate brachytherapy (HDR-BT) is used routinely as a boost to external beam radiation therapy (EBRT) [1–4] and increasingly as a monotherapy [5–7]. Evidence suggests that it is possible to deliver dose distributions using HDR-BT with decreased dose to normal tissue [8] and decreased dosimetric uncertainty [9] than low-dose-rate prostate brachytherapy, but achieving these treatment plan characteristics is critically dependent on accurately localizing HDR-BT needles relative to anatomy

[10–12]. Image-guidance for HDR-BT has been implemented using CT [13], MRI [14, 15], and trans-rectal ultrasound (TRUS) [16, 17]. Patient repositioning for imaging, as required for conventional CT- and MRI-guided workflows, has been shown to cause caudal needle shifts prior to treatment [18]. In-bore treatments have been proposed, but lowering patients legs to fit in the bore may compromise access to the perineum and increase pubic arch interference [19]. TRUS-guided HDR-BT workflows allow needle insertion, imaging, and treatment to be completed in existing brachytherapy bunkers without the need to reposition the patient [16, 17]. TRUS-guidance has demonstrated comparable needle tip localization accuracy [16] and treatment plan dosimetry to CT-guidance [20]; however, conventional multi-step TRUS-guided procedures create the potential for needle tip localization errors for some patients.

Conventional TRUS-guided HDR-BT makes use of live-2D sagittal images to localize needle tips at the time of insertion [10]. Accurate organ dose calculation requires reconstruction of a 3D image, which is typically performed by acquiring multiple axial images while stepping the probe in the superior/inferior direction [16]. Information from the two imaging planes is then combined through an alignment of the axial organ segmentations with a live-2D sagittal view, introducing a source of uncertainty in the final needle tip positions relative to anatomy. This sagittally-assisted axially-reconstructed (SAAR) workflow is outlined in Figure 4.1a. An alternative TRUS-guided approach was proposed making use of sagittally-reconstructed 3D ultrasound (SR3D), which is produced by rotating the probe using a motor while simultaneously capturing a fan of sagittal images that are reconstructed into a 3D image with sub-millimeter resolution in the needle insertion direction [21, 22], eliminating the need to combine axial and sagittal views. Custom hardware and software solutions have been presented for SR3D reconstruction [22], and vendors including Varian Medical Systems (Palo Alto CA) and Elekta (Stolkholm SE) have introduced technologies with similar SR3D reconstruction capabilities. It was demonstrated that HDR-BT needles could be

segmented using SR3D images with insertion depth errors ≤5 mm for 93% of needles, *versus* 76% when using the conventional SAAR-technique [23]. Unfortunately, shadow artifacts were found to introduce uncertainty in needle tip locations when using a single post-insertion SR3D image, leading to insertion depth errors >10 mm in 3% of needles and completely obstructing the view of an additional 3% of needles, impacting 4 out of 12 patients in the study [23]. Although these artifacts impacted a relatively small number of needles, the potential for large errors limited the utility of single post-insertion SR3D images for localizing all HDR-BT needles.

The clinical SAAR approach is not as susceptible to these image artifacts due to the incorporation of live-2D sagittal imaging to localize needle tips at the time of insertion. The live-2D technique enables the identification of needle tips as the needles are inserted from the prostate anterior-to-posterior, effectively eliminating the impact of shadow artifacts caused by posterior needles on tip localization [16]. The SAAR-guided technique incorporating live-2D tip identification was found to lead to larger insertion depth errors than the SR3D approach for most needles; however, we found that these errors were attributed to superior/inferior probe motion required for axially-reconstructed 3D (AR3D) ultrasound introducing uncertainty in tip positions relative to organs [23].

Based on the characteristics of SR3D images and live-2D sagittal images, we have investigated a sagittally assisted sagittally reconstructed (SASR) needle segmentation workflow outlined in Figure 4.1b. The SASR workflow is designed specifically to eliminate uncertainty created by probe movement when switching between axial and sagittal transducers required for the conventional SAAR technique, and to mitigate the impact of shadow artifacts created by posterior needles in SR3D images. The purpose of this study is to validate the SASR needle segmentation method, and compare it to the conventional SAAR-guided approach geometrically using calibrated needle end-length measurements [23, 24] as the gold-standard.

4.2   Materials and Methods

4.2.1   Needle Segmentation Techniques

Conventional Technique: Sagittally-Assisted Axially-Reconstructed (SAAR)

The steps of the SAAR technique are outlined in Figure 4.1a, and have been described previously [16, 23]. Briefly, the technique begins by acquiring an axially-reconstructed 3D image (AR3D) prior to needle insertion by stepping the probe in the inferior direction from the bladder to prostate apex in 1-5 mm intervals. This initial AR3D image is used to segment the prostate, urethra, rectum, and bladder. Needles are then inserted to the prostate mid-gland using a live-2D axial view to verify coverage in the left/right and anterior/posterior directions. The probe is then manipulated to acquire a live-2D sagittal view of the prostate, including the base and apex. To maintain a geometric relationship between the AR3D and live-2D sagittal images, the axial organ contours must be aligned in the superior/inferior direction with this live 2D sagittal view. Following organ alignment, each needle is identified using the live 2D sagittal view by rotating the probe, then advanced to the superior edge of the prostate. Needle tip positions are localized at the time of insertion using live 2D sagittal images. Needle advancement and tip localization are performed from prostate anterior-to-posterior to mitigate the impact of shadow artifacts. Once all needles have been advanced, a second AR3D image is acquired attempting to match the anatomical landmarks present in the original image and compensating for superior prostate movement caused by the insertion, which tends to be ~1.3 cm [23]. Needle trajectories are edited using the final AR3D image to account for out-of-plane trajectories not captured by the live 2D sagittal images, but needle insertion depths are not modified due to limited spatial resolution in the superior/inferior direction.

Proposed Technique: Sagittally-Assisted Sagittally-Reconstructed (SASR)

The steps of this technique are outlined in Figure 4.1b, and are similar to the steps of the SAAR technique but make use of SR3D images in place of AR3D images. Specifically, an SR3D image is acquired prior to needle insertion to aid prostate, urethra, rectum, and bladder segmentation. Needles are inserted to prostate mid-gland using a live-2D axial view identical to the SAAR technique, and each needle is localized and advanced to the prostate-bladder interface using live-2D sagittal images. This localization is performed from prostate anterior-to-posterior, and needle tip positions are recorded at the time of insertion using custom software, making use of the probe angle to calculate the anterior/posterior and left/right position of each needle. Following advancement of all needles, a final SR3D image is acquired with sub-millimeter spatial resolution in the superior/inferior direction. This image is then used for final organ segmentation, and needle tips and trajectories are adjusted to account for potential out-of-plane trajectories and additional tip motion relative to anatomy introduced by the insertion of adjacent needles.

4.2.2 Image Acquisition and Segmentation

Intra-Operative Imaging and Segmentation Workflow

Ten prostate cancer patients underwent TRUS-guided HDR-BT using a Profocus 2202 ultrasound machine and 8848 bi-planar probe (BK Medical, Boston MA) operating at 9 MHz. The probe was supported by a custom compact mechatronic device enabling SR3D image acquisition [22], and the ultrasound machine video output was captured by two systems simultaneously: 1) a computer running Vitesse 2.5 (Varian Medial Systems, Palo Alto CA) for conventional SAAR-guided segmentation by one user, and 2) a computer running custom software for parallel SASR-guided segmentation by an additional user. Both the SAAR and SASR techniques involve identifying needle tips
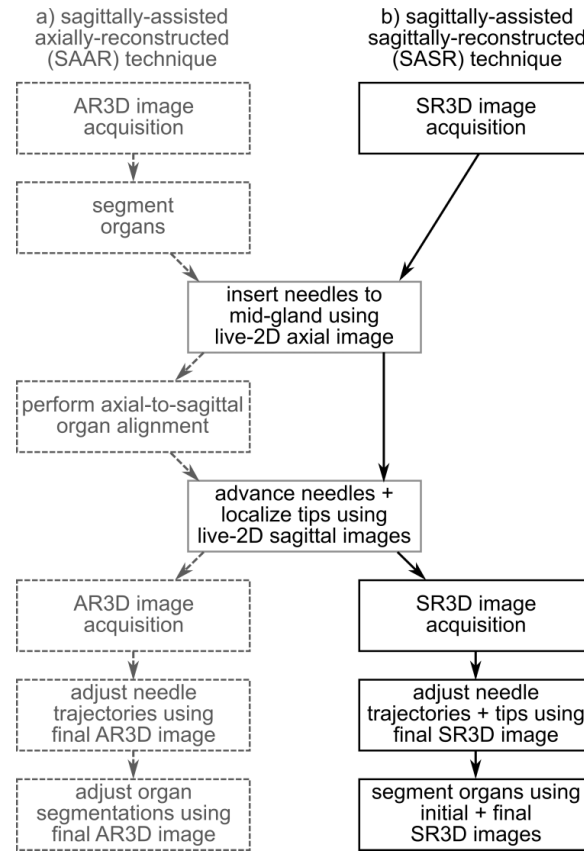
Figure 4.1: Flow chart outlining the SAAR and proposed SASR needle segmentation workflows. The steps common to both procedures involving the insertion and advancement of needles are placed in the middle of the flow chart.

using the live-2D sagittal view as they are inserted from prostate anterior-to-posterior, so this step was completed simultaneously by both users as needles were being inserted. Following insertion, an SR3D image was acquired spanning 140° at 0.5° angular intervals, followed by an AR3D image acquired at 5 mm intervals. The superior/inferior position of the probe was recorded during all image acquisitions. The SAAR-guided segmentations were used for intra-operative treatment planning and delivery. Following insertion, the lengths of needle ends protruding from the template were measured to calculate insertion depth errors (*IDE*s) for each technique. All segmentations were anonymized and exported to MATLAB 2015b (Mathworks, Natick MA) for analysis. This study was approved by the University of Western Ontario Health Sciences research

ethics board.
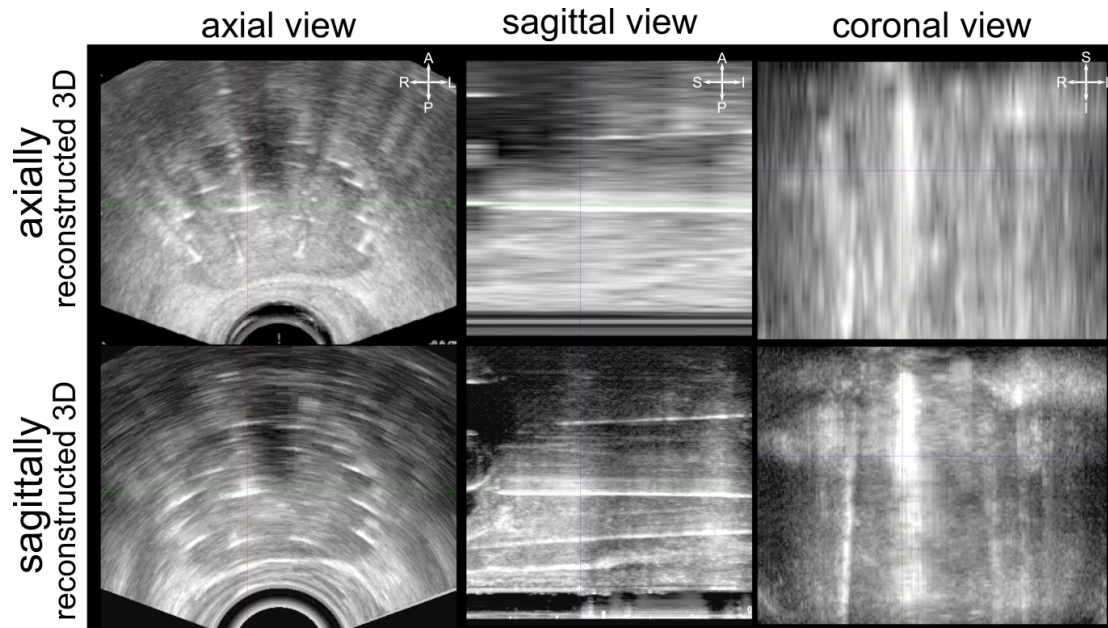
Figure 4.2: Example co-registered axially-reconstructed 3D (AR3D) and sagittally-reconstructed 3D (SR3D) images from a single patient following needle insertion.

Multi-User Tip and Trajectory Adjustment Using SR3D Images

Following HDR-BT procedures, all SR3D images and live-2D based needle segmentations were imported into Brachyvision treatment planning software (Varian Medical Systems, Palo Alto CA) for needle tip and trajectory adjustments. Beginning with the intra-operative live-2D based needle segmentations, each needle trajectory and tip was adjusted using the final SR3D image twice by two separate users, resulting in four individual SR3D-based segmentations for each needle. At least one week transpired between the first and second segmentation adjustments for each patient by each user. At the time of segmentation adjustment each user also subjectively scored each needle based on its appearance on the SR3D image. These tip scores were assigned to enable estimation of the impact of image artifacts on intra- and inter-operator variability in SR3D-based tip localization. Criteria for selecting tip scores was predominantly based

on the presence or absence of shadow artifacts appearing in the vicinity of the needle tip, and tip scores of 0-3 were assigned to each needle in order of increasing tip visibility according to the criteria provided in Table 4.1 and illustrated in Figure 4.3. Distinguishing between tip scores 1 and 2 was performed using a circular cursor with 3 mm radius that could be placed at each manually selected tip position, allowing the user to estimate whether uncertainty in tip position was within the cursor area (tip score 2), or exceeded the cursor area due to the presence of artifacts (tip score 1). Tip score 3 was included to allow for the identification of needles that did not appear to enter any image artifacts for the entire length. We expected the lowest segmentation uncertainty for this group of needles, and associated systematic error would be a potential indicator of calibration errors in device encoders or analysis software. A unique tip score was assigned to each needle each time it was segmented, resulting in four scores per needle. A single score for each needle was found by selecting the minimum of the four scores, representing the most conservative classification of tip appearance. For instance, a needle would only receive a final tip score of 3 if it received a score of 3 for all four individual tip adjustment trials.

Tip score	0	1	2	3
Definition	needle tip is **not** visible on SR3D image	needle tip is visible on SR3D image, user is **not** confident in tip position with ≤3 mm uncertainty	needle tip is visible on SR3D image, user is confident in tip position with ≤3 mm uncertainty	needle tip is visible on SR3D image, user is confident in tip position with ≤3 mm uncertainty, image artifacts absent for entire trajectory and tip
% (#) of Needles	8.8 (13)	38.8 (57)	42.9 (63)	9.5 (14)

Table 4.1: Needle tip score definitions and detection frequencies.
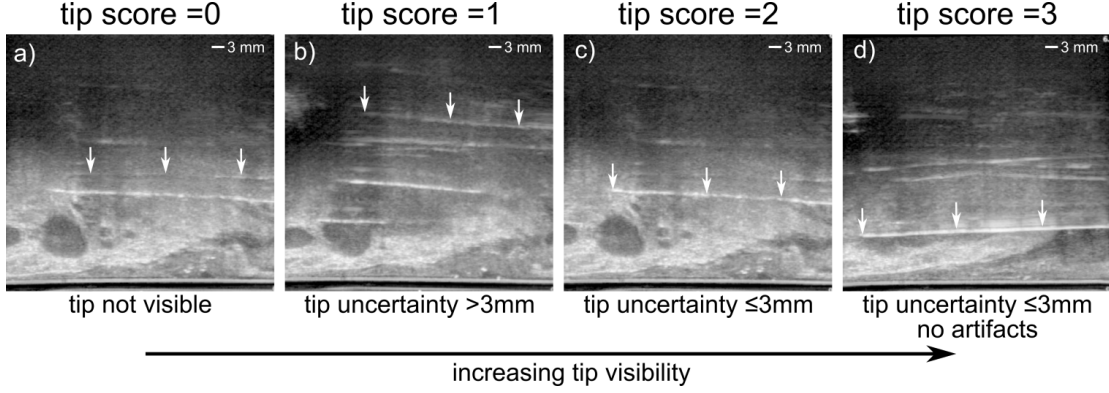
Figure 4.3: Examples of needles appearing in an SR3D image from a single patient with different tip scores based on visibility on the final SR3D image. The needles are arranged from lowest tip visibility (tip score 0) to highest (tip score 3).

4.2.3 Segmentation Analysis

Difference Between Live-2D and SR3D-based Tip Positions

Since the SASR procedure enables the adjustment of live-2D based tip positions using the final SR3D image, tip positions were analyzed to characterize the magnitude and direction of these adjustments. We indicate the live-2D based tip position of each needle as $\vec{t}_{2D}$, and indicate individual SR3D-based tip positions of each needle as $\vec{t}_{3D}(i, j)$, where $i = 1, 2$ indicates the user, and $j = 1, 2$ indicates the trial. The mean value of $\vec{t}_{3D}$ for each needle across users and trials, $\vec{t}_{3Dm}$, was calculated as

$$\vec{t}_{3Dm} = [\vec{t}_{3D}(1, 1) + \vec{t}_{3D}(1, 2) + \vec{t}_{3D}(2, 1) + \vec{t}_{3D}(2, 2)]/4 \tag{4.1}$$

The mean tip adjustment $\vec{d}_{adj}$ was calculated for each needle as

$$\vec{d}_{adj} = \vec{t}_{3dm} - \vec{t}_{2D} \tag{4.2}$$

Needles were stratified based on tip scores, and principal component analysis of $\vec{d}_{adj}$ was performed to calculate the 95% prediction intervals of the mean tip adjustments. Since the live-2D based needle segmentations were produced using 2D images oriented

radially from the axis of probe rotation, tip adjustments were expressed in terms of in-plane directions radial (r) and parallel (z) to the axis of probe rotation, and the out-of-plane direction tangential (t) to the axis of probe rotation.

Intra- and Inter-Operator Variability in SR3D-based Tip Positions

Intra-operator variability was assessed by calculating the average difference in $\vec{t}_{3D}$ between trials, within users. Specifically, the distance $\vec{d}_{intra}$ was calculated for each needle as

$$\vec{d}_{intra} = ([\vec{t}_{3D}(1,2) - \vec{t}_{3D}(1,1)] + [\vec{t}_{3D}(2,2) - \vec{t}_{3D}(2,1)])/2 \qquad (4.3)$$

Similarly, inter-operator variability was assessed by calculating the average difference in $\vec{t}_{3D}$ between users, within trials. The distance $\vec{d}_{inter}$ was calculated for each needle as

$$\vec{d}_{inter} = ([\vec{t}_{3D}(2,1) - \vec{t}_{3D}(1,1)] + [\vec{t}_{3D}(2,2) - \vec{t}_{3D}(1,2)])/2 \qquad (4.4)$$

Needles were stratified based on tip scores, and principal component analysis of $\vec{d}_{intra}$ and $\vec{d}_{inter}$ was performed to calculate the 95% prediction intervals of the components of intra- and inter-operator variability. Similar to the mean tip adjustments, $\vec{d}_{intra}$ and $\vec{d}_{inter}$ were expressed in terms of directions radial (r), tangential (t), and parallel (z) to the axis of probe rotation.

Impact of SR3D-based Adjustments on Insertion Depth Errors

The method for calculating *IDE*s has been described previously and requires calibrating the superior/inferior mechatronic device encoders using a phantom [23]. This calibration enables the calculation of expected needle tip position based on 1) the probe position during image acquisition, 2) the total needle length, and 3) the length of the needle

end protruding from the template following insertion [23, 24]. *IDE*s are calculated as the difference in insertion depths between the image-based needle segmentations and the expected insertion depths based on calibrated needle end-length measurements. *IDE*s were calculated for the live-2D-based needle tip positions $\vec{t}_{2D}$, and for the mean SR3D-based tip positions across users and trials, $\vec{t}_{3Dm}$. Needles were stratified by tip score, and F-tests were used to compare variance in *IDE*s before and after SR3D-based tip adjustments. The F-test results were used to assess the benefit in accuracy provided by SR3D-based tip adjustments in the presence of varying degrees of SR3D image artifacts. P-values ¡.05 were considered statistically significant for all tests.

Comparison of Final SASR and SAAR Insertion Depth Errors

Based on the statistical analysis of *IDE*s before and after SR3D-based tip adjustments, a final SASR workflow was created as follows. All needles were assigned the live-2D-based tip position $\vec{t}_{2D}$. Next, needles with tip scores that demonstrated statistically significant decreases in *IDE* variance following SR3D-based tip adjustments were assigned the mean SR3D-based tip position $\vec{t}_{3Dm}$. *IDE*s were then calculated for this set of final SASR-guided segmentations. *IDE*s were also calculated for the clinical SAAR-guided segmentations, and compared to the SASR-guided segmentations using paired t-tests and F-tests.

4.3   Results

For each patient, 15-17 needles were inserted for a total of 158 needles. 155 needles were plastic FlexiGuide needles (Eckert and Ziegler Group, Berlin, DE) and three were metal interstitial needles. Eleven needles were excluded from analysis because three needles were metal, three needles extended beyond the superior edge of the final SR3D volume due to incorrect probe placement, and four needles were not localized in their

final positions using the custom live-2D segmentation tool during the procedure. One needle was excluded due to the presence of an abnormal image artifact, which is described further in the Discussion. The small number of metal needles were excluded from analysis to improve consistency of the data, although strong specular reflection may lead to improved tip appearance of metal needles than plastic needles. Table 4.1 summarizes the frequencies of tip scores assigned to the 147 needles included in the analysis. Thirteen of the 147 needles were not visible on the final SR3D image (tip score =0) precluding SR3D-based tip adjustments, so were not included in the SR3D-based tip analysis.
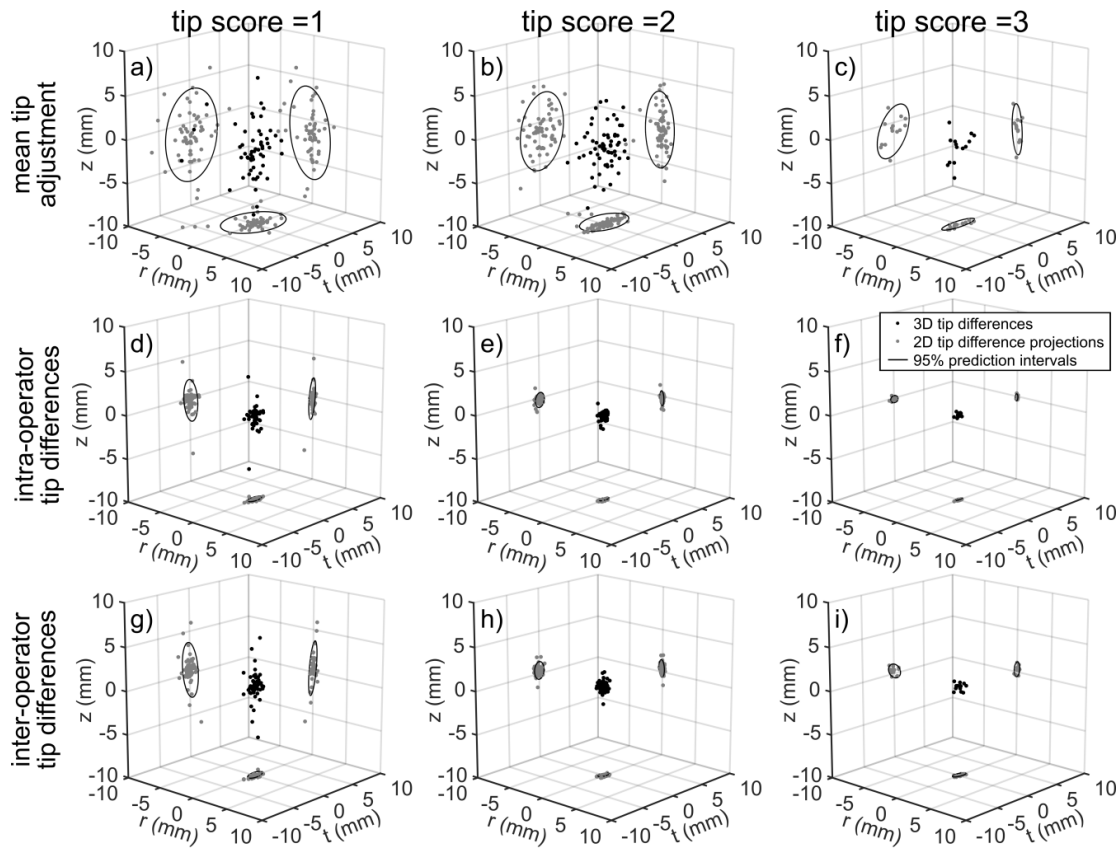
Figure 4.4: 3D scatter plots of tip position adjustments made using the SR3D images, and variability in those adjusted tip positions stratified by tip score. a-c) Plots of the mean tip adjustment made using the final SR3D image relative to the tip identified using the live-2D view. d-f) Plots of intra-operator differences in adjusted tip positions. g-i) Plots of inter-operator differences in adjusted tip position.

		tip score = 1	tip score = 2	tip score = 3
Mean	r (mm)	[-3.5, 2.6]	[-2.4, 1.9]	[-0.6, 0.9]
Tip	t (mm)	[-4.0, 4.4]	[-3.2, 3.9]	[-2.8, 2.4]
Adjustment	z (mm)	[-7.0, 3.9]	[-5.7, 3.5]	[-4.0, 2.0]
Intra-	r (mm)	[-0.5, 0.4]	[-0.3, 0.3]	[-0.2, 0.2]
operator	t (mm)	[-1.1, 1.2]	[-0.7, 0.7]	[-0.6, 0.6]
Variability	z (mm)	[-2.8, 2.2]	[-1.1, 0.7]	[-0.5, 0.3]
Inter-	r (mm)	[-0.6, 0.6]	[-0.4, 0.4]	[-0.4, 0.5]
operator	t (mm)	[-1.3, 1.3]	[-0.9, 0.7]	[-1.0, 1.0]
Variability	z (mm)	[-2.8, 3.8]	[-0.6, 1.5]	[-0.5, 1.2]

Table 4.2: 95% prediction intervals of needle tip adjustments and variability using SR3D images.

4.3.1 Difference Between Live-2D and SR3D Based Tip Positions

Figures 4.4a-c display 3D scatter plots of the average distances that each live-2D tip position was adjusted using the final SR3D image, stratified by tip score. The first three rows of Table 4.2 display the 95% prediction intervals corresponding to the scatter plots in Figure 4.4a-c. The largest tip adjustments tended to be in the direction of needle insertion (z-direction), followed by direction out-of-plane of the live-2D images (t-direction).

4.3.2 Intra- and Inter-Operator Variability in SR3D Based Tip Positions

Figure 4.4d-f display 3D scatter plots of $\vec{d}_{intra}$, and Figure 4.4g-i display 3D scatter plots of $\vec{d}_{inter}$ stratified by tip score. The final 6 rows of Table 4.2 display the 95% prediction intervals corresponding to the scatter plots in Figure 4.4d-i. Similar to the mean tip adjustments, intra- and inter-operator variability tended to be largest in the z-direction, followed by the t-direction and r-direction, respectively.
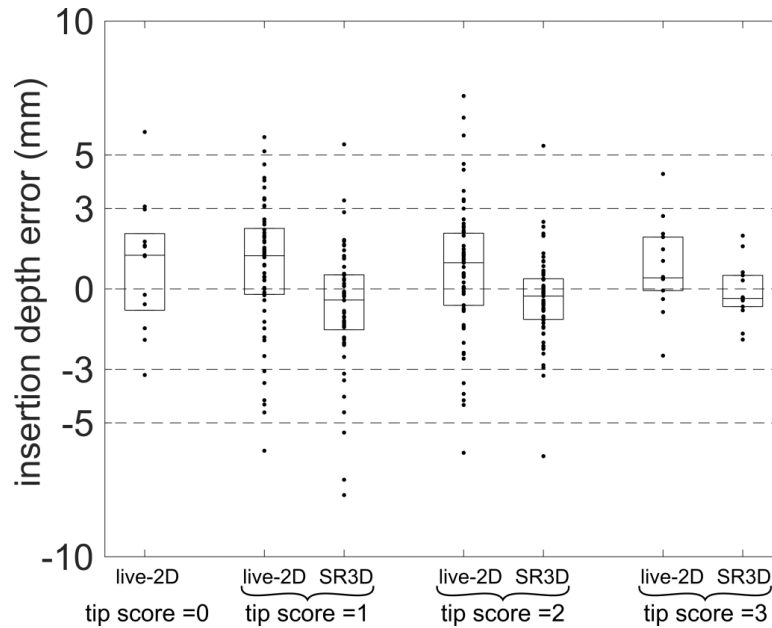
Figure 4.5: Box plots of needle insertion depth errors following intra-operative tip identification on live-2D images, and after adjustment on the final SR3D image. Needles are stratified by tip score. Needles with tip score = 0 were not visible on the final SR3D image.

4.3.3 Impact of SR3D Based Adjustments on Insertion Depth Errors

Figure 4.5 displays boxplots of *IDE*s corresponding to the live-2D tip positions and tip positions following SR3D based editing for all needles stratified by tip score, and relevant geometric parameters are summarized in Table 4.3. Results of F-tests indicated that the differences in *IDE* variance between the live-2D and SR3D-based tip-positions were not statistically significant for needles with a tip score of 1 (p = .54) and 3 (p = .13), but were statistically significant for needles with a tip score of 2 (p = .0015). Based on these results, the final SASR technique was implemented as follows. Needles with tip scores of 0 or 1 were assigned their live-2D based tip positions, and needles with tip scores of 2 and 3 were assigned their mean SR3D-based tip positions. Needles with tip scores of 3 were assigned the mean SR3D-based tip positions despite the failure to find a statistically significant difference (p < .05) between the live-2D and SR3D-based

*IDE*s, which was attributed to the relatively small number of needles in this group (n = 14).
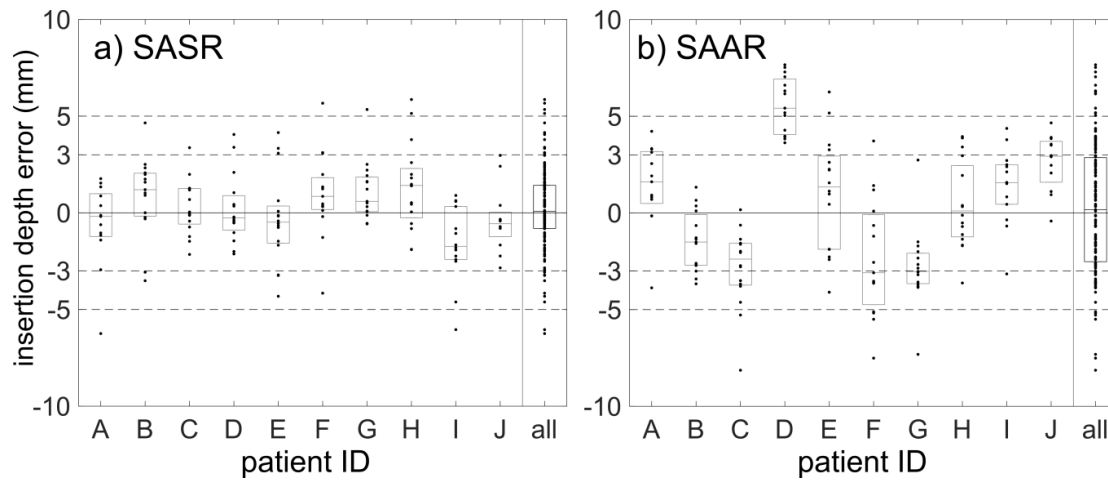
Figure 4.6: Boxplots of insertion depth errors determined using the SASR technique and SAAR technique for each patient individually, and all patients combined. In all plots center lines indicate median values, and boxes represent inter-quartile ranges.

4.3.4   Comparison of Final SASR and SAAR Insertion Depth Errors

Figure 4.6 displays boxplots of *IDE*s determined using the SASR and SAAR segmentation techniques for each patient individually, and for all patients combined. The SASR and SAAR techniques resulted in *IDE*s with mean±standard deviation of 0.2±2.1 mm and 0.2±3.3 mm respectively. Results of the F-tests and paired t-tests indicated statistically significant differences between techniques in terms of variance (p <.001) but not in terms of mean value (p =.99). The SASR technique identified needle tips with *IDE*s within ±3 mm and ±5 mm for 84% and 96% of needles respectively, and provided an *IDE* range of [-6.2 mm, 5.9 mm]. The SAAR technique provided *IDE*s within ±3 mm and ±5 mm for 57% and 87% of needles respectively, and an *IDE* range of [-8.1 mm, 7.7 mm].

	tip score =1		tip score =2		tip score =3	
	live-2D	SR3D	live-2D	SR3D	live-2D	SR3D
Mean±SD (mm)	0.8±2.5	-0.7±2.3	0.7±2.5	-0.4±1.6	0.8±1.7	-0.1±1.1
Range (mm)	[-6.0 5.7]	[-7.7 5.4]	[-6.1 7.2]	[-6.2 5.3]	[-2.5 4.3]	[-1.9 2.0]
%(#) Needles with $IDE \leq 3$ mm	70 (40)	84 (48)	78 (49)	95 (60)	93 (13)	100 (14)
%(#) Needles with $IDE \leq 5$ mm	95 (54)	93 (53)	94 (59)	97 (61)	100 (14)	100 (14)

Table 4.3: Insertion depth errors (IDEs) of needles identified on live-2D and SR3D images

4.4 Discussion

We have presented a TRUS-based SASR technique for HDR-BT needle segmentation combining intra-operative live-2D sagittal images and post-insertion SR3D images, and demonstrated improvements in tip localization accuracy compared to the conventional SAAR technique. The range of IDEs corresponding to the SASR technique observed in this study of [-6.2 mm, 5.9 mm] is less than half of the range reported previously of [-15.6 mm, 13.6 mm] when using static SR3D images alone for needle segmentation [23], and did not require the exclusion of any needles due to image artifacts on the final SR3D image, despite the presence of these artifacts obstructing the view of 8.8% of needles analyzed. These SASR segmentation characteristics were enabled by incorporating the live-2D segmentation step in the procedure, providing the tip location for needles with SR3D-based tip scores of 0 and 1, representing 47.6% of needles. The tip scores used for stratification were assigned to provide a subjective characterization of needle appearances for the purposes of this study, recognizing that needle appearances on SR3D images vary, which we expected to influence tip localization accuracy. The scores from two trials from two users were combined to create the set of tip scores for this study, which would not be practical during an intra-operative SASR-guided HDR-BT procedure; however, the observed frequency, variability, and IDE characteristics associated with each tip score are intended to provide information to aid clinical deci-

sion making when relying upon a combination of live-2D and SR3D images to select needle tip positions in the presence of image artifacts. The stratification of needles based on appearance by a single user should not add additional time to brachytherapy workflows that currently incorporate a manual verification of needle appearances on the final 3D TRUS image as a quality assurance step. Needle tips that appear clearly within a 3 mm circular cursor may be updated during this existing quality assurance procedure.

The decision to use the live-2D based tip locations for the 38.8% of needles with a tip score of 1 was made in this study for multiple reasons. First, the SR3D-based tip adjustments performed for this group of needles did not have a statistically significant impact on the measured *IDE* variance. Second, we found that the 95% prediction intervals corresponding to inter-operator variability of SR3D-based tip positions for needles with a tip score of 1 were [-3.8 mm, 2.8 mm] in the *z*-direction, exceeding our accuracy target of ±3 mm as recommended by Tiong et al. [11]. Third, the SR3D-based tip adjustments for needles with a tip score of 1 increased the measured overall *IDE* range relative to the live-2D results, from [-6.0 mm, 5.7 mm] to [-7.7 mm, 5.4 mm]. It should be noted that SR3D-based tip adjustments of needles with a tip score of 1 increased the number of needles with *IDE*s within ±3 mm from 70.2% to 84.2%, indicating a benefit in accuracy when using SR3D-based tip positions for the majority of needles, despite increased errors for some needles. It may be pragmatic to adopt a workflow where needle insertion depths with SR3D-based uncertainty >3 mm are not adjusted; however, if some of these needles are chosen to be adjusted, our results suggest that it is possible, but unlikely to increase error.

A major limitation of this study was the use of 5 mm sampling intervals for AR3D image reconstruction during the SAAR-guided procedure, which was used as the clinical reference for tip localization accuracy. Updated SAAR-guided workflows based on commercially available steppers and acquisition software enable the acquisition of

AR3D images with 1 mm sampling intervals, and enable tracking of superior/inferior probe motion using encoders, similar to the custom device used for the SASR procedure in this study. These features may enable SAAR-guided tip localization with decreased error compared to the results presented in this study. However, even with 1 mm sampling intervals, AR3D spatial resolution in the needle insertion direction is inherently limited by the elevational resolution of the axial transducer, which has been measured to be 1.5-4.0 mm depending on distance from the probe [25]. On the other hand, the superior/inferior spatial resolution of the SR3D image is limited by the in-plane spatial resolution of the sagittal transducer [21], specified as 0.9 mm by the manufacturer [10]. More importantly, the SASR approach does not require moving the probe in the superior/inferior direction, limiting the potential for organ motion between live-2D tip localization and final image acquisition.

As indicated in Figure 4.2, the superior/inferior spatial resolution of the SR3D image is higher than the AR3D image. Conversely, in the axial plane, the spatial resolution tangential to the TRUS probe is lower in the SR3D image than the AR3D image. In the SR3D image, the spatial resolution in this direction is limited by the elevational resolution of the sagittal transducer, estimated to be 1.2 mm at the focal zone (9 MHz central frequency, 40 mm focal length, 5.5 mm aperture), but wider at locations nearer and more distant from the probe. In the AR3D image, the spatial resolution in this direction is limited by the lateral resolution of the axial transducer, specified by the manufacturer as 1.5 mm, which will be more uniform with distance from the probe than the elevational resolution due to dynamic receive focusing in the in-plane direction. The decrease in axial spatial resolution outside of the focal zone associated with SR3D compared to AR3D imaging may be a limitation for certain brachytherapy workflows, such as those incorporating end-length measurements for insertion depth calculation and relying upon TRUS only to localize the needle position in the axial plane. The impact due to the difference in axial resolution outside of the focal zone between SR3D and

AR3D in such workflows needs to be quantified with further investigations.

As mentioned, 11 needles were excluded from analysis including four needles that were not segmented intra-operatively using our custom software due to technical issues, and one needle that was excluded due to the presence of an abnormal SR3D image artifact. The technical issues leading to the exclusion of four needles were related to the user interface of our custom software, and have since been resolved. The image artifact leading to the exclusion of one needle was a reflection artifact from a posterior needle in the vicinity of the true needle. This reflection artifact was selected as the true needle by one user, who noted at the time of segmentation that he was uncertain which image feature was the true needle. During an intra-operative SASR-guided workflow, live-2D tip identification and SR3D imaging could be repeated to efficiently distinguish between the artifact and needle, so the needle in question was excluded from our post-operative analysis.

While this study showed a benefit in accuracy of the SASR technique over the SAAR technique, commercially available imaging software currently enables alternate needle tip localization workflows that were not evaluated in this study. Specifically, Oncentra Brachy (Elekta, Stockholm, SE) enables the incorporation of calibrated needle end-length measurements into the intra-operative estimation of needle tip positions. This method effectively replaces the live-2D based needle tip localization technique with the gold standard insertion depth calculation technique employed in this validation study. The agreement between end-length measurements and image-based tip positions for needles with tip score = 3 within 2 mm as found in the present study suggests that the combination of end-length measurements with SR3D image acquisition may represent an optimal intra-operative needle tip and trajectory localization technique.

The dosimetric impact of the *IDE*s observed in this study was not determined; however, previous studies have indicated that needle segmentation using a single static SR3D image resulted in uncertainty in prostate V100% within 4% for all patients, and

within 3% for 11 out of 12 patients in the study [23]. Based on the geometric results of this study, we expect dosimetric uncertainty attributed to SASR-guided needle segmentation to be smaller, but a more representative dosimetric simulation would incorporate prostate and organ segmentation uncertainty. Future work will involve assessment of prostate and organ segmentation uncertainty using SR3D image-guidance, and the impact of all measured uncertainties on final HDR-BT treatment plan dosimetry.

4.5 Conclusions

The SASR technique provided decreased *IDE* variance than the conventional SAAR technique, indicating increased needle tip localization precision. The SASR technique could be performed in the same amount of time as the SAAR technique, adding negligible time for SR3D image acquisition and eliminating the need for axial-to-sagittal alignment. The SASR technique also mitigated the effects of shadow artifacts previously observed when using a single SR3D image for needle segmentation [23], demonstrated by the fact that every needle could be identified and segmented with *IDE*s within [-6.2 mm, 5.9 mm]. The SASR technique provides improved HDR-BT needle segmentation accuracy over the SAAR technique by: 1) eliminating the need to move the probe in the superior/inferior direction, 2) transferring needle segmentations from live-2D images to the SR3D image to mitigate the impact of shadow artifacts without the potentially error-prone registration step required by SAAR, and 3) providing higher spatial resolution than the AR3D image for segmentation editing and quality assurance. In our center, SR3D images are routinely acquired to aid in needle visualization, but are used in combination with the commercially available SAAR-guidance tools for treatment planning. Based on the results of this study, our center is currently working to commission our SASR-guidance system for routine clinical use within our HDR-BT procedure.

References

1. Hoskin, P. J. *et al.* GEC/ESTRO recommendations on high dose rate afterloading brachytherapy for localised prostate cancer: An update. *Radiotherapy and Oncology* **107,** 325–332 (2013).

2. Helou, J. *et al.* High dose-rate brachytherapy boost for intermediate risk prostate cancer: Long-term outcomes of two different treatment schedules and early biochemical predictors of success. *Radiotherapy and Oncology* **115,** 84–89 (2015).

3. Morton, G. C. High-dose-rate brachytherapy boost for prostate cancer: rationale and technique. *Journal of Contemporary Brachytherapy* **6,** 323–330 (2014).

4. Yamada, Y. *et al.* American Brachytherapy Society consensus guidelines for high-dose-rate prostate brachytherapy. *Brachytherapy* **11,** 20–32 (2012).

5. Hauswald, H. *et al.* High-dose-rate monotherapy for localized prostate cancer: 10-year results. *International Journal of Radiation Oncology Biology Physics* **94,** 667–674 (2016).

6. Yoshioka, Y. *et al.* High-dose-rate brachytherapy as monotherapy for intermediate- and high-risk prostate cancer: Clinical results for a median 8-year follow-up. *International Journal of Radiation Oncology Biology Physics* **94,** 675–682 (2016).

7. Jawad, M. S. *et al.* Outcomes associated with 3 treatment schedules of high-dose-rate brachytherapy monotherapy for favorable-risk prostate cancer. *International Journal of Radiation Oncology Biology Physics* **94,** 657–666 (2016).

8. Georg, D. *et al.* Dosimetric considerations to determine the optimal technique for localized prostate cancer among external photon, proton, or carbon-ion therapy and high-dose-rate or low-dose-rate brachytherapy. *International Journal of Radiation Oncology Biology Physics* **88,** 715–722 (2014).

9. Kirisits, C. *et al.* Review of clinical brachytherapy uncertainties: Analysis guidelines of GEC-ESTRO and the AAPM. *Radiotherapy and Oncology* **110,** 199–212 (2014).

10. Siebert, F.-A. A., Hirt, M., Niehoff, P. & Kovács, G. Imaging of implant needles for real-time HDR-brachytherapy prostate treatment using biplane ultrasound transducers. *Medical Physics* **36,** 3406–3412 (2009).

11. Tiong, A. *et al.* A small tolerance for catheter displacement in high-dose rate prostate brachytherapy is necessary and feasible. *International Journal of Radiation Oncology Biology Physics* **76,** 1066–1072 (2010).

12. Mason, J., Al-Qaisieh, B., Bownes, P., Thwaites, D. & Henry, A. Dosimetry modeling for focal high-dose-rate prostate brachytherapy. *Brachytherapy* **13,** 611–617 (2014).

13. Kolotas, C., Baltas, D. & Zamboglou, N. CT-based interstitial HDR brachytherapy. *Strahlentherapie und Onkologie* **175,** 419–427 (1999).

14. Murgic, J. *et al.* Lessons learned using an MRI-only workflow during high-dose-rate brachytherapy for prostate cancer. *Brachytherapy* **15,** 147–155 (2016).

15. Buus, S. *et al.* Learning curve of MRI-based planning for high-dose-rate brachytherapy for prostate cancer. *Brachytherapy* **15,** 426–434 (2016).

16. Batchelar, D. *et al.* Validation study of ultrasound-based high-dose-rate prostate brachytherapy planning compared with CT-based planning. *Brachytherapy* **13,** 75–79 (2014).

17. Morton, G. C. Prostate high-dose-rate brachytherapy: Transrectal ultrasound based planning, a technical note. *Practical Radiation Oncology* **5,** 238–240 (2015).

18. Holly, R. *et al.* Use of cone-beam imaging to correct for catheter displacement in high dose-rate prostate brachytherapy. *Brachytherapy* **10,** 299–305 (2011).

19. Cepek, J., Chronik, B., Lindner, U., Trachtenberg, J. & Fenster, A. Development of an MRI-compatible device for prostate focal therapy. *Medical Image Computing and Computer-Assisted Intervention* **15,** 455–62 (2012).

20. Batchelar, D. L. *et al.* Intraoperative ultrasound-based planning can effectively replace postoperative CT-based planning for high-dose-rate brachytherapy for prostate cancer. *Brachytherapy* **15,** 399–405 (2016).

21. Tong, S., Downey, D. B., Cardinal, H. N. & Fenster, A. A three-dimensional ultrasound prostate imaging system. *Ultrasound in Medicine and Biology* **22,** 735–746 (1996).

22. Bax, J. *et al.* A compact mechatronic system for 3D ultrasound guided prostate interventions. *Medical Physics* **38,** 1055–1069 (2011).

23. Hrinivich, W. T. *et al.* Three-dimensional transrectal ultrasound guided high-dose-rate prostate brachytherapy: A comparison of needle segmentation accuracy with two-dimensional image guidance. *Brachytherapy* **15,** 231–239 (2016).

24. Zheng, D. & Todor, D. A. A novel method for accurate needle-tip identification in trans-rectal ultrasound-based high-dose-rate prostate brachytherapy. *Brachytherapy* **10,** 466–473 (2011).

25. Peikari, M. *et al.* Characterization of ultrasound elevation beamwidth artifacts for prostate brachytherapy needle insertion. *Medical Physics* **39,** 246–256 (2012).

Chapter 5

Spatial *versus* temporal resolution of dynamic contrast enhanced MRI for prostate cancer localization: Comparing images from two pulse sequences with histology

Tumour-targeted HDR-BT efficacy depends on the ability to localize prostate tumours, and mpMRI incorporating DCE-MRI is currently recommended for this purpose. Consensus guidelines recommend DCE-MRI acquisition times of ≤ 7 s/image [1], but increased spatial resolution achievable at longer acquisition times may improve cancer localization performance. The purpose of Chapter 5 is to compare prostate cancer localization performance of DCE-MRI parameters derived from two pulse sequences demonstrating the inherent trade-off in MRI spatial and temporal resolution.

5.1   Introduction

Dynamic contrast enhanced (DCE)-MRI is a recommended component of multi-parametric MR imaging (mpMRI) protocols including T2-weighted (T2w) and diffusion-weighted (DW) imaging for the detection and localization of prostate cancer [1, 2]. Studies have demonstrated that incorporating DCE-MRI for prostate cancer localization increases the area under the receiver operating characteristic curve (AUC) from 0.92 to 0.94 [3], and reduces the contour expansion necessary to encompass 95% of high-grade cancer

from 9 mm to 6 mm when compared to mpMRI incorporating T2w and DW imaging alone [4]. Pharmacokinetic models can be applied to DCE-MRI to calculate parameters such as the transfer constant K^{trans}, corresponding to the rate of contrast agent transfer from the vascular space to the extracellular extra-vascular (EES) space [5]. K^{trans} demonstrates statistically significantly higher values in cancer relative to normal peripheral zone tissue [6] and can be used to classify $\leq$Gleason 3+4 and $\geq$Gleason 4+3 cancer with AUC of 0.69 [7]. The rate constant k_{ep}, corresponding to K^{trans} divided by the EES fractional volume, is correlated with bio-markers of prostate cancer on histology including mean vessel density [8, 9]. Model-free parameters such as washout gradient (WG), corresponding to the slope of a straight line fit to the late phase of the signal enhancement curve, demonstrated AUC of 0.88 for the distinction of $\leq$Gleason 3+3 from $\geq$Gleason 3+4 cancer [10].

While DCE-MRI parameter maps demonstrate utility for prostate cancer localization and staging, parameter values are sensitive to the time required to acquire each individual T1-weighted (T1w) image in the DCE-MRI time series [11, 12]. Recent prostate cancer imaging guidelines from the American College of Radiology recommend optimal DCE-MRI acquisition times of $\leq$7 s/image, and at most 15 s/image [1]. Pharmacokinetic modeling for K^{trans} and k_{ep} calculation requires an estimate of the arterial contrast agent concentration *versus* time, or arterial input function (AIF) [5]. Patient-specific AIF measurements require high temporal sampling and are susceptible to inflow artifacts in magnitude T1w images [13]. Population-averaged AIFs have been proposed [14], enabling pharmacokinetic modeling at acquisition times >5 s/image [15], but eliminate patient-specific contrast agent delivery normalization. Alternatively, reference region models (RRM) have been proposed enabling the estimation of patient-specific AIFs by measuring the contrast agent concentration *versus* time of a nearby reference tissue with known pharmacokinetic parameters [16, 17]. Since the AIF is not measured directly, these RRM techniques show promise for patient-specific

AIF estimation with acquisition times up to 32.8 s/image [18–20]. While these techniques are promising for overcoming limitations in AIF sampling, evidence suggests that temporal sampling in the tissue-of-interest is also subject to constraints. Simulations demonstrate that DCE-MRI acquisition times >10 s/image leads to aliasing of high temporal frequency components, manifesting as noise in resultant K^{trans} and k_{ep} values [11]. Alternatively, simulations demonstrated that decreasing image acquisition time from 14.9 s/image to 1.4 s/image does not lead to statistically significant improvements in prostate cancer localization performance using K^{trans} [7], suggesting that 10 s/image may represent an optimum trade-off between temporal resolution and image quality.

Simulation studies suggesting optimal DCE-MRI acquisition times of 10-15 s/image do not fully account for benefits of increased spatial resolution achievable with longer acquisition times. Rosenkrantz et al. provide a summary of pulse sequences used in 17 studies investigating DCE-MRI of prostate cancer, including acquisition times and voxel dimensions [21]. The smallest in-plane voxel dimensions among studies with acquisition times <15 s/image and ≥15 s/image were 0.8×0.9 mm^2 and 0.5×0.5 mm^2 respectively [22, 23]. Recent developments in DCE-MRI acquisition techniques using compressed sensing, parallel imaging [21, 24], and 32-coil receiver arrays [25] have demonstrated acquisition times of 2.3-6.6 s/image with higher signal-to-noise ratios (SNR) than previously achievable, but have not demonstrated the in-plane voxel dimensions achievable with acquisition times ≥15 s/image [23].

DCE-MRI detects changes in vascular properties associated with cancer presence [8], and increasing spatial resolution may improve the ability to detect these changes. Vascular properties may be heterogeneous within prostate tumours [8], and partial volume effects may decrease the ability to detect small regions of high vascular permeability that contribute contrast between cancer and normal tissue. Spatial resolution higher than 0.5 mm may improve the detection of high-grade tumour sub-volumes for

improved detection of clinically-significant disease [26] or targeting in mpMRI-guided biopsy systems [27]. To detect vascular heterogeneity, Degani et al. proposed the three-time-point (3TP) method, involving the analysis of only three images acquired minutes apart [28]. The 3TP method has shown utility in the detection and characterization of cancer in the prostate and breast using pulse sequences with acquisition times of 90 s/image [29] and 123 s/image [30, 31] respectively. Additionally, *WG* has demonstrated stable values at acquisition times up to 30 s/image [15]. Analysis methods suitable for acquisition times $\geq$30 s/image may lead to improved prostate cancer localization accuracy through improved spatial resolution, potentially providing higher accuracy than currently possible with recommended acquisition times $\leq$15 s/image.

The purpose of this study is to investigate the trade-off in spatial and temporal resolution of DCE-MRI for prostate cancer localization experimentally by comparing pharmacokinetic, *WG*, and 3TP parameter maps derived from DCE-MRI acquired using two pulse sequences with deformably registered whole-mount histology. The two pulse sequences demonstrate this trade-off with mean acquisition times of 6.4 s/image and 92.5 s/image and corresponding voxel dimensions of $0.55 \times 0.55 \times 3.00$ mm^3 and $0.27 \times 0.27 \times 2.80$ mm^3.

5.2   Materials and Methods

Sixteen prostate cancer patients scheduled to undergo radical prostatectomy underwent MR imaging at 3T with a Discovery MR750 imaging unit (GE Healthcare, Waukesha, WI) using a Prostate eCoil 8-channel endorectal receive coil (Medrad, Warrendale, PA) and 32-channel phased-array abdominal coil (Neocoil, Pewaukee, WI) using one of two sets of pulse sequence parameters. Patients were divided into cohorts A and B based on the pulse sequence parameters used, with 5 patients in cohort A and 11 patients in cohort B. All patients included in analysis had components of Gleason 3+3 and

≥Gleason 3+4 cancer identified on histology. We are currently analyzing data from an additional 8 patients in cohort A (for a total of 13), but report the results from the first 5 patients in this manuscript. The imaging study was approved by the Western University Health Sciences research ethics board, and written consent was obtained for each patient upon enrollment.

5.2.1 Image Acquisition

DCE-MRI datasets were acquired using 3D T1w fast-spoiled gradient echo (FSPGR) pulse sequences with mean acquisition times and voxel dimensions of 6.4 s/image and $0.55 \times 0.55 \times 3.00$ mm^3 for cohort A, and 92.5 s/image and $0.27 \times 0.27 \times 2.80$ mm^3 for cohort B. Additional pulse sequence parameters are summarized in Table 5.1. For all patients 20 mL of gadolinium based contrast agent (Magnevist, Bayer Healthcare Pharmaceuticals, West Haven CT) was injected as a bolus at 4 ml/s using a power-injector for all patients followed by a 20 ml saline flush. At least one baseline image was acquired prior to contrast agent injection for each patient. T2-weighted (T2w) images were acquired for each patient in the same imaging session for prostate segmentation and registration with whole-mount histology. All T2w images were acquired using a 3D spin echo pulse sequence with 90° flip angle, 155.5 ms echo time (TE), 2000 ms repetition time (TR), $0.27 \times 0.27 \times 1.40$ mm^3 voxel dimensions, 14.0×14.0 mm^2 in-plane field-of-view (FOV), and 80-148 slices with 0.70 mm spacing.

5.2.2 Image Analysis

Image analysis was performed using 3D Slicer 4.4 [32] and custom software written in C++ using the Insight Segmentation and Registration Toolkit (ITK) 4.0 (Kitware Inc. Clifton Park, NY). To account for motion between the T2w and DCE-MRI acquisitions, baseline T1w images were rigidly registered to the T2w images manually. To account for motion occurring during DCE-MRI acquisition, all T1w images in each

	cohort A	cohort B
median (range) time/image (s)	6.4 (6.1-7.0)	92.5 (90.2-93.3)
median (range) # time points	8 (7-11)	40 (40-50)
median (range) TR (ms)	3.31 (3.09-3.48)	5.73 (5.58 - 5.78)
median (range) TE (ms)	1.59 (1.54-1.64)	2.10 (2.10-2.12)
flip angle ($°$)	12	15
voxel dimensions (mm^3)	$0.55 \times 0.55 \times 3.00$	$0.27 \times 0.27 \times 2.80$
in-plane field of view (mm^2)	9.8×14.0	14.0×14.0
slice spacing	3.00	1.40
median (range) # slices	26 (24-28)	76 (76-76)

Table 5.1: MRI pulse sequence parameters for 2 cohorts.

dataset were rigidly registered to the baseline T1w image automatically using Mattes mutual information (MMI) image similarity metric [33] optimized using the limited-memory Broyden-Fletcher-Goldfarb-Shanno (L-BFGS) algorithm [34]. Each prostate was manually segmented using the T2w image.

Signal-to-Gadolinium Concentration Conversion

Voxel-wise gadolinium (Gd) concentrations were estimated using the increases in T1w signal intensity over time relative to the baseline image. First, T1 relaxation rates were estimated using the non-linear FSPGR signal equation [35], assuming a baseline T1 value of 1597 ms in the prostate [36]. Second, Gd concentrations were calculated assuming a linear relationship between T1 relaxation rate and concentration, assuming Gd relaxivity of 3.87×10^{-3} mmol^{-1} ms^{-1} [37].

Pharmacokinetic Modeling

The Tofts two-compartment pharmacokinetic model was applied to the Gd concentration *versus* time curves to determine maps of K^{trans} and k_{ep} [5]. These parameter maps were calculated for each patient twice, using two arterial input function (AIF) models. First, the population-averaged AIF measured by Parker et al. was applied to determine K^{trans}-AIF and k_{ep}-AIF [14]. Second, a patient-specific AIF derived from nearby

reference tissue using the method proposed by Kovar et al. was applied to determine K^{trans}-RRM and k_{ep}-RRM [16]. The RRM method involves the measurement of Gd concentration *versus* time for a nearby tissue with characterized pharmacokinetic parameters. By assuming constant pharmacokinetic parameters for the reference tissue, a patient-specific AIF can be estimated and applied to the tissue of interest. In this study, obturator internus muscle (OIM) located lateral to the prostate within the DCE-MRI field of view were segmented for each patient and used as reference tissue. Gd concentrations in the OIM were calculated using the same method as the prostate, assuming a baseline T1 value of 898 ms [36]. The RRM was applied assuming population-averaged OIM K^{trans} and k_{ep} values of 0.022 min^{-1} and 0.25 min^{-1} [13]. Non-linear versions of the population-averaged AIF [5] and RRM [38] were fit to the Gd concentration *versus* time curves of each voxel by minimizing the sum of the squared residuals using the bounded L-BFGS optimization algorithm [34], constraining K^{trans} and k_{ep} within 0 and 5 min^{-1}.

Washout-Gradient

Washout-gradients (*WG*) were calculated as the slope of a straight line fit to the late phase of the Gd *versus* time curves [10]. The late phase was set as 2 min post-contrast agent onset to the end of the acquisition for all patients.

Three-Time-Point Method

The three-time-point (3TP) method for low temporal resolution DCE-MRI was applied as proposed by Degani et al. [28]. Briefly, the 3TP method involves the analysis of three images, assigning intensities based on the rate of contrast wash-in, and colors based on the rate of contrast agent wash-out. For all patients in this study, the three imaging time points were selected as the baseline pre-contrast image, and two images 1.5 min and 4.5 min post-contrast onset. Comparison of the first and second image was used to

assign intensity values from 0-255, and comparison of the second and third image was used to assign a color, where a change >5% was colored blue, a change within 5% and -15% was assigned green, and a change <-15% was assigned red. Details regarding the 3TP calibration used in this study are provided in Appendix C. Statistical analysis of the 3TP voxel values required conversion from vector RGB voxel values to scalar voxel values. This was performed by scaling intensity values from 0-1 for blue voxels, 1-2 for green voxels, and 2-3 for red voxels. We refer to the resultant dimensionless value between 0 and 3 for each voxel as the 3TP score.

5.2.3 Histological Analysis

Slide Preparation

All patients in this study underwent radical prostatectomy within 6 weeks of MR imaging. Post-prostatectomy specimens were marked with strand-shaped fiducials and imaged *ex vivo* with MRI to support 3D reconstruction and then processed for whole-mount histology. Histology sections (3-5 per patient) were stained with hematoxylin and eosin, and digitized on a ScanScope brightfield scanner (Aperio Technologies, Vista, CA). Contouring and grading of cancer on histology images was performed by an MD and approved by a genitourinary pathologist. Contoured pathologies included in the analysis were prostatic intra-epithelial neoplasia (PIN), Gleason 3+3 cancer, and ≥Gleason 3+4 cancer, which included any component of Gleason 4 or 5 cancer.

Slide Registration

Histology was reconstructed into the 3D *ex vivo* image space using a semi-automated reconstruction algorithm that minimized the fiducial registration error between fiducials on histology and the *ex vivo* images [39]. The reconstructed histology was registered to the *in vivo* T2w images using an interactively defined 3D thin-plate-spline transfor-

mation from *ex vivo* image coordinates to *in vivo* image coordinates. For comparison with *in vivo* images, transformed histology was projected onto the best-fit oblique plane through the *in vivo* images.

Transferring Pathologist Contours to DCE-MRI Parameter Maps

Pathologist contours were transferred from the T2w image space to the baseline T1w image space using the manual rigid registration between the T1w and T2w images. To label T1w voxels for analysis, slide contours were re-sampled using the following scheme. For each voxel intersected by a slide, the fractional cross sectional area of each T1w voxel contoured as normal tissue, PIN, Gleason 3+3, and ≥Gleason 3+4 was determined. Voxels containing any fraction of diseased tissue (PIN, Gleason 3+3, or ≥Gleason 3+4) were labelled as the diseased tissue type comprising the largest cross sectional area. Voxels were labeled as normal tissue if they were intersected by a slide, contained zero diseased tissue component, were within the T2w prostate contour, and were at least 2 mm away from any diseased tissue voxels.

cohort (#patients)	tissue type	median(range) # voxels/patient	median(range) % voxels/patient	total # voxels	total area (mm^2)
A (5)	normal	4.5 (1.5-6.6)×10^3	54.6 (19.4-87.6)	2.1×10^4	6.2×10^3
	PIN	20.0 (5.2-30.3)×10^2	24.3 (10.0-40.4)	9.1×10^3	2.7×10^3
	G3+3	2.1 (0.9-32.7)×10^2	2.1 (1.7-41.7)	4.0×10^3	1.2×10^3
	≥G3+4	16.1 (1.3-22.1)×10^1	3.3 (0.2-21.9)	3.1×10^3	9.4×10^2
B (11)	normal	28.7 (9.0-66.3)×10^3	85.4 (52.5-95.2)	3.7×10^5	2.7×10^4
	PIN	33.5 (7.6-110.6)×10^2	9.9 (2.6-31.4)	5.1×10^4	3.7×10^3
	G3+3	7.0 (2.6-49.5)×10^2	2.3 (0.5-16.3)	1.5×10^4	1.1×10^3
	≥G3+4	51.3 (5.8-20.6)×10^1	1.2 (0.2-7.0)	7.3×10^3	5.5×10^2

Table 5.2: Histology label map characteristics.

5.2.4 Experimental Methods

Parameter Mean Values in Diseased and Normal Tissue

The mean value of each parameter across voxels labeled as each tissue type was determined for each patient. Patient-specific parameter mean values were analyzed to determine whether statistically significant differences existed: 1) between cohorts within tissue types and 2) between normal and diseased tissue types within each cohort.

A two-way mixed multivariate ANOVA was applied to the patient-specific mean values, with cohort as the between-subjects factor and tissue type as the within-subjects factor. For parameters with a significant main effect of cohort on mean values, a one-way multivariate ANOVA with cohort as the between-subjects factor was applied to each tissue type individually. For parameters with a significant main effect of tissue type, a one-way repeated-measures multivariate ANOVA with tissue type as the within-subjects factor was applied to each cohort individually, and post-hoc paired t-tests with Bonferroni corrections were used to assess pairwise differences between normal and diseased tissue types. All statistical analyses were performed using R (version 3.4, the R Foundation).

Parameter Contrast Between Diseased and Normal Tissue

Patient-specific contrasts between diseased and normal tissue for each tissue type and parameter were calculated using Eq 5.1,

$$contrast = \frac{(\mu_{dis} - \mu_{norm})}{\mu_{norm}} \tag{5.1}$$

where μ_{norm} is the mean parameter value in normal tissue, and μ_{dis} is the mean value in the diseased tissue. In the case of WG, mean values straddle zero precluding normalization of contrast by μ_{norm}, so a value of 0.5 μmol s^{-1} was uniformly subtracted from μ_{norm} and μ_{dis} to make mean WG values purely negative, enabling application of Eq.

5.1. Patient-specific mean contrasts were analyzed to determine whether statistically significant differences existed: 1) between cohorts within each diseased tissue type and 2) between parameters within each cohort.

A three-way mixed ANOVA was applied to the patient-specific mean contrasts, with cohort as a between-subjects factors, and parameter and tissue type as within-subjects factors. A two-way repeated-measures ANOVAs with parameter and tissue type as within-subjects factors was applied to the data within each cohort independently. For cohorts with a statistically significant main effect of parameter, a one-way repeated measures ANOVA with parameter as the within-subjects factor was performed for each tissue type individually, and post-hoc paired t-tests with Bonferroni correction to assess pairwise differences between parameters. Post-hoc unpaired t-tests were used to determine pairwise differences between cohorts for each parameter and tissue type.

Classification of Diseased and Normal Tissue Voxels

Receiver operating characteristic (ROC) curve analysis was used to assess the performance of each parameter in voxel-wise classification of diseased and normal tissue. Voxel values for each tissue type were combined across patients in each cohort. To normalize for differences in tissue volumes across patients, voxel values were randomly sampled with replacement so that each patient contributed 7.0×10^4 voxels from normal tissue and 1.2×10^4 voxels from each of PIN, Gleason 3+3, and $\geq$Gleason 3+4 tissue. These labeled voxel-arrays were then used as input in the ROC analysis to assess the performance of each parameter in classifying PIN *versus* normal tissue, Gleason 3+3 cancer *versus* normal tissue, and $\geq$Gleason 3+4 cancer *versus* normal tissue for each cohort. Area under the curve (AUC) was calculated for each ROC curve. All ROC analysis was performed in R using the pROC package [40].
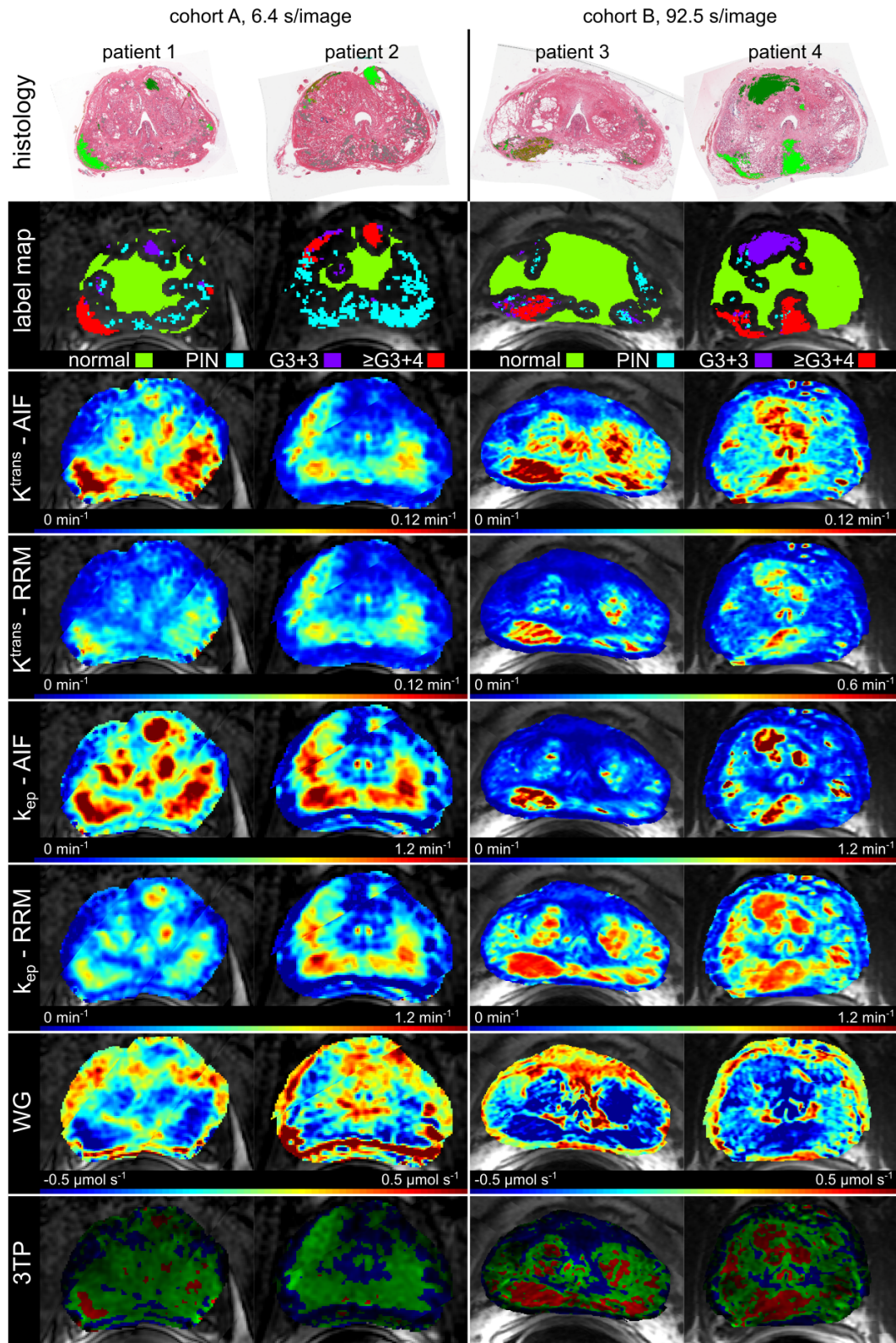
Figure 5.1: Example co-registered histology slides, label maps, and parameter maps from two patients from each cohort. Parameter maps are displayed over the baseline T1w image for the prostate plus a 2 mm expansion.
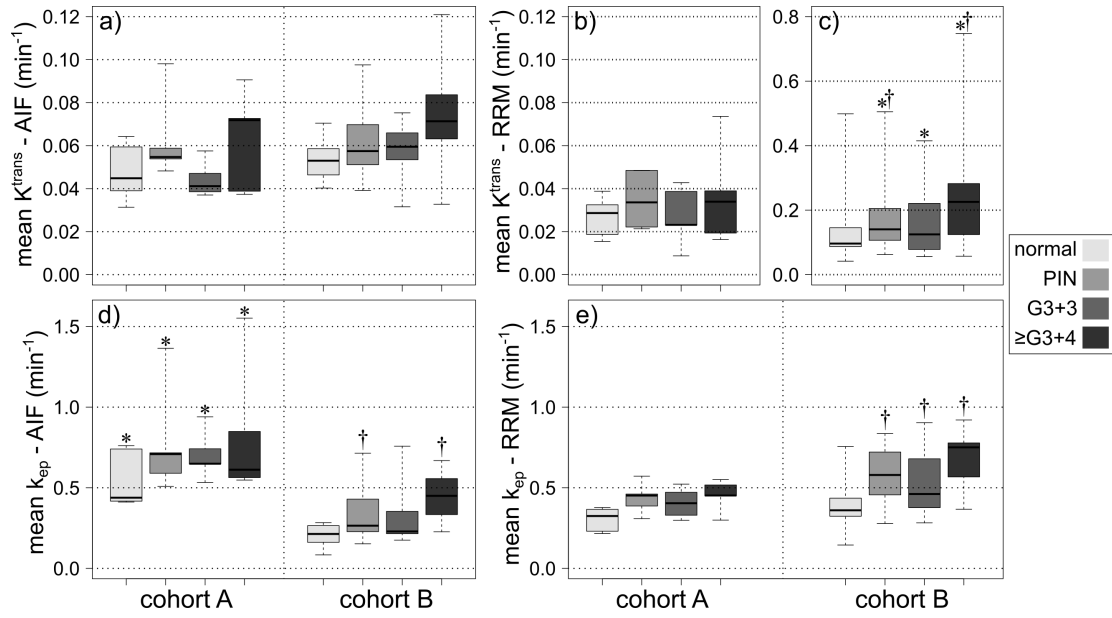
Figure 5.2: Boxplots of patient-specific mean parameter values in normal and diseased prostate tissue. Center-lines indicate median values and whiskers indicate the range across patients. Superscript symbols indicate the presence of a statistically significantly higher mean value than the same tissue in the alternate cohort (*), or normal tissue within the same cohort (†).

5.3 Results

The number of voxels and cross-sectional areas of each tissue type in the histology-derived label maps are summarized in Table 5.2. Figure 5.1 displays example co-registered histology slides, label maps, and parameter maps from two patients from each cohort.

5.3.1 Parameter Mean Values in Diseased and Normal Tissue

Boxplots of patient-specific mean parameter values for each tissue type are displayed in Figures 5.2 and 5.3. Statistically significant main effects of cohort were found for K^{trans}-RRM (p = .029), k_{ep}-AIF (p = .001), WG (p = .001), and 3TP score (p = .007). Statistically significant main effects of tissue type were found for all parameters (p <.001). Within cohort A, statistically significant effects of tissue type were found for

k_{ep}-RRM (p = .041) and 3TP score (p = .043). Within cohort B, statistically significant effects of tissue type were found for all parameters (p <.01). Statistically significant pairwise differences between cohorts for each tissue type are indicated in Figures 5.2 and 5.3 by asterisks (*). Statistically significant pairwise differences between diseased and normal tissue types within cohorts are indicated in Figures 5.2 and 5.3 by daggers (†).
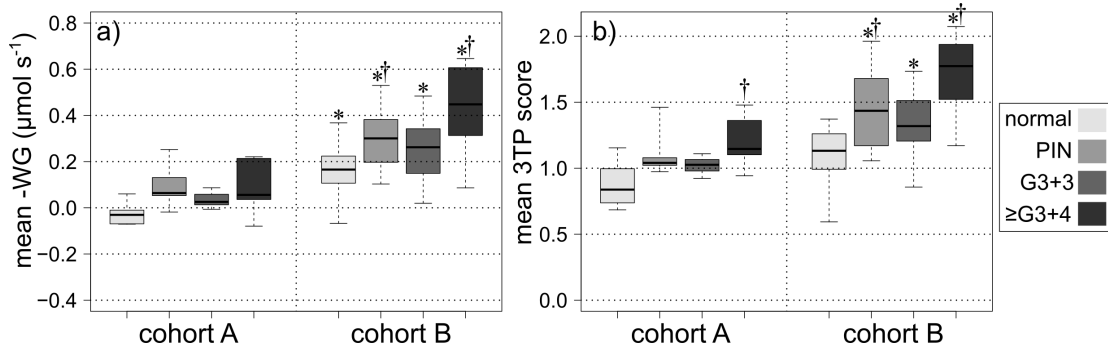
Figure 5.3: Boxplots of patient-specific mean parameter values in normal and diseased prostate tissue. Center-lines indicate median values and whiskers indicate the range across patients. Superscript symbols indicate the presence of a statistically significantly higher mean value than the same tissue in the alternate cohort (*), or normal tissue within the same cohort (†) (Plot 5.3a displays negative *WG* values to make relative values between diseased and normal tissue consistent with other parameters.)

5.3.2   Parameter Contrast Between Diseased and Normal Tissue

Boxplots of patient-specific mean contrast for each parameter and tissue type are displayed in Figure 5.4, and summarized in Table 5.3. Statistically significant main effects were found for parameter type (p <.001) and tissue type (p = .003) but not cohort (p = .30). A statistically significant interaction was found between parameter type and cohort (p = .024) and a statistically significant pairwise difference between cohorts was found for k_{ep}-AIF in ≥Gleason 3+4 cancer. Statistically significant interactions were not found between parameter type and tissue type (p = .10) or between cohort and tissue type (p = .23).

When analyzing differences between parameters within each cohort, statistically significant main effects of parameter type were found for both cohort A and B (p <.001). Within cohort A, k_{ep}-RRM provided the highest mean contrast for all tissue types; however, no statistically significant pair-wise differences were found between parameters. Within cohort B, k_{ep}-AIF provided the highest mean contrast for all tissue types. Statistically significant pairwise differences between k_{ep}-AIF and other parameters were found for K^{trans}-AIF (p = .032) in PIN, and for K^{trans}-AIF (p = .042) and WG (p = .048) in ≥Gleason 3+4 cancer.

Based on the statistically significant main effect of tissue type on contrast, and an absence of statistically significant interactions between tissue type and cohort or parameter type, paired t-tests with Bonferroni correction were performed to assess pairwise differences in contrast between tissue types across cohorts and parameters. Mean±SD contrast across cohorts and parameters for PIN, Gleason 3+3, and ≥Gleason 3+4 cancer was 0.37±0.33, 0.26±0.41, and 0.60±0.52 respectively, and pairwise differences between PIN and Gleason 3+3 (p = .003), PIN and ≥Gleason 3+4 (p <.001), and Gleason 3+3 and ≥Gleason 3+4 (p <.001) were all statistically significant.

5.3.3   Classification of Diseased and Normal Tissue Voxels

ROC curves for the classification of diseased and normal tissue voxels for each parameter and cohort are displayed in Figure 5.5 with corresponding AUC values in Table 5.4. Between tissue types, ≥Gleason 3+4 cancer was associated with the highest AUC values across cohorts and parameters, followed by PIN. Between parameters, k_{ep}-RRM and k_{ep}-AIF provided the highest AUC values for cohort A nd B respectively. Between cohorts, relative AUC values depended on tissue and parameter type. Cohort B demonstrated higher classification performance for ≥Gleason 3+4 cancer than cohort A for all parameters.
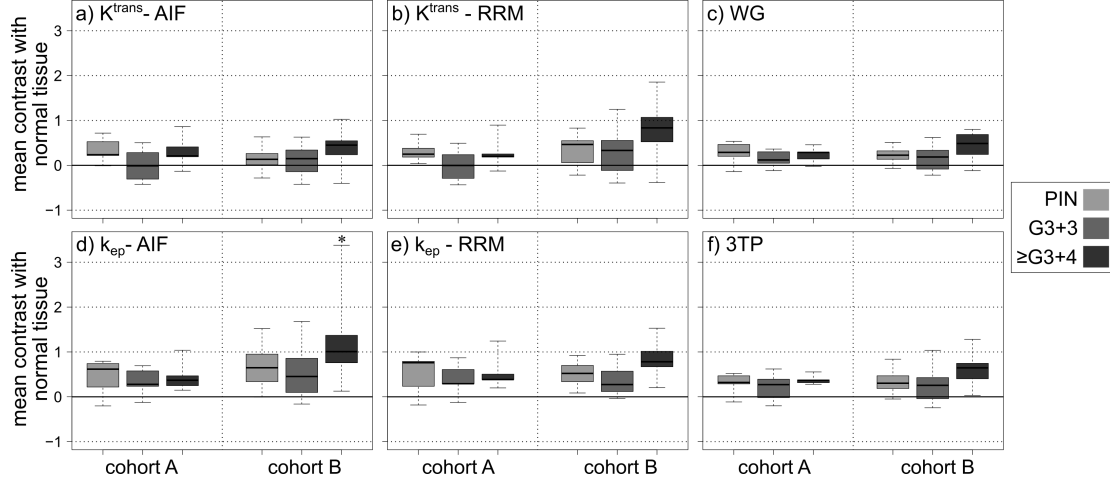
Figure 5.4: Boxplots of patient-specific mean contrast between diseased regions and normal tissue. Center-lines indicate median values and whiskers represent range across patients. The superscript asterisk (*) indicates contrast in k_{ep}-AIF between $\geq$Gleason 3+4 cancer and normal tissue was statistically significantly higher in cohort B than cohort A.

5.4   Discussion

This preliminary hypothesis generating study compared mean values, contrast between diseased and normal prostate tissue, and voxel-wise classification performance of DCE-MRI parameter maps in two cohorts of prostate cancer patients imaged using two pulse sequences. These pulse sequences represent the trade-off between spatial and temporal resolution inherent to MR imaging with acquisition time and voxel dimensions of 6.4 s/image and $0.55 \times 0.55 \times 3.00$ mm^3 for cohort A and 92.5 s/image and $0.27 \times 0.27 \times 2.80$ mm^3 for cohort B.

The comparison of patient-specific mean parameter values between cohorts demonstrated varying effects depending on the parameter. Statistically significant main effects of cohort were found for K^{trans}-RRM, k_{ep}-AIF, WG, and 3TP score. Differences in parameter values between cohorts could be attributed to multiple factors including differences in acquisition time per image, spatial resolution, SNR, total number of imaging timepoints, and pulse-sequence specific uncertainties in parameters such as flip angle.

parameter map	tissue type	cohort A	cohort B
K^{trans}-AIF	PIN	0.34 (0.29)	0.15 (0.24)
	G3+3	0.01 (0.39)	0.12 (0.33)
	≥G+4	0.31 (0.37)	0.41 (0.40)
K^{trans}-RRM	PIN	0.31 (0.25)	0.35 (0.33)
	G3+3	0.00 (0.38)	0.29 (0.48)
	≥G3+4	0.28 (0.37)	0.78 (0.58)
k_{ep}-AIF	PIN	0.43 (0.42)	0.64 (0.47)
	G3+3	0.33 (0.32)	0.57 (0.65)
	≥G3+4	0.45 (0.35)	1.21 (0.84)
k_{ep}-RRM	PIN	0.52 (0.48)	0.51 (0.28)
	G3+3	0.39 (0.38)	0.37 (0.32)
	≥G3+4	0.54 (0.41)	0.82 (0.41)
WG	PIN	0.27 (0.27)	0.23 (0.17)
	G3+3	0.14 (0.19)	0.18 (0.28)
	≥G3+4	0.23 (0.18)	0.44 (0.30)
3TP	PIN	0.30 (0.25)	0.34 (0.25)
	G3+3	0.21 (0.33)	0.27 (0.38)
	≥G3+4	0.38 (0.11)	0.61 (0.37)

Table 5.3: Mean (standard deviation) contrast between diseased and normal prostate tissue.

These factors are expanded upon as follows.

K^{trans}-RRM was found to have statistically significant differences between cohorts A and B for all tissue types, with median values higher in cohort B than cohort A. This was partially attributed to differences in Gd concentrations measured in the OIM between cohorts A and B, which lay on the lateral edges of the T1w image field of view. OIM Gd concentrations were found to be systematically higher in cohort A with mean±SD plateau values of 0.20±0.06 mMol *versus* 0.14±0.03 mMol in cohort B, potentially attributed to flip angle uncertainties [41] or biases in signal intensities due to differing SNR between pulse sequences [42]. Conversely, k_{ep}-AIF has demonstrated insensitivity to Gd concentration re-scaling [43], so differences between cohorts A and B may be attributed to differences in acquisition time per image. Model-free parameters WG and 3TP scores may have been impacted by multiple factors including Gd concentration uncertainty, acquisition times, and total number of imaging time points.

Across parameters, k_{ep}-RRM demonstrated the smallest differences between cohorts for all tissue types.
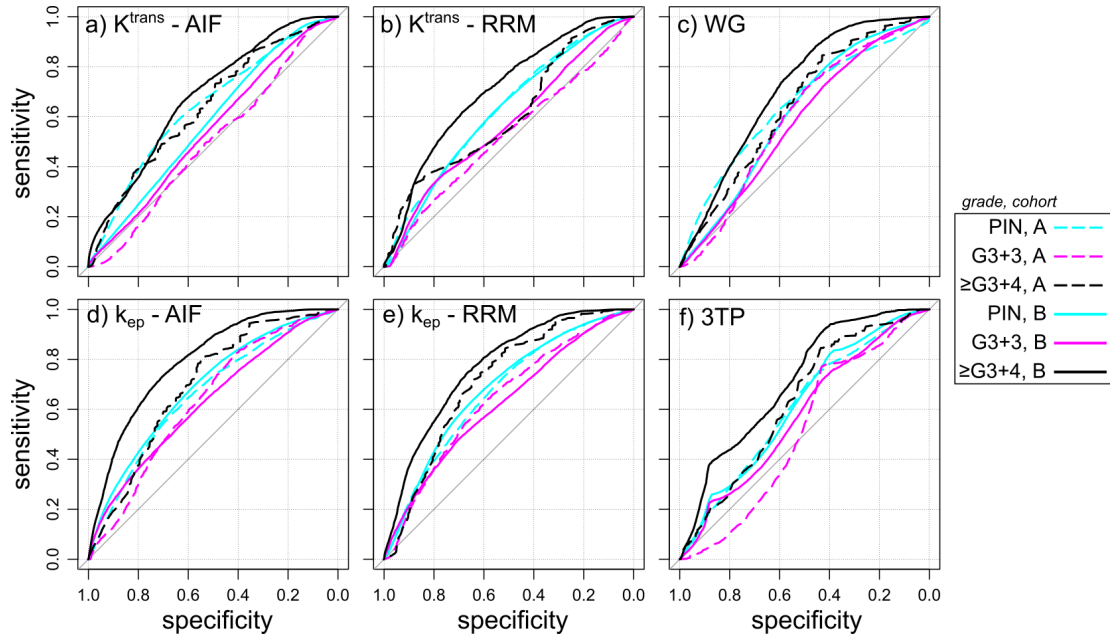
Figure 5.5: ROC curves corresponding to the classification of diseased and normal tissue voxels using parameter maps across patients in cohorts A and B.

| parameter | PIN | | Gleason 3+3 | | ≥Gleason 3+4 | |
map	cohort A	cohort B	cohort A	cohort B	cohort A	cohort B
K^{trans}-AIF	0.64	0.58	0.50	0.55	0.64	0.68
K^{trans}-RRM	0.63	0.62	0.52	0.57	0.61	0.70
k_{ep}-AIF	0.66	0.69	0.63	0.63	0.70	0.79
k_{ep}-RRM	0.67	0.68	0.64	0.62	0.71	0.77
WG	0.65	0.61	0.60	0.58	0.64	0.71
3TP	0.61	0.61	0.51	0.58	0.63	0.71

Table 5.4: AUC values for voxel-wise classification of diseased and normal tissue.

The comparison of patient specific mean parameter values between diseased and normal tissue demonstrated varying effects depending on the parameter, cohort, and tissue type. Statistically significant effects of tissue type were found in both cohorts for k_{ep}-RRM, but were only found in cohort B for the other parameters. In cohort A, statistically-significant pairwise differences in k_{ep}-RRM were only found between

$\geq$Gleason 3+4 cancer and normal tissue, whereas in cohort B pairwise differences were found between PIN, Gleason 3+3, and $\geq$Gleason 3+4 cancer. This difference in statistical significance between cohorts may be partially attributable to differing numbers of patients in each cohort; however, mean values between diseased and normal tissue tended to be larger in cohort B than cohort A. Vascular changes have been shown to increase from PIN, to low-grade cancer, to high-grade cancer [9].

The comparison of patient-specific contrasts between cohorts also demonstrated varying effects depending on the parameter and tissue type. Statistically significant pairwise differences between cohorts were only found in $\geq$Gleason 3+4 cancer for k_{ep}-AIF, with cohort B providing higher mean contrast. Across parameters, k_{ep}-RRM and k_{ep}-AIF provided the highest mean contrast for all tissue types within cohort A and B, respectively. Within both cohort A and B, there were no statistically significant pairwise differences in mean contrast between k_{ep}-AIF and k_{ep}-RRM for any tissue type, suggesting that the small differences observed within cohorts between k_{ep} calculation methods may be due to random variations. Interestingly, K^{trans} tended to provide significantly lower contrast between cancer and normal tissue than k_{ep} within both cohorts when calculated using either a population averaged AIF or RRM. K^{trans} has demonstrated high sensitivity to Gd rescaling [43], which may be a significant source of error in the analysis methods employed in this study [41]; however, our calculation of patient-specific contrast involved normalization with normal tissue to account for inter-patient variation in absolute parameter values. van Niekerk et al. demonstrated that a statistically significant correlation with microvascular parameters on whole-mount histology did not exist for K^{trans}, but did exist for k_{ep} [8]. The results of the present study also suggest that k_{ep} may be a superior bio-marker for prostate cancer compared to K^{trans}.

The comparison of voxel-wise classification performance followed similar trends to the patient-specific contrast between diseased and normal tissue. Within each parameter and tissue type, cohort B provided a higher AUC value than cohort A, with k_{ep}-AIF

providing the highest AUC values within cohort B for each tissue type. Within cohort A, k_{ep}-AIF and k_{ep}-RRM provided identical AUC values for all tissue types, which were higher than all other parameters.

The results indicating that pharmacokinetic parameters derived from DCE-MRI with acquisition times of 92.5 s/image provide superior contrast between cancer and normal tissue contradict the results of simulation studies recommending acquisition times <10 s/image [11]. It is likely that the methods employed in previous simulation studies did not fully account for the potential benefits in prostate cancer localization performance through improved spatial resolution, which can only be fully accounted for by acquiring DCE-MRI with longer acquisition times per image. The benefits in performance observed in cohort B may be attributed to decreases in partial volume effects, leading to improved detection of small high-grade cancer components or regions of high vascular permeability [30]. Improved spatial resolution, SNR, and a larger imaging field of view may also have improved the registration accuracy of the motion compensation technique employed. The median (range) of patient-specific maximum translational motion observed in cohort A and B during the DCE-MRI acquisition was 0.7 (0.5-2.4) mm and 1.0 (0.2-3.9) mm respectively, and incomplete correction of this motion may introduce artifacts in Gd concentration *versus* time curves [44] leading to decreased contrast between cancer and normal tissue. A simulation study involving spatial down-sampling of the T1w images in cohort B may provide additional evidence that spatial resolution is the reason for the improvement in cancer localization observed in cohort B in this study.

The results of this study indicated increased contrast and voxel-wise classification performance for both ≥Gleason 3+4 cancer and PIN compared to Gleason 3+3 cancer. While previous studies have indicated that DCE-MRI parameters correlate with cancer aggressiveness [7], the result indicating that DCE-MRI parameters associated with PIN are increased compared to Gleason 3+3 cancer is unexpected. This increase associated

with PIN was found to be consistent across cohorts and parameter maps. We verified that the PIN and Gleason 3+3 labels were not reversed in the software by viewing the DCE-MRI label maps overlaid the original histology contours, then importing the label map into the statistical analysis software as a parameter map to verify that the labels were preseved through all steps of the analysis. PIN is a precursor to invasive prostate adenocarcinoma [45], and has been associated with an increase in vascular growth factors compared to normal tissue, but decreased relative to adenocarcinoma [9]. Increased contrast agent wash-in and wash-out rates in PIN, as observed in this study, may contribute to the low-specificity to cancer associated with DCE-MRI, as many studies assessing cancer localization performance do not indicate whether PIN is identified or included as normal tissue. This result should be validated in a larger patient cohort.

This study was subject to several limitations. The number of patients included in each cohort was limited, and patient-specific variations may have contributed to the presence or absence of differences observed between pulse sequences, which are based entirely on between-subjects comparisons. Table 5.2 shows that patients in cohort A tended to have larger tumour volumes than patients in cohort B, which may have influenced results, although evidence suggests that the larger tumour volumes in cohort A would lead to improved cancer localization performance [46], which was not observed in this study. Furthermore, there were an unequal number of patients analyzed from each cohort, with 5 and 11 patients in cohort A and B respectively. The difference in cohort sizes likely contributed to the differences in statistical significance observed between cohorts in the within-subjects tests, such as the pairwise differences between parameter values in diseased and normal tissue. Our group is currently working to co-register whole-mount histology from an additional 8 patients in cohort A, and will report updated results once those patients have been included in the analysis. A major limitation of the pharmacokinetic modeling employed in this study was the calculation

of Gd concentrations based on relative T1w signal enhancement without quantitative voxel-wise or patient specific estimation of baseline T1 values, which were not measured for any patients in this study. Gd concentrations and resultant pharmacokinetic parameter values are sensitive to this source of error [41], which likely contributed to the differences observed in parameter mean values between cohorts.

The estimated 2 mm registration uncertainty between the whole-mount histology slides and *in vivo* MR images may have contributed to the poor contrast and voxel-wise classification performance measured for Gleason 3+3 cancer in the present study, particularly for small cancer components as indicated in Table 5.2. An alternative validation approach would be the comparison of DCE-MRI parameter maps with tissue cores obtained through MR-guided biopsies. However, a previous study estimated that the error in positioning biopsy cores using MR-guided approaches to be 3.5 mm [27], so would be unlikely to decrease the registration errors associated with the validation approach employed in this study.

5.5   Conclusions

The results of this hypothesis generating study suggest that increasing acquisition time per image to improve DCE-MRI spatial resolution may lead to an improvement in pharmacokinetic parameter contrast between high-grade cancer and normal prostate tissue, leading to an improvement in voxel-wise cancer classification performance. The parameter k_{ep} demonstrated advantages over K^{trans} for the pulse sequences investigated in this study. k_{ep}-RRM and k_{ep}-AIF provided the highest contrast between $\geq$Gleason 3+4 cancer and normal tissue for pulse sequences with acquisition times of 92.5 s/image and 6.4 s/image respectively, and k_{ep}-RRM demonstrated the smallest differences in patient-specific mean values between pulse sequences. Parameters derived from both pulse sequences demonstrated increased contrast and voxel-wise classification perfor-

mance of ≥Gleason 3+4 cancer compared to Gleason 3+3 cancer. mpMRI and post-prostatectomy specimens have been acquired from additional patients in cohort A and B, and we are currently working to analyze the data to include in the present study.

References

1. Weinreb, J. C. *et al.* PI-RADS Prostate Imaging - Reporting and Data System: 2015, Version 2. *European Urology* **69,** 16–40 (2016).

2. Barentsz, J. O. *et al.* ESUR prostate MR guidelines 2012. *European Radiology* **22,** 746–757 (2012).

3. Selnæs, K. M. *et al.* Peripheral zone prostate cancer localization by multiparametric magnetic resonance at 3 T. *Investigative Radiology* **47,** 624–633 (2012).

4. Gibson, E. *et al.* Toward prostate cancer contouring guidelines on magnetic resonance imaging: Dominant lesion gross and clinical target volume coverage via accurate histology fusion. *International Journal of Radiation Oncology Biology Physics* **96,** 188–196 (2016).

5. Tofts, P. S. *et al.* Estimating kinetic parameters from dynamic contrast-enhanced T1-weighted MRI of a diffusable tracer: Standardized quantities and symbols. *Journal of Magnetic Resonance Imaging* **10,** 223–232 (1999).

6. Kozlowski, P. *et al.* Combined diffusion-weighted and dynamic contrast-enhanced MRI for prostate cancer diagnosis - Correlation with biopsy and histopathology. *Journal of Magnetic Resonance Imaging* **24,** 108–113 (2006).

7. Ream, J. M. *et al.* Dynamic contrast-enhanced MRI of the prostate: An intraindividual assessment of the effect of temporal resolution on qualitative detection and quantitative analysis of histopathologically proven prostate cancer. *Journal of Magnetic Resonance Imaging, in Press* (2016).

8. Van Niekerk, C. G. *et al.* Correlation between dynamic contrast-enhanced MRI and quantitative histopathologic microvascular parameters in organ-confined prostate cancer. *European Radiology* **24,** 2597–2605 (2014).

9. Pallares, J. *et al.* Study of microvessel density and the expression of the angiogenic factors VEGF, bFGF and the receptors Flt-1 and FLK-1 in benign, premalignant and malignant prostate tissues. *Histology and Histopathology* **21,** 857–865 (2006).

10. Chen, Y. J. *et al.* Washout gradient in dynamic contrast-enhanced MRI is associated with tumor aggressiveness of prostate cancer. *Journal of Magnetic Resonance Imaging* **36,** 912–919 (2012).

11. Aerts, H., Jaspers, K. & Backes, W. The precision of pharmacokinetic parameters in dynamic contrast-enhanced magnetic resonance imaging: The effect of sampling frequency and duration. *Physics in Medicine and Biology* **56** (2011).

12. Heisen, M. *et al.* The influence of temporal resolution in determining pharmacokinetic parameters from DCE-MRI data. *Magnetic Resonance in Medicine* **63,** 811–816 (2010).

13. Cron, G. O. *et al.* Arterial input functions determined from MR signal magnitude and phase for quantitative dynamic contrast-enhanced MRI in the human pelvis. *Magnetic Resonance in Medicine* **66,** 498–504 (2011).

14. Parker, G. J. M. *et al.* Experimentally-derived functional form for a population-averaged high-temporal-resolution arterial input function for dynamic contrast-enhanced MRI. *Magnetic Resonance in Medicine* **56,** 993–1000 (2006).

15. Othman, A. E. *et al.* Effect of temporal resolution on diagnostic performance of dynamic contrast-enhanced magnetic resonance imaging of the prostate. *Investigative Radiology* **51,** 290–296 (2016).

16. Kovar, D. a., Lewis, M. & Karczmar, G. S. A new method for imaging perfusion and contrast extraction fraction: Input functions derived from reference tissues. *Journal of Magnetic Resonance Imaging* **8,** 1126–1134 (1998).

17. Yankeelov, T. E. *et al.* Comparison of a reference region model with direct measurement of an AIF in the analysis of DCE-MRI data. *Magnetic Resonance in Medicine* **57,** 353–361 (2007).

18. Cárdenas-Rodríguez, J., Howison, C. M. & Pagel, M. D. A linear algorithm of the reference region model for DCE-MRI is robust and relaxes requirements for temporal resolution. *Magnetic Resonance Imaging* **31,** 497–507 (2013).

19. Planey, C. R. *et al.* Temporal sampling requirements for reference region modeling of DCE-MRI data in human breast cancer. *Journal of Magnetic Resonance Imaging* **30,** 121–134 (2009).

20. Heisen, M. *et al.* The use of a reference tissue arterial input function with low-temporal-resolution DCE-MRI data. *Physics in Medicine and Biology* **55,** 4871–4883 (2010).

21. Rosenkrantz, A. B. *et al.* Dynamic contrast-enhanced MRI of the prostate with high spatiotemporal resolution using compressed sensing, parallel imaging, and continuous golden-angle radial sampling: Preliminary experience. *Journal of Magnetic Resonance Imaging* **41,** 1365–1373 (2014).

22. Roy, C. *et al.* Comparative sensitivities of functional MRI sequences in detection of local recurrence of prostate carcinoma after radical prostatectomy or external-beam radiotherapy. *American Journal of Roentgenology* **200,** 361–368 (2013).

23. Rouvière, O. *et al.* Is it possible to model the risk of malignancy of focal abnormalities found at prostate multiparametric MRI? *European Radiology* **22,** 1149–1157 (2012).

24. Rosenkrantz, A. B. *et al.* Detection of prostate cancer local recurrence following radical prostatectomy: assessment using a continuously acquired radial golden-angle compressed sensing acquisition. *Abdominal Radiology* **42,** 1–8 (2016).

25. Riederer, S. J. *et al.* Improved performance of prostate DCE-MRI using a 32-coil vs. 12-coil receiver array. *Magnetic Resonance Imaging* **In Press** (2017).

26. Epstein, J. I., Walsh, P. C., Carmichael, M. & Brendler, C. B. Pathologic and clinical findings to predict tumor extent of nonpalpable (stage T1c) prostate cancer. *Journal of the American Medical Association* **271,** 368–374 (1994).

27. Martin, P. R., Cool, D. W., Romagnoli, C., Fenster, A. & Ward, A. D. Magnetic resonance imaging-targeted, 3D transrectal ultrasound-guided fusion biopsy for prostate cancer: Quantifying the impact of needle delivery error on diagnosis. *Medical Physics* **41,** 073504 (2014).

28. Degani, H., Gusis, V., Weinstein, D., Fields, S. & Strano, S. Mapping patho-physiological features of breast tumors by MRI at high spatial resolution. *Nature Medicine* **3,** 780–782 (1997).

29. Eyal, E. *et al.* Principal component analysis of dynamic contrast enhanced MRI in human prostate cancer. *Investigative Radiology* **45,** 174–181 (2010).

30. Furman-Haran, E., Grobgeld, D., Kelcz, F. & Degani, H. Critical role of spa-tial resolution in dynamic contrast-enhanced breast MRI. *Journal of Magnetic Resonance Imaging* **13,** 862–867 (2001).

31. Kelcz, F., Furman-Haran, E., Grobgeld, D. & Degani, H. Clinical testing of high-spatial-resolution parametric contrast-enhanced MR imaging of the breast. *American Journal of Roentgenology* **179,** 1485–1492 (2002).

32. Fedorov, A. *et al.* 3D Slicer as an image computing platform for the Quantitative Imaging Network. *Magnetic Resonance Imaging* **30,** 1323–1341 (2012).

33. Mattes, D., Haynor, D. R., Vesselle, H., Lewellen, T. K. & Eubank, W. PET-CT image registration in the chest using free-form deformations. *IEEE Transactions on Medical Imaging* **22,** 120–128 (2003).

34. Byrd, R. H., Lu, P., Nocedal, J. & Zhu, C. A limited memory algorithm for vound constrained optimization. *Society of Industrial and Applied Mathematics* **16,** 1190–1208 (1995).

35. Dathe, H. & Helms, G. Exact algebraization of the signal equation of spoiled gradient echo MRI. *Physics in Medicine and Biology* **55,** 4231–4245 (2010).

36. De Bazelaire, C. M. J., Duhamel, G. D., Rofsky, N. M. & Alsop, D. C. MR imaging relaxation times of abdominal and pelvic tissues measured in vivo at 3.0 T: preliminary results. *Radiology* **230,** 652–659 (2004).

37. Donahue, K. M. & Donahue, K. M. Studies of Gd-DTPA relaxivity and proton exchange rates in tissue with implications for MR imaging of regional myocar-dial perfusion. *Magnetic Resonance in Medicine* **32,** 66–76 (1993).

38. Yankeelov, T. E. *et al.* Quantitative pharmacokinetic analysis of DCE-MRI data without an arterial input function: A reference region model. *Magnetic Reso-nance Imaging* **23,** 519–529 (2005).

39. Gibson, E. *et al.* Registration of prostate histology images to ex vivo MR images via strand-shaped fiducials. *Journal of Magnetic Resonance Imaging* **36,** 1402–1412 (2012).

40. Robin, X. *et al.* pROC: an open-source package for R and S+ to analyze and compare ROC curves. *BMC Bioinformatics* **12,** 1–8 (2011).

41. Subashi, E., Choudhury, K. R. & Johnson, G. A. An analysis of the uncertainty and bias in DCE-MRI measurements using the spoiled gradient-recalled echo pulse sequence. *Medical Physics* **41,** 032301 (2014).

42. Gudbjartsson, H. & Patz, S. The rician distribution of noisy MRI data. *Magnetic Resonance in Medicine* **34,** 910–914 (1995).

43. Li, X. *et al.* Relative sensitivities of DCE-MRI pharmacokinetic parameters to arterial input function (AIF) scaling. *Journal of Magnetic Resonance* **269,** 104–112 (2016).

44. Hamy, V. *et al.* Respiratory motion correction in dynamic MRI using robust data decomposition registration - Application to DCE-MRI. *Medical Image Analysis* **18,** 301–313 (2014).

45. Bostwick, D. G. & Brawer, M. K. Prostatic intra-epithelial neoplasia and early invasion in prostate cancer. *Cancer* **59,** 788–794 (1987).

46. Steenbergen, P. *et al.* Prostate tumor delineation using multiparametric magnetic resonance imaging: Inter-observer variability and pathology validation. *Radiotherapy and Oncology* **115,** 186–190 (2015).

Chapter 6

Conclusions, Limitations, and Future Work

Tumour-targeted HDR-BT may lead to improvements in therapeutic ratio for prostate cancer, but HDR-BT treatment plans are critically sensitive to uncertainty in needle tip positions relative to anatomy. Imaging and treatment planning must be performed efficiently while the patient is anesthetized. The efficacy of tumour-targeted treatments also depends on the ability to localize prostate tumours using mpMRI incorporating DCE-MRI. The purpose of Chapter 6 is to summarize the contributions, conclusions, and limitations of Chapters 2-5 in improving and evaluating TRUS and DCE-MRI for tumour-targeted HDR-BT, and to discuss areas for future work.

6.1   Contributions and Conclusions

Chapter 2: SR3D TRUS for Needle Tip Localization

Conventional sagitally-assisted axially-reconstructed (SAAR)-guided HDR-BT uses AR3D images for organ segmentation and live-2D sagittal images for needle tip segmentation [1]. SAAR-guidance requires movement of the probe in the superior/inferior direction between imaging organs and needle tips, introducing a source of uncertainty in the final set of segmentations used for treatment planning. Chapter 2 addressed this source of uncertainty by implementing SR3D TRUS for needle tip localization, which eliminates the need to move the probe in the superior/inferior direction for 3D image reconstruction. A comparison of SAAR and SR3D-based needle tip positions to

needle end-length measurements in 12 patients demonstrated statistically significantly smaller insertion depth errors (*IDE*s) associated with SR3D than SAAR-guidance, with mean±SD of -0.6±3.2 mm and 2.8±3.2 mm, respectively (p <.001). Dosimetric simulations demonstrated that SR3D led to decreased error in the volume of the prostate recieving the prescribed dose than SAAR, with mean±SD decreases of -1.2±1.3% and -6.5±6.7%, respectively (p <.05). SR3D-guided HDR-BT eliminates a source of systematic uncertainty from the conventional approach, providing decreased *IDE*s for the majority of needles and leading to a significant decrease in dosimetric uncertainty. However, using a single SR3D image with all needles inserted for tip localization was found to be limited by shadow artifacts. These artifacts were found to obstruct the view of a portion of needle tips in SR3D-images either partially (12% of needles) or fully (10% of needles). This finding led to work using live-2D sagittal TRUS in Chapter 4.

Chapter 3: Automatic Segmentation of Multiple Needles using SR3D TRUS

Automatic needle segmentation has the potential to decrease the time required for intra-operative HDR-BT treatment planning, but existing automatic needle segmentation algorithms have not been designed to handle 3D TRUS images containing multiple needles. Chapter 3 presented and characterized an automatic needle segmentation algorithm designed for HDR-BT, specifically capable of simultaneously segmenting multiple needles in an HDR-BT implant using a single SR3D image with ~5 mm inter-needle spacing. This algorithm was used to automatically segment needles in the SR3D images from 12 patients acquired in Chapter 2, demonstrating mean execution times of 11.0 s per patient, or 0.7 s per needle. The algorithm identified 82% and 85% of needle tips with 3D errors ≤3 mm and ≤5 mm, respectively, and 83% of needle trajectories with angular errors ≤3°. The largest tip error component was in the needle insertion direction. The automatic segmentation results should be considered in the context of

the results of Chapter 2, which demonstrated that HDR-BT needles may be manually segmented using SR3D images with *IDE*s ≤3 mm and ≤5 mm for 83% and 92% of needles, respectively. This algorithm shows promise to reduce the time required for HDR-BT treatment planning by initializing needle segmentations, which may then be verified manually. Similar to manual needle segmentation, shadow artifacts in the SR3D images were found to limit geometric performance of the algorithm, leading to the work in Chapter 4.

Chapter 4: Improved Needle Tip Localization using Live-2D and SR3D TRUS

The results of Chapters 2 and 3 provided evidence that shadow artifacts in SR3D images limit both manual and automatic needle tip localization accuracy, limiting the potential for clinical implementation of SR3D-guided brachytherapy using the mechatronic device investigated. Chapter 4 addressed this limitation by proposing a needle tip localization method that augmented the SR3D images with live-2D sagittal images acquired at the time of needle insertion. The live-2D images did not add time to the HDR-BT procedure, and could be related to a final SR3D image geometrically using the mechatronic device encoders. The proposed sagittally-assisted sagittally-reconstructed (SASR) technique enabled the localization of all needles from another cohort of 10 patients with *IDE*s within ±3 mm for 84% of needles and *IDE* range of [-6.2 mm, 5.9 mm], compared to 57% and [-8.1 mm, 7.7 mm] when using the clinical SAAR technique. Segmentation results from two users indicated that inter-operator variability in SASR-based tip positions was largest in the insertion direction, with 95% prediction intervals within [-0.6 mm, 1.5 mm]. The proposed SASR technique overcomes a major limitations in SR3D-guided needle segmentation by incorporating mechanically registered live-2D sagittal images, mitigating the impact of image artifacts. The ability to segment all needle tips in the cohort of 10 patients indicates that the SASR technique

is sufficiently robust for clinical implementation. At out center we are currently transitioning from SAAR-guidance to SASR-guidance for routine whole-gland HDR-BT.

Chapter 5: Spatial *versus* Temporal Resolution of DCE-MRI

Consensus guidelines recommend DCE-MRI for prostate cancer localization with acquisition times ≤7 s/image [2]. Conversely, recent simulation studies indicated that prostate cancer localization performance is robust up to acquisition times of at least 15 s/image [3], suggesting that it may be possible to improve prostate cancer boundary localization performance by increasing DCE-MRI spatial resolution at the expense of temporal resolution. Chapter 5 investigated this trade-off by comparing DCE-MRI acquired using one of two pulse sequences with mean acquisition times of 6.4 s/image (5 patients) and 92.5 s/image (11 patients) to deformably registered whole-mount histology. Data from 16 patients indicated that the pharmacokinetic rate constant (k_{ep}) derived from the 92.5 s/image sequence provided the highest contrast between high-grade cancer (≥Gleason 3+4) and normal tissue, with mean±SD contrast of 1.21±0.84 *versus* 0.45±0.35 for the 6.4 s/image sequence (p = .023) when calculated using a population averaged arterial input function (AIF). k_{ep} from the 92.5 s/image sequence also provided area under the ROC curve of 0.79 for voxel-wise classification of high-grade cancer *versus* 0.70 for the 6.4 s/image sequence. These preliminary results suggest parameters derived from DCE-MRI acquired at 92.5 s/image with 0.27×0.27 mm^2 in-plane voxel dimensions provide improved contrast between high-grade cancer and normal prostate tissue compared to DCE-MRI acquired at 6.4 s/image with 0.55×0.55 mm^2 in-plane voxel dimensions, leading to an improvement in voxel-wise cancer classification performance.

6.2   Limitations

6.2.1   Study Specific Limitations

Chapter 2: SR3D TRUS for Needle Tip Localization

HDR-BT needle tip localization accuracy relative to anatomy is critical for treatment planning accuracy. In Chapter 2, this accuracy was estimated in the needle insertion direction (superior/inferior) by comparing image-based tip positions to calibrated needle end-length measurements. The interpretation of the resultant insertion depth errors assumes that the prostate and surrounding anatomy remains stationary relative to the insertion template between imaging and treatment delivery. We reduced the possibility of such motion by locking all needles into place following insertion and prior to imaging, and minimizing probe movement following imaging and prior to treatment delivery. However, we did not directly measure tip locations relative to anatomy, and any anatomical motion (such as prostate swelling) could introduce additional error in the results [4]. Furthermore, the sampling intervals used for AR3D acquisition in this study were limited to 5 mm by the commercial system available at our center. Other commercially available systems enable AR3D sampling intervals of 1 mm, but increasing AR3D spatial resolution through increased sampling is limited by the elevational resolution of the axial transducer, measured to be 1.5 - 4.0 mm depending on distance from the probe [5].

Chapter 3: Automatic Segmentation of Multiple Needles Using SR3D TRUS

The primary limitation of the algorithm proposed in this study is that all HDR-BT needles were modeled as straight lines. Needles may bend when inserted in tissue [6], so an updated algorithm modeling curved trajectories may be required for widespread implementation. Furthermore, the algorithm currently requires manual needle labeling for treatment planning, involving the selection of needle label points on a live-2D axial

view. The algorithm also led to segmentation failures in 7.3% of needles, and 3D tip errors >9 mm in 2.1% of unobstructed needles, indicating the need for manual quality assurance. The need for manual labeling and quality assurance indicates that this algorithm can enhance segmentation efficiency, but is not yet ready as a fully automatic solution for HDR-BT needle segmentation.

Chapter 4: Improved Needle Tip Localization Using Live-2D and SR3D TRUS

The limitations of this study are due to the limitations identified in Chapter 2; namely, indirect measurement of needle tip locations relative to anatomy and the limited 5 mm sampling intervals of the AR3D TRUS images used for comparison. Furthermore, we did not directly assess the dosimetric impact of the needle *IDE*s measured using this updated needle tip localization technique. Based on the dosimetric simulations performed in Chapter 2, we expect the uncertainty in prostate V100% associated with needle tip localization in this study to be <4%. It is possible that prostate and urethra segmentation may now contain greater dosimetric uncertainties than those associated with the needle tip localization errors measured in this study [7], and a more representative dosimetric simulation of the SASR workflow for whole-gland treatment would incorporate a model of uncertainty in organ segmentations.

Chapter 5: Spatial vs. Temporal Resolution of DCE-MRI

The primary limitation of this study is the number of patients included in the analysis (n=16), particularly in cohort A (n=5). The comparison of pulse sequences in this study depended entirely on between-subjects comparisons, and the heterogeneity of prostate cancer may have impacted the differences between pulse sequences observed. As mentioned, we are in the process of analyzing an additional 8 patients to be included in cohort A, and will report updated results once those patients have been included in the analysis. An additional limitation of this study was the inability to identify the spe-

cific pulse sequence characteristic leading to improved high-grade cancer localization observed in cohort B. Potential characteristics include increased spatial resolution, or increased SNR associated with the 92.5 s/image pulse sequence compared to the 6.4 s/image pulse sequence. We intend to perform a simulation study in which the images from cohort B are spatially down-sampled to directly investigate the hypothesis that improved spatial resolution is the reason for the improved high-grade cancer localization observed in cohort B.

6.2.2 General Limitations

A general limitation of Chapters 2-4 was the lack of comparison between the SR3D images produced using our custom mechatronic device [8] and the SR3D images produced by commercially available systems. For instance, Gomez-Iturriaga et al. used Elekta's SR3D TRUS imaging system for tumour targeted HDR-BT [9] with identical 0.5° angular sampling intervals as those used for SR3D acquisition and reconstruction in Chapters 2-5. While the property of sub-millimeter spatial resolution in the needle insertion direction should be consistent across SR3D reconstruction methods, it would be ideal to compare performance and workflows directly for direct application of the results in these studies to commercial systems currently used at other centers.

Finally, the tumour-targeted HDR-BT workflow motivating the work in this thesis requires image registration between the mpMRI and SR3D TRUS for treatment planning. Deformable image registration between MRI and SR3D TRUS has been investigated in the past, demonstrating 2 mm target registration error when using surface-based techniques developed by our group [10], but this has not been demonstrated in SR3D TRUS images containing ~15-20 needles that would be used for HDR-BT treatment planning. This component of error in the treatment planning workflow was not addressed in this thesis, and should be characterized and included in the overall uncertainty model when developing planning target volume (PTV) expansions (i.e. contour

expansions intended to encompass treatment delivery uncertainty) for tumour-targeted HDR-BT.

6.3 Future Work

Planning Target Volume Expansions for Tumour-Targeted HDR-BT

Chapter 4 characterized a needle tip localization technique that can be implemented for clinical whole-gland HDR-BT treatment planning. As previously mentioned, tumour-targeted HDR-BT treatment plans are more sensitive to needle tip localization errors than whole-gland treatment plans [11]. The distributions of needle insertion depth errors and inter-operator variability in needle tip positions measured in Chapter 4 may be used as a model of uncertainty in a tumour-targeted HDR-BT treatment planning study. By incorporating models of uncertainty in tumour localization using mpMRI (such as the contouring uncertainty measured by Gibson et al. [12]) and a model of uncertainty in deformable mpMRI-to-SR3D registration [10], it will be possible to conduct a thorough evaluation of impact of the uncertainty components on tumour-targeted HDR-BT dosimetry to derive PTV expansions that provide a known probability of DIL coverage (e.g. 95%).

Specifically, tumour-targeted treatment plans could be simulated, and DIL contours and radiation source positions could be randomly perturbed according to the error distributions measured for each component of the treatment planning process, followed by re-calculation of dosimetric parameters. PTV expansions of increasing size could be added to the DIL clinical target volume (CTV) until the volume of the CTV receiving the prescription dose was at least 95% for 95% of perturbations (for example). Dose to critical structures such as the urethra and rectum could be assessed through these simulations to determine dose-limiting factors to tumour-targeted treatments, such as DIL volume or DIL location within the prostate.

Implementing New Imaging Tools in a Clinical Trial

Tumour-targeted TRUS-guided HDR-BT has been investigated in multiple clinical trials [9, 13]; however, these trials did not include PTV expansions to account for uncertainties in needle tip localization or prostate tumour localization. The technical developments in this thesis may be directly applied to similar clinical trials with: 1) reduced needle tip localization uncertainty, 2) reduced time required for intra-operative needle segmentation, and 3) improved tumour localization performance through increased DCE-MRI spatial resolution. By increasing imaging accuracy and deriving PTV expansions from the uncertainties associated with these imaging tools, it will be possible to improve the probability of delivering the intended prescription dose to the DIL. Since bDFS following whole-gland HDR-BT is impacted by target coverage [14], improved probability of DIL coverage with tumour-targeted HDR-BT may lead to improvements in bDFS associated with these treatments. To this end, we are in the process of completing a Health Sciences Research Ethics Board submission for a clinical trial investigating tumour-targeted HDR-BT using the imaging tools described in this thesis.

Radiobiology of High Single Fraction Doses

With the potential for single fraction doses >19 Gy delivered to DIL with tumour-targeted HDR-BT, the radiobiological mechanisms leading to cell death may be different than the clonogenic or "replicative" cell death associated with the DNA damage caused by conventional fractionated radiotherapy [15]. Radiotherapy initiates a cascade of cellular processes, and combinations of radiotherapy and drugs designed to enhance immune response (immune checkpoint inhibitors) have demonstrated synergistic effects, suggesting that radiotherapy may be used to modulate an immune response to cancer [15]. However, these experiments have also demonstrated that the synergistic effects of combination treatments are sensitive to the dose and scheduling of the radiotherapy and immune therapies [16]. Precise control of prostate tumour doses using

HDR-BT may facilitate clinical trials investigating these treatments in humans. Combination therapies leading to an immune response to cancer are promising for the creation of curative treatments for high-risk prostate cancer due to the potential for "out-of-field" effects, where cancer cells both inside and outside of the treatment field are controlled [15].

A unique feature of the mechatronic device investigated in this thesis is the ability to perform oblique needle insertions using interactive tracked needle guides [8]. This feature may enable accurate trans-perineal biopsy either during or following dose-escalated tumour-targeted HDR-BT, with biopsy cores oriented to maximize tumour sampling. Histological analysis of biopsy samples pre and post-dose-escalated treatment using stains for DNA double strand breaks [17] combined with measurements of circulating T-cells [18] may provide some insight into radiobiological processes taking place at very high doses in prostate cancer patients.

References

1. Batchelar, D. *et al.* Validation study of ultrasound-based high-dose-rate prostate brachytherapy planning compared with CT-based planning. *Brachytherapy* **13,** 75–79 (2014).

2. Weinreb, J. C. *et al.* PI-RADS Prostate Imaging - Reporting and Data System: 2015, Version 2. *European Urology* **69,** 16–40 (2016).

3. Ream, J. M. *et al.* Dynamic contrast-enhanced MRI of the prostate: An intraindividual assessment of the effect of temporal resolution on qualitative detection and quantitative analysis of histopathologically proven prostate cancer. *Journal of Magnetic Resonance Imaging, in Press* (2016).

4. Kim, Y., Hsu, I.-C. C., Lessard, E., Vujic, J. & Pouliot, J. Dosimetric impact of prostate volume change between CT-based HDR brachytherapy fractions. *International Journal of Radiation Oncology Biology Physics* **59,** 1208–1216 (2004).

5. Peikari, M. *et al.* Characterization of ultrasound elevation beamwidth artifacts for prostate brachytherapy needle insertion. *Medical Physics* **39,** 246–256 (2012).

6. Wan, G., Wei, Z., Gardi, L., Downey, D. B. & Fenster, A. Brachytherapy needle deflection evaluation and correction. *Medical Physics* **32,** 902–909 (2005).

7. Rylander, S., Buus, S., Pedersen, E., Bentzen, L. & Tanderup, K. Dosimetric impact of contouring and needle reconstruction uncertainties in US-, CT- and MRI-based high-dose-rate prostate brachytherapy treatment planning. *Radiotherapy and Oncology* **in Press** (2017).

8. Bax, J. *et al.* A compact mechatronic system for 3D ultrasound guided prostate interventions. *Medical Physics* **38,** 1055–1069 (2011).

9. Gomez-Iturriaga, A. *et al.* Dose escalation to dominant intraprostatic lesions with MRI-transrectal ultrasound fusion high-dose-rate prostate brachytherapy. Prospective phase II trial. *Radiotherapy and Oncology* **119,** 91–96 (2016).

10. Sun, Y., Qiu, W., Romagnoli, C. & Fenster, A. 3D non-rigid surface-based MR-TRUS registration for image-guided prostate biopsy. *Progress in Biomedical Optics and Imaging - Proceedings of SPIE,* 90362 (2014).

11. Mason, J., Al-Qaisieh, B., Bownes, P., Thwaites, D. & Henry, A. Dosimetry modeling for focal high-dose-rate prostate brachytherapy. *Brachytherapy* **13,** 611–617 (2014).

12. Gibson, E. *et al.* Toward prostate cancer contouring guidelines on magnetic resonance imaging: Dominant lesion gross and clinical target volume coverage via accurate histology fusion. *International Journal of Radiation Oncology Biology Physics* **96,** 188–196 (2016).

13. Crook, J. *et al.* Ultrasound-planned high-dose-rate prostate brachytherapy: Dose painting to the dominant intraprostatic lesion. *Brachytherapy* **13,** 433–441 (2014).

14. Hoskin, P. J. *et al.* Dosimetric predictors of biochemical control of prostate cancer in patients randomised to external beam radiotherapy with a boost of high dose rate brachytherapy. *Radiotherapy and Oncology* **110,** 110–113 (2014).

15. Derer, A., Frey, B., Fietkau, R. & Gaipl, U. S. Immune-modulating properties of ionizing radiation: rationale for the treatment of cancer by combination radiotherapy and immune checkpoint inhibitors. *Cancer Immunology, Immunotherapy* **65,** 779–786 (2016).

16. Harris, T. J. *et al.* Radiotherapy augments the immune response to prostate cancer in a time-dependent manner. *Prostate* **68,** 1319–1329 (2008).

17. Kinner, A., Wu, W., Staudt, C. & Iliakis, G. Gamma-H2AX in recognition and signaling of DNA double-strand breaks in the context of chromatin. *Nucleic Acids Research* **36,** 5678–5694 (2008).

18. Morgan, R. A. *et al.* Cancer regression in patients after transfer of genetically engineered lymphocytes. *Science* **314,** 126–129 (2006).

Appendix A

Appendix to Chapter 2

A.1 Intra-Operative Image Acquisition and SAAR Workflow

Under general anesthesia, patients were placed in the dorsal lithotomy position and a Foley catheter was inserted into the bladder. The mechatronic device was positioned with the HDR-BT template against the perineum. As mentioned in the methods section, contiguous axial image sets and SR3D images were acquired before and after needle insertion. Superior/inferior encoder values were recorded for all axial and SR3D image acquisitions. Initial prostate, urethra, rectum, and bladder contours were created with Vitesse on the pre-insertion 2D axial images as indicated in Figure 2.1. To deliver the 15 Gy brachytherapy dose, a median (range) of 15 (14-20) FlexiGuide HDR-BT needles was implanted. Needles were positioned to cover the prostate periphery and interior based on the mid-gland axial cross-section. Rigid steel pathfinder needles were inserted prior to each FlexiGuide needle to create paths for the needles to follow. Once all needles were inserted, the TRUS view was switched from axial to sagittal view and the organ segmentations previously created with Vitesse on the axial image set were manually aligned in the superior/inferior direction with the live mid-gland sagittal view. This enabled the alignment of the needle and organ segmentations as indicated in Figure

2.1. Working anteriorly-to-posteriorly, needles were advanced to the desired insertion depth under sagittal 2D guidance and the needle tips were identified and segmented on the live ultrasound view using Vitesse. One of three operators segmented needle tips on Vitesse for each patient.

Once all needles were inserted to the required depth, they were locked in place and the stylets were removed before a final set of contiguous 2D axial images was acquired at 5 mm intervals. These images were acquired starting at a point that matched as closely as possible the anatomical positions of the pre-insertion axial image set. A second SR3D image was acquired immediately following the axial image set. Based on the final axial image set, needle positions were verified and any apparent curved trajectories were accounted for using the Vitesse software tools. If necessary, prostate and organ contours were adjusted to account for post-implant deformation and organ motion. The organ contours, needle segmentations, and 2D images were then imported into BrachyVision for treatment planning. The completed plan was delivered with the patient under general anesthesia with the transrectal probe *in situ*.

A.2 String Phantom Calibration

The mechatronic device incorporates encoders that track both the probe tilt angle for SR3D image reconstruction with nominal $0.08°$ angular resolution, and the longitudinal (superior/inferior) probe position within ± 0.1 mm. Since the template holder rigidly affixes the insertion template to the mechatronic device and the device remains stationary during the HDR-BT procedure, the longitudinal encoder position can be used to determine the distance between each image and the template face ($d_{encoder}$) allowing the use of needle free-end lengths (d_{end}) to verify insertion depths as indicated in Figure 2.2. The relationship between the longitudinal encoder position and the template face depends on the probe geometry, transducer position, and template thickness. The tem-

plate thickness was accounted for by physically measuring the template. To account for the probe geometry and transducer position, a phantom was constructed that rigidly attached to the mechatronic device template mounting point shown in Figure A.1a. The phantom frame was constructed out of thermoplastic and polycarbonate for structural rigidity and incorporated 0.1 mm diameter strings at specified positions relative to the mounting point. The frame and string mounting holes were machined to 0.05 mm tolerances. Strings were positioned in the transverse direction to estimate superior/inferior image position using the sagittal transducer. Strings were also positioned to create two z-frames along sagittal planes to enable the estimation of superior/inferior axial crystal position, as highlighted in Figure A.1b.

The phantom was scanned in a bath of water and 7% glycerol per weight for a speed of sound matching soft tissue [1] using this study's BK ProFocus ultrasound machine and 8848 bi-plane transducer scanning at 9 MHz and 6.3 cm field of view. An SR3D image was acquired at 0.5° angular intervals and the raw superior/inferior encoder position was recorded. Next, a set of contiguous 2D axial images were acquired in 5 mm steps and captured using Vitesse segmentation software, again recording the raw encoder value of each image. All phantom images were imported into 3D Slicer 4.4 [2] for analysis. Example phantom images are provided in Figure A.2. The distance between the transverse strings in the SR3D image to the inferior edge of the image were measured. Based on the raw encoder value and known position of the strings relative to the template holder, a superior/inferior calibration value was calculated for the sagittal crystal. Next, the 2D axial image set was rigidly registered to the SR3D image based on the z-frames present in each image. The z-frame registration technique allows the estimation of superior/inferior image position using axial views based on the relative distances of the strings from one another within each z-frame. Using the resultant rigid registration transformation matrix and raw encoder positions of the images, the distance between the superior edge of a 2D sagittal image and the center of an axial
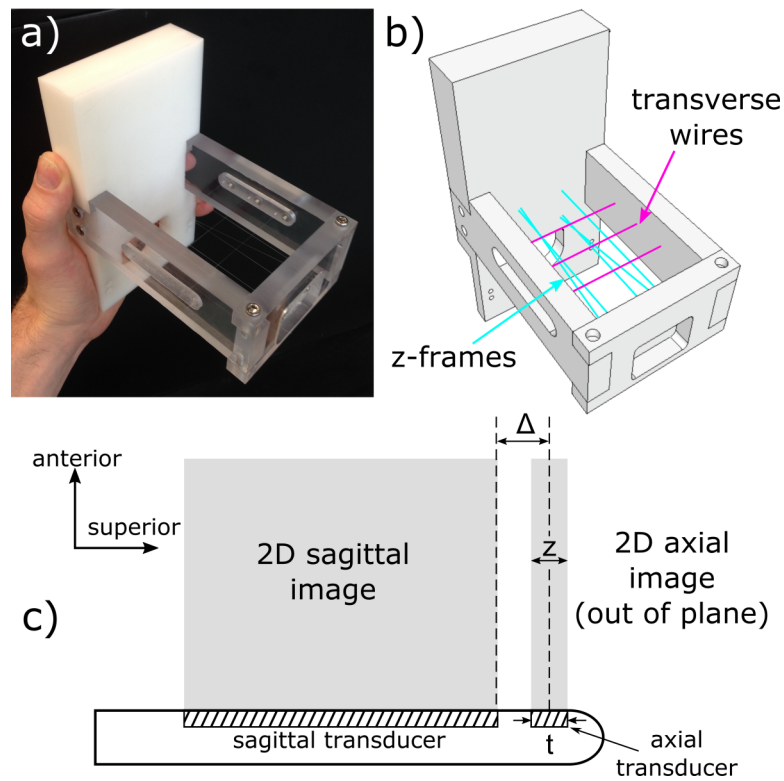
Figure A.1: a) Photo of the string phantom used for encoder calibration and measurement of the distance between the axial and sagittal transducers of the BK 8848 bi-plane TRUS probe. b) 3D rendering of the string phantom with the z-frames and transverse wire positions highlighted in cyan and magenta. c) Schematic of the transrectal probe geometry showing the crystal positions and the resulting 2D image for both sagittal and axial transducers. Note that the crystal thickness, t, is in general not the same as the axial slice thickness, z. The transducer-offset Δ, which is required for image registration, was measured to be 4.6 mm using the string phantom.

image (Δ) was measured to be 4.6 mm, as shown in Figure A.1. By combining the measured template thickness, sagittal crystal transducer calibration value, and distance between sagittally- and axially-acquired images, the raw encoder values could be used to calculate image position relative to the template face ($d_{encoder}$).
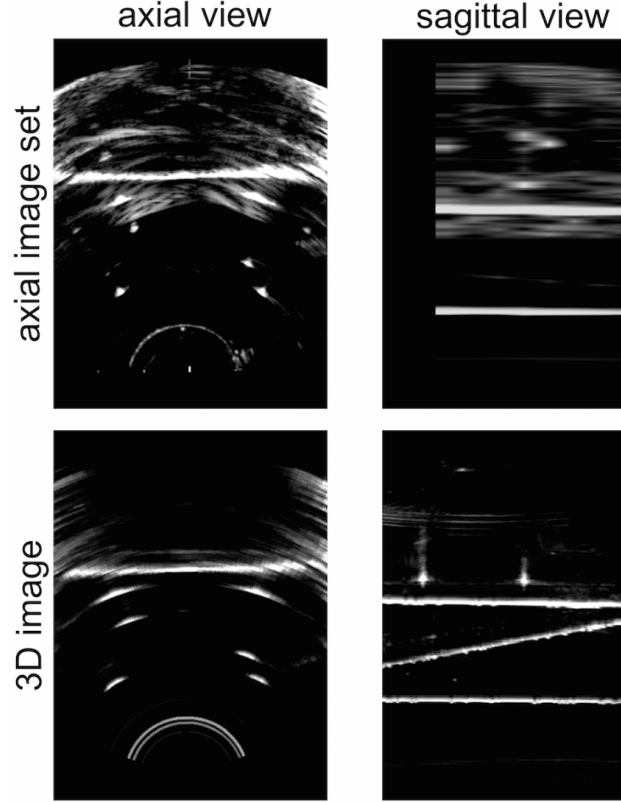
Figure A.2: Example co-registered axial and sagittal views of the string phantom displaying the z-frames and transverse wires used for superior/inferior encoder calibration. The top row corresponds to an image-set acquired using the axial crystal and the bottom row corresponds to a SR3D image.

The estimated upper bound of uncertainty in the encoder calibration was on the order of ±0.5 mm based on the width of the phantom strings as appearing in TRUS images, and the encoder indicating superior/inferior image position had a spatial resolution of 0.1 mm. An upper bound on uncertainty in the free-end length measurements acquired intra-operatively was also on the order of ±0.5 mm due to limitations in the ability to physically measure FlexiGuide needle lengths using a graduated ruler. Nee-

dle obliquity was also not accounted for in the hidden space between the template face and SR3D image ($d_{encoder}$); however, given that needle deflection was not expected to be more than 5° and this intervening space has a typical length of 100 mm, an upper bound for this error was estimated at ±0.4 mm.
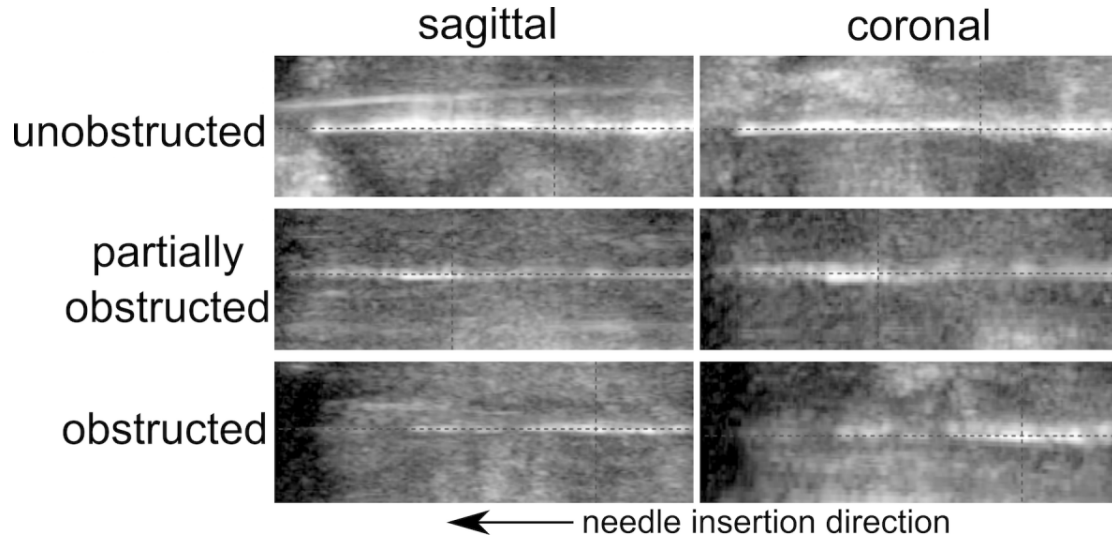
Figure A.3: Examples of unobstructed, partially obstructed, and obstructed needle tips provided as a supplementary file to the manuscript.

References

1. Tong, S., Downey, D. B., Cardinal, H. N. & Fenster, A. A three-dimensional ultrasound prostate imaging system. *Ultrasound in Medicine and Biology* **22,** 735–746 (1996).

2. Fedorov, A. *et al.* 3D Slicer as an image computing platform for the Quantitative Imaging Network. *Magnetic Resonance Imaging* **30,** 1323–1341 (2012).

Appendix B

Appendix to Chapter 3

B.1   Manual Segmentation Analysis

Figure B.1a shows a histogram of needle trajectory angles relative to the z-axis for all 185 plastic needles that could be manually segmented, demonstrating that the largest angle was <10°. The elevational angle (θ) search space of randomized 3DHT was then limited to the range [0°, 10°] as described in section 3.2.2. Figure B.1b shows a histogram of the shortest distance in the axial plane to the nearest adjacent needle within the SR3D image for the manually segmented needles. Three pairs of needles had distances between one another <3mm (2.9 mm, 2.7 mm, and 2.1 mm). Five out of six of these needles were considered partially obstructed or obstructed by shadow artifacts at the time of manual segmentation, and the diameter of the plastic needles used in this study was 2 mm. A minimum separation distance of 3 mm in the axial plane was enforced between feature points as described in section 3.2.2. Figure B.2a shows a boxplot of the length of each needle within the SR3D image, referred to as insertion depths, for each individual patient and all patients combined. Figure B.2b then shows a boxplot of insertion depths after subtracting the median insertion depth for each patient. Limits of -12 mm and 10 mm are indicated, which encompass 98% of all needles. These limits were used to bound the insertion depth search space in the second step of the tip localization algorithm, as described in section 3.2.2.
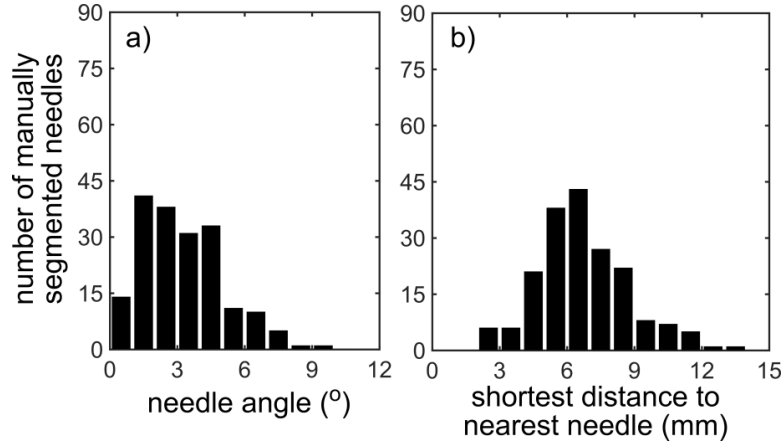
Figure B.1: a) Histogram of needle trajectory angles relative to the superior/inferior (z)-axis and b) histogram of the shortest distance in the axial plane to the nearest adjacent needle within the SR3D image for 185 manually segmented needles.

B.2 Signal Intensity Profile Analysis for Tip Localization

B.2.1 Oriented Sub-Volume Cropping

Intensity profiles were obtained by cropping regions of interest surrounding each trajectory, then filtering and averaging the signal intensity in directions normal to the trajectory. The cropping region was 1.6 mm in the radial direction, and 4.7 mm in the tangential direction, corresponding to the intervals expected to contain 95% of the signal intensity distribution based on the standard deviations used by the filtering kernel. These cropping limits were applied by defining a local coordinate system (x', y', z'), with the z'-axis aligned along the needle trajectory, the x'-axis aligned along the tangential (t) image direction, and the y'-axis aligned along the radial (r) image direction at each point along the needle trajectory. Sub-volume cropping was performed with $0.16 \times 0.16 \times 0.16$ mm^3 voxel dimensions.

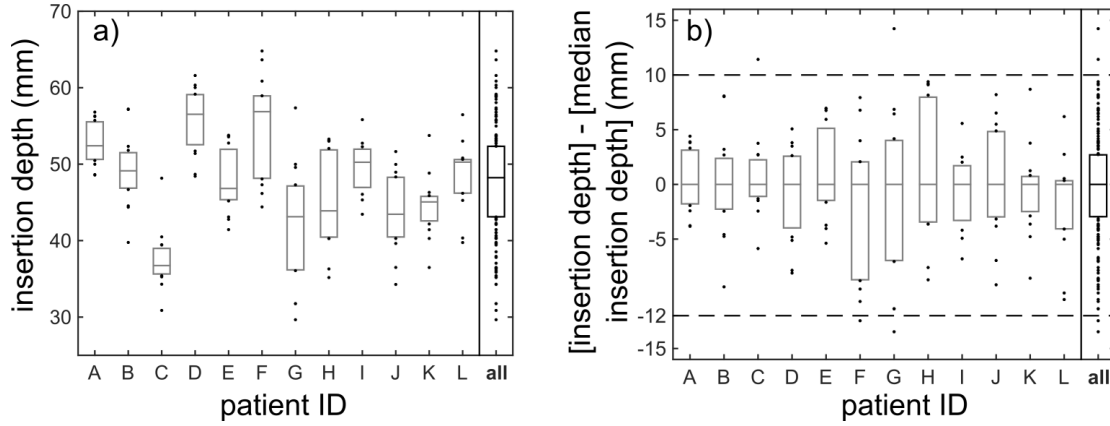Figure B.2: a) Boxplots of insertion depths (length of the needle within the SR3D image) of the 185 manually segmented needles for each individual patient, and all patients combined. b) Boxplots of insertion depths after subtracting the median insertion depth for each patient. Horizontal lines at -12 mm and 10 mm indicate the insertion depth limits used by the tip localization algorithm. In all plots the center-lines indicate median value, boxes indicate inter-quartile range, and points indicate values outside of the inter-quartile range.

B.2.2 Sub-Volume Filtering

Following cropping, the cropped signal intensity values were filtered in the y' direction using the intensity-curvature based filter as described in section 3.2.2, but to preserve spatial resolution in the insertion direction the signal intensity was not convolved with a uniform distribution in the z' direction. Following filtering, signal intensities were averaged in the x' and y' directions to produce 1D intensity profiles as a function of z' as shown in Figure 3.4.

B.2.3 Signal Intensity Profile Analysis

The needle tip corresponds to a signal intensity drop at the most superior point along the needle trajectory. Intensity breaks along a needle trajectory caused by imaging artifacts can cause intensity drops preceding the needle tip; however, the drop associated with the visible needle tip will be the most superior when inserted trans-perineally. Figure 3.4a-c displays cross sections and intensity profiles of a needle with a signal intensity

break inferior to the tip location. The first derivative of the 1D signal intensity profile was calculated by finding the intensity slope within 2.5 mm of each point using linear least-squares, as shown in Figure 3.4d. This derivative profile was normalized by the maximum value, and all local peaks with values greater than 0.7 were identified using MATLABs findpeaks function, and the tip was selected as the most superior of these peaks.

B.3   Radial-Tangential Error Components

Let $p_m[p_{m,x}, p_{m,y}]$ and $p_a[p_{a,x}, p_{a,y}]$ be the 2D axial coordinates of corresponding manual and algorithm-based segmentations. The 2D axial distance between these points is $|\vec{d}|$, where $\vec{d} = p_a - p_m$. To express $\vec{d}$ in terms of the r and t components at point p_m, a rotation matrix A was defined that effectively rotates the y-coordinate into r and the x-coordinate into t at point p_m, expressed as

$$A = \begin{pmatrix} \frac{1}{\sqrt{1+u^2}} & \frac{u}{\sqrt{1+u^2}} \\ \frac{-u}{\sqrt{1+u^2}} & \frac{1}{\sqrt{1+u^2}} \end{pmatrix} \tag{B.1}$$

$$u = \frac{p_{m,x}}{p_{m,y}} \tag{B.2}$$

This rotation matrix was applied to $\vec{d}$ to obtain the r and t components while preserving the length $|\vec{d}|$ in the rotated coordinate system. This method was used to find the r and t trajectory error components in section 3.2.3, and the r and t tip error components in section 3.2.3.

Appendix C

Appendix to Chapter 5

C.1 Three-Time-Point Method Calibration

The calibration parameters of the 3TP method are the three time points used for image analysis, the thresholds on wash-out rate for color assignment, and the conversion factor from normalized wash-in rate to 8-bit intensity values. Calibration is performed by simulating signal enhancement curves for a variety of K^{trans} and EES fractional volumes (v_e), applying the 3TP method to the curves, and displaying the resultant color and intensity matrix. Parameters are iteratively updated until approximately equal portions of the matrix are red, green, and blue, and the full 8-bit intensity spectrum is displayed [1]. This calibration was performed in MATLAB 2015a (Mathworks, Natick MA USA) using the Tofts two-compartment pharmacokinetic model [2], the population averaged AIF measured by Parker et al. [3], and the non-linear FSPGR signal equation [4] using the pulse sequence parameters from cohort A and B. For both cohorts, the three time points were selected as the pre-contrast image and images 1.5 min and 4.5 min post contrast onset, the intensity thresholds for washout-rate were >5% for blue, <5% and >-15% for green, and <-15% for red, and the intensity conversion factor was 150. The resultant color matrices for cohorts A and B are provided in Figure C.1.
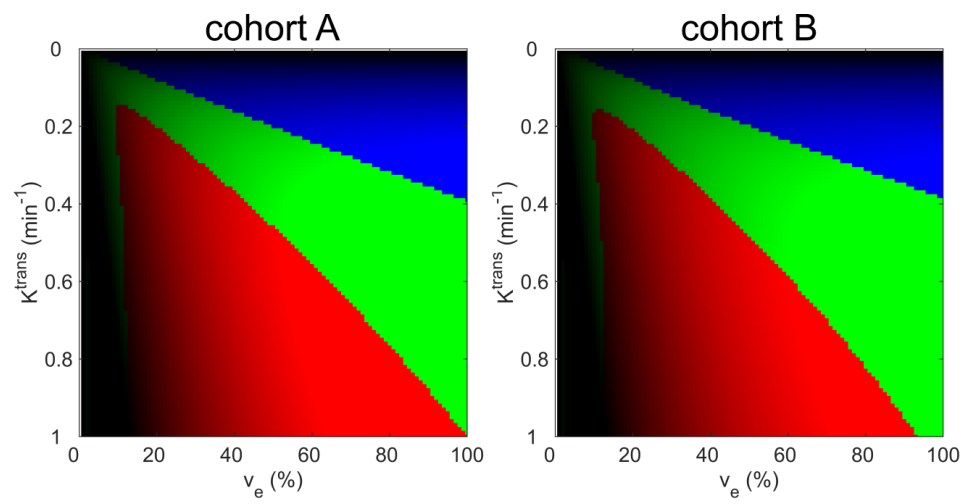
Figure C.1: Color intensity matrices used for 3TP method calibration.

References

1. Degani, H., Gusis, V., Weinstein, D., Fields, S. & Strano, S. Mapping patho-physiological features of breast tumors by MRI at high spatial resolution. *Nature Medicine* **3,** 780–782 (1997).

2. Tofts, P. S. *et al.* Estimating kinetic parameters from dynamic contrast-enhanced T1-weighted MRI of a diffusable tracer: Standardized quantities and symbols. *Journal of Magnetic Resonance Imaging* **10,** 223–232 (1999).

3. Parker, G. J. M. *et al.* Experimentally-derived functional form for a population-averaged high-temporal-resolution arterial input function for dynamic contrast-enhanced MRI. *Magnetic Resonance in Medicine* **56,** 993–1000 (2006).

4. Dathe, H. & Helms, G. Exact algebraization of the signal equation of spoiled gradient echo MRI. *Physics in Medicine and Biology* **55,** 4231–4245 (2010).

Appendix D

Ethics Approvals

	Health	Santé
	Canada	Canada
	Health Products	Direction générale des produits
	and Food Branch	de santé et des aliments

DATE: JUL 0 7 2011

Application No. 178857

Investigational Testing Authorization - Class II

Dear Chandima Edirisinghe:

This is in reference to your application for Authorization to conduct Investigational Testing in Canada, received on 10 March 2011, and submitted pursuant to Part 3 of the *Medical Devices Regulations*. This pertains to the following:

Protocol: An Improved Prostate Imaging and Cancer Treatment Procedure

Objectives: (1) To determine the accuracy improvement to the treatment delivery using 3-dimensional imaging

(2) To determine the effectiveness of the intra-operative delivery adjustment to compensate for prostate movement, and

(3) To determine whether only ultrasound imaging can be used throughout the procedure and instead of combination of CT imaging and ultrasound imaging.

(4) To determine whether better delivery can be done using the flexibility of the non-template mechanical device.

Device: "3D Ultrasound Prostate Imaging and Cancer Treatment Planning System"

No. of devices: One (1)

No. of subjects: Ten (10)

The information has been reviewed and you are hereby authorized under Section 83 of the *Medical Devices Regulations* to sell the subject device for investigational testing to the institution(s) listed in the attached Appendix 1.

Sections 86, 87 and 88 of the *Medical Devices Regulations* impose additional requirements regarding the advertisement, record keeping and labelling of devices involved in investigational trials. Please advise the Bureau of any changes to the device, protocol or list of investigators. Any changes to the device or protocol that fall outside the scope of the risk assessment of this protocol will require a new application.

Yours sincerely,

Director
Medical Devices Bureau

RGR/mw
Attach.

Canada

Dr. David D'Souza

Western Research

Western University Health Science Research Ethics Board
HSREB Delegated Initial Approval Notice

Principal Investigator: Dr. David D'Souza
Department & Institution: Schulich School of Medicine and Dentistry\Oncology, London Health Sciences Centre

Review Type: Delegated
HSREB File Number: 108857
Study Title: Evaluation of organ and needle segmentation accuracy using 3D ultrasound for brachytherapy treatment planning.

HSREB Initial Approval Date: February 09, 2017
HSREB Expiry Date: February 09, 2018

Documents Approved and/or Received for Information:

Document Name	Comments	Version Date
Western University Protocol	108857_D'Souza Protocol	2017/01/31
Data Collection Form/Case Report Form	Data collection form.	2017/01/05

The Western University Health Science Research Ethics Board (HSREB) has reviewed and approved the above named study, as of the HSREB Initial Approval Date noted above.

HSREB approval for this study remains valid until the HSREB Expiry Date noted above, conditional to timely submission and acceptance of HSREB Continuing Ethics Review.

The Western University HSREB operates in compliance with the Tri-Council Policy Statement Ethical Conduct for Research Involving Humans (TCPS2), the International Conference on Harmonization of Technical Requirements for Registration of Pharmaceuticals for Human Use Guideline for Good Clinical Practice Practices (ICH E6 R1), the Ontario Personal Health Information Protection Act (PHIPA, 2004), Part 4 of the Natural Health Product Regulations, Health Canada Medical Device Regulations and Part C, Division 5, of the Food and Drug Regulations of Health Canada.

Members of the HSREB who are named as Investigators in research studies do not participate in discussions related to, nor vote on such studies when they are presented to the REB.

The HSREB is registered with the U.S. Department of Health & Human Services under the IRB registration number IRB 00000940.

Western Research

Western University Health Science Research Ethics Board
HSREB Annual Continuing Ethics Approval Notice

Date: October 11, 2016
Principal Investigator: Dr. Joseph Chin
Department & Institution: Schulich School of Medicine and Dentistry\Oncology,London Health Sciences Centre

Review Type: Full Board
HSREB File Number: 5650
Study Title: Histopathologic Validation of Pre-operative Prostate Cancer Imaging (REB 15551)
Sponsor: Canadian Institutes of Health Research

HSREB Renewal Due Date & HSREB Expiry Date:
Renewal Due -2017/10/31
Expiry Date -2017/11/13

The Western University Health Science Research Ethics Board (HSREB) has reviewed the Continuing Ethics Review (CER) Form and is re-issuing approval for the above noted study.

The Western University HSREB operates in compliance with the Tri-Council Policy Statement Ethical Conduct for Research Involving Humans (TCPS2), the International Conference on Harmonization of Technical Requirements for Registration of Pharmaceuticals for Human Use Guideline for Good Clinical Practice (ICH E6 R1), the Ontario Freedom of Information and Protection of Privacy Act (FIPPA, 1990), the Ontario Personal Health Information Protection Act (PHIPA, 2004), Part 4 of the Natural Health Product Regulations, Health Canada Medical Device Regulations and Part C, Division 5, of the Food and Drug Regulations of Health Canada.

Members of the HSREB who are named as Investigators in research studies do not participate in discussions related to, nor vote on such studies when they are presented to the REB.

The HSREB is registered with the U.S. Department of Health & Human Services under the IRB registration number IRB 00000940.

Ethics Officer: Erika Basile ___ Katelyn Harris___ Nicole Kaniki___ Grace Kelly ___ Vikki Tran ___ Karen Gopaul___

Western Research

Western University Health Science Research Ethics Board
HSREB Annual Continuing Ethics Approval Notice

Date: June 23, 2016
Principal Investigator: Dr. Joseph Chin
Department & Institution: Schulich School of Medicine and Dentistry\Oncology,London Health Sciences Centre

Review Type: Full Board
HSREB File Number: 101038
Study Title: Multi-modality Prostate Cancer Image Guided Interventions (REB #18135)
Sponsor: Canadian Institutes of Health Research

HSREB Renewal Due Date & HSREB Expiry Date:
Renewal Due -2017/06/30
Expiry Date -2017/07/19

The Western University Health Science Research Ethics Board (HSREB) has reviewed the Continuing Ethics Review (CER) Form and is re-issuing approval for the above noted study.

The Western University HSREB operates in compliance with the Tri-Council Policy Statement Ethical Conduct for Research Involving Humans (TCPS2), the International Conference on Harmonization of Technical Requirements for Registration of Pharmaceuticals for Human Use Guideline for Good Clinical Practice (ICH E6 R1), the Ontario Freedom of Information and Protection of Privacy Act (FIPPA, 1990), the Ontario Personal Health Information Protection Act (PHIPA, 2004), Part 4 of the Natural Health Product Regulations, Health Canada Medical Device Regulations and Part C, Division 5, of the Food and Drug Regulations of Health Canada.

Members of the HSREB who are named as Investigators in research studies do not participate in discussions related to, nor vote on such studies when they are presented to the REB.

The HSREB is registered with the U.S. Department of Health & Human Services under the IRB registration number IRB 00000940.

Ethics Officer: Erika Basile ___ Katelyn Harris___ Nicole Kaniki___ Grace Kelly ___ Vikki Tran ___ Karen Gopaul ✓

Appendix E

Copyright Releases

Copyright
Clearance
Center

RightsLink®

BRACHYTHERAPY

Title: Three-dimensional transrectal ultrasound guided high-dose-rate prostate brachytherapy: A comparison of needle segmentation accuracy with two-dimensional image guidance

Author: William Thomas Hrinivich,Douglas A. Hoover,Kathleen Surry,Chandima Edirisinghe,Jacques Montreuil,David D'Souza,Aaron Fenster,Eugene Wong

Publication: Brachytherapy

Publisher: Elsevier

Date: Dec 31, 1969

Copyright © 1969, Elsevier

Logged in as:
William Hrinivich
Account #:
3001134265

LOGOUT

Order Completed

Thank you for your order.

This Agreement between William Hrinivich ("You") and Elsevier ("Elsevier") consists of your order details and the terms and conditions provided by Elsevier and Copyright Clearance Center.

License number	Reference confirmation email for license number
License date	Apr, 04 2017
Licensed Content Publisher	Elsevier
Licensed Content Publication	Brachytherapy
Licensed Content Title	Three-dimensional transrectal ultrasound guided high-dose-rate prostate brachytherapy: A comparison of needle segmentation accuracy with two-dimensional image guidance
Licensed Content Author	William Thomas Hrinivich,Douglas A. Hoover,Kathleen Surry,Chandima Edirisinghe,Jacques Montreuil,David D'Souza,Aaron Fenster,Eugene Wong
Licensed Content Date	March–April 2016
Licensed Content Volume	15
Licensed Content Issue	2
Licensed Content Pages	9
Type of Use	reuse in a thesis/dissertation
Portion	full article
Format	electronic
Are you the author of this Elsevier article?	Yes
Will you be translating?	No
Order reference number	
Title of your thesis/dissertation	Tools for improving the efficacy of high-dose-rate prostate cancer brachytherapy using 3D ultrasound and dynamic contrast enhanced magnetic resonance imaging
Expected completion date	Apr 2017
Estimated size (number of pages)	150
Elsevier VAT number	GB 494 6272 12
Requestor Location	

Billing Type   Invoice

Billing address

Total

[CLOSE WINDOW]

JOHN WILEY AND SONS LICENSE
TERMS AND CONDITIONS

Apr 06, 2017

This Agreement between William Hrinivich ("You") and John Wiley and Sons ("John Wiley and Sons") consists of your license details and the terms and conditions provided by John Wiley and Sons and Copyright Clearance Center.

License Number	4081430348848
License date	
Licensed Content Publisher	John Wiley and Sons
Licensed Content Publication	Medical Physics
Licensed Content Title	Simultaneous automatic segmentation of multiple needles using 3D ultrasound for high-dose-rate prostate brachytherapy
Licensed Content Author	William Thomas Hrinivich,Douglas A. Hoover,Kathleen Surry,Chandima Edirisinghe,Jacques Montreuil,David D'Souza,Aaron Fenster,Eugene Wong
Licensed Content Date	Mar 14, 2017
Licensed Content Pages	1
Type of use	Dissertation/Thesis
Requestor type	Author of this Wiley article
Format	Electronic
Portion	Full article
Will you be translating?	No
Title of your thesis / dissertation	Tools for improving the efficacy of high-dose-rate prostate cancer brachytherapy using 3D ultrasound and dynamic contrast enhanced magnetic resonance imaging
Expected completion date	Apr 2017
Expected size (number of pages)	150
Requestor Location	
Publisher Tax ID	
Billing Type	
Billing Address	
Total	
Terms and Conditions	

TERMS AND CONDITIONS

This copyrighted material is owned by or exclusively licensed to John Wiley & Sons, Inc. or one of its group companies (each a"Wiley Company") or handled on behalf of a society with which a Wiley Company has exclusive publishing rights in relation to a particular work (collectively "WILEY"). By clicking "accept" in connection with completing this licensing transaction, you agree that the following terms and conditions apply to this transaction (along with the billing and payment terms and conditions established by the Copyright Clearance Center Inc., ("CCC's Billing and Payment terms and conditions"), at the time that you opened your RightsLink account (these are available at any time at http://myaccount.copyright.com).

Terms and Conditions

- The materials you have requested permission to reproduce or reuse (the "Wiley Materials") are protected by copyright.

- You are hereby granted a personal, non-exclusive, non-sub licensable (on a stand-alone basis), non-transferable, worldwide, limited license to reproduce the Wiley Materials for the purpose specified in the licensing process. This license, **and any CONTENT (PDF or image file) purchased as part of your order,** is for a one-time use only and limited to any maximum distribution number specified in the license. The first instance of republication or reuse granted by this license must be completed within two years of the date of the grant of this license (although copies prepared before the end date may be distributed thereafter). The Wiley Materials shall not be used in any other manner or for any other purpose, beyond what is granted in the license. Permission is granted subject to an appropriate acknowledgement given to the author, title of the material/book/journal and the publisher. You shall also duplicate the copyright notice that appears in the Wiley publication in your use of the Wiley Material. Permission is also granted on the understanding that nowhere in the text is a previously published source acknowledged for all or part of this Wiley Material. Any third party content is expressly excluded from this permission.

- With respect to the Wiley Materials, all rights are reserved. Except as expressly granted by the terms of the license, no part of the Wiley Materials may be copied, modified, adapted (except for minor reformatting required by the new Publication), translated, reproduced, transferred or distributed, in any form or by any means, and no derivative works may be made based on the Wiley Materials without the prior permission of the respective copyright owner.**For STM Signatory Publishers clearing permission under the terms of the STM Permissions Guidelines only, the terms of the license are extended to include subsequent editions and for editions in other languages, provided such editions are for the work as a whole in situ and does not involve the separate exploitation of the permitted figures or extracts,** You may not alter, remove or suppress in any manner any copyright, trademark or other notices displayed by the Wiley Materials. You may not license, rent, sell, loan, lease, pledge, offer as security, transfer or assign the Wiley Materials on a stand-alone basis, or any of the rights granted to you hereunder to any other person.

- The Wiley Materials and all of the intellectual property rights therein shall at all times remain the exclusive property of John Wiley & Sons Inc, the Wiley Companies, or their respective licensors, and your interest therein is only that of having possession of and the right to reproduce the Wiley Materials pursuant to Section 2 herein during the continuance of this Agreement. You agree that you own no right, title or interest in or to the Wiley Materials or any of the intellectual property rights therein. You shall have no rights hereunder other than the license as provided for above in Section 2. No right,

license or interest to any trademark, trade name, service mark or other branding ("Marks") of WILEY or its licensors is granted hereunder, and you agree that you shall not assert any such right, license or interest with respect thereto

- NEITHER WILEY NOR ITS LICENSORS MAKES ANY WARRANTY OR REPRESENTATION OF ANY KIND TO YOU OR ANY THIRD PARTY, EXPRESS, IMPLIED OR STATUTORY, WITH RESPECT TO THE MATERIALS OR THE ACCURACY OF ANY INFORMATION CONTAINED IN THE MATERIALS, INCLUDING, WITHOUT LIMITATION, ANY IMPLIED WARRANTY OF MERCHANTABILITY, ACCURACY, SATISFACTORY QUALITY, FITNESS FOR A PARTICULAR PURPOSE, USABILITY, INTEGRATION OR NON-INFRINGEMENT AND ALL SUCH WARRANTIES ARE HEREBY EXCLUDED BY WILEY AND ITS LICENSORS AND WAIVED BY YOU.

- WILEY shall have the right to terminate this Agreement immediately upon breach of this Agreement by you.

- You shall indemnify, defend and hold harmless WILEY, its Licensors and their respective directors, officers, agents and employees, from and against any actual or threatened claims, demands, causes of action or proceedings arising from any breach of this Agreement by you.

- IN NO EVENT SHALL WILEY OR ITS LICENSORS BE LIABLE TO YOU OR ANY OTHER PARTY OR ANY OTHER PERSON OR ENTITY FOR ANY SPECIAL, CONSEQUENTIAL, INCIDENTAL, INDIRECT, EXEMPLARY OR PUNITIVE DAMAGES, HOWEVER CAUSED, ARISING OUT OF OR IN CONNECTION WITH THE DOWNLOADING, PROVISIONING, VIEWING OR USE OF THE MATERIALS REGARDLESS OF THE FORM OF ACTION, WHETHER FOR BREACH OF CONTRACT, BREACH OF WARRANTY, TORT, NEGLIGENCE, INFRINGEMENT OR OTHERWISE (INCLUDING, WITHOUT LIMITATION, DAMAGES BASED ON LOSS OF PROFITS, DATA, FILES, USE, BUSINESS OPPORTUNITY OR CLAIMS OF THIRD PARTIES), AND WHETHER OR NOT THE PARTY HAS BEEN ADVISED OF THE POSSIBILITY OF SUCH DAMAGES. THIS LIMITATION SHALL APPLY NOTWITHSTANDING ANY FAILURE OF ESSENTIAL PURPOSE OF ANY LIMITED REMEDY PROVIDED HEREIN.

- Should any provision of this Agreement be held by a court of competent jurisdiction to be illegal, invalid, or unenforceable, that provision shall be deemed amended to achieve as nearly as possible the same economic effect as the original provision, and the legality, validity and enforceability of the remaining provisions of this Agreement shall not be affected or impaired thereby.

- The failure of either party to enforce any term or condition of this Agreement shall not constitute a waiver of either party's right to enforce each and every term and condition of this Agreement. No breach under this agreement shall be deemed waived or excused by either party unless such waiver or consent is in writing signed by the party granting such waiver or consent. The waiver by or consent of a party to a breach of any provision of this Agreement shall not operate or be construed as a waiver of or consent to any other or subsequent breach by such other party.

- This Agreement may not be assigned (including by operation of law or otherwise) by you without WILEY's prior written consent.

- Any fee required for this permission shall be non-refundable after thirty (30) days from receipt by the CCC.

- These terms and conditions together with CCC's Billing and Payment terms and conditions (which are incorporated herein) form the entire agreement between you and WILEY concerning this licensing transaction and (in the absence of fraud) supersedes all prior agreements and representations of the parties, oral or written. This Agreement may not be amended except in writing signed by both parties. This Agreement shall be binding upon and inure to the benefit of the parties' successors, legal representatives, and authorized assigns.

- In the event of any conflict between your obligations established by these terms and conditions and those established by CCC's Billing and Payment terms and conditions, these terms and conditions shall prevail.

- WILEY expressly reserves all rights not specifically granted in the combination of (i) the license details provided by you and accepted in the course of this licensing transaction, (ii) these terms and conditions and (iii) CCC's Billing and Payment terms and conditions.

- This Agreement will be void if the Type of Use, Format, Circulation, or Requestor Type was misrepresented during the licensing process.

- This Agreement shall be governed by and construed in accordance with the laws of the State of New York, USA, without regards to such state's conflict of law rules. Any legal action, suit or proceeding arising out of or relating to these Terms and Conditions or the breach thereof shall be instituted in a court of competent jurisdiction in New York County in the State of New York in the United States of America and each party hereby consents and submits to the personal jurisdiction of such court, waives any objection to venue in such court and consents to service of process by registered or certified mail, return receipt requested, at the last known address of such party.

WILEY OPEN ACCESS TERMS AND CONDITIONS

Wiley Publishes Open Access Articles in fully Open Access Journals and in Subscription journals offering Online Open. Although most of the fully Open Access journals publish open access articles under the terms of the Creative Commons Attribution (CC BY) License only, the subscription journals and a few of the Open Access Journals offer a choice of Creative Commons Licenses. The license type is clearly identified on the article.

The Creative Commons Attribution License

The Creative Commons Attribution License (CC-BY) allows users to copy, distribute and transmit an article, adapt the article and make commercial use of the article. The CC-BY license permits commercial and non-

Creative Commons Attribution Non-Commercial License

The Creative Commons Attribution Non-Commercial (CC-BY-NC)License permits use, distribution and reproduction in any medium, provided the original work is properly cited and is not used for commercial purposes.(see below)

Creative Commons Attribution-Non-Commercial-NoDerivs License

The Creative Commons Attribution Non-Commercial-NoDerivs License (CC-BY-NC-ND) permits use, distribution and reproduction in any medium, provided the original work is properly cited, is not used for commercial purposes and no modifications or adaptations are made. (see below)

Use by commercial "for-profit" organizations
Use of Wiley Open Access articles for commercial, promotional, or marketing purposes requires further explicit permission from Wiley and will be subject to a fee.
Further details can be found on Wiley Online Library
http://olabout.wiley.com/WileyCDA/Section/id-410895.html

Other Terms and Conditions:

v1.10 Last updated September 2015

Appendix F

Curriculum Vitae

William Thomas Hrinivich, B.Sc.

A. EDUCATIONAL BACKGROUND

2012 - Present   *Ph.D. Candidate, CAMPEP Clinical M.Sc., Dept. of Medical Biophysics*
The University of Western Ontario (UWO), London ON
Supervisors: Eugene Wong, Ph.D., FCCPM; Aaron Fenster, Ph.D., FCCPM
Thesis title: *"Image-Guided Focal Brachytherapy for Prostate Cancer"*

2008 - 2012   *B.Sc. Medical Physics, Dept. of Physics and Astronomy*
The University of Western Ontario (UWO), London ON

B. PUBLICATIONS

i. Refereed journal articles

Hrinivich WT, Hoover DA, Surry K, Edirisinghe C, Velker V, Bauman G, D'Souza D, Fenster A, Wong E. "Accuracy and variability of high-dose-rate prostate brachytherapy needle tip localization using live two-dimensional and sagittally-reconstructed three-dimensional ultrasound.", Brachytherapy, *[Accepted May 9, 2017]*

Gutpel K, Tasevski N, Wong B, **Hrinivich WT**, Su F, Hadway J, Desjardins L, Lee TY, Hoffman L. "ANG1 treatment reduces muscle pathology and prevents a decline in perfusion in DMD mice". PLOS ONE. *[In Press]*

Hrinivich WT, Hoover DA, Surry K, Edirisinghe C, D'Souza D, Fenster A, Wong E. "Simultaneous automatic segmentation of multiple needles using three-dimensional ultrasound for high-dose-rate prostate brachytherapy.", Medical Physics. *[In Press]*

Hrinivich WT, Hoover, DA, Surry K, Edirisinghe C, Montreuil J, D'Souza D, Fenster A, Wong E. **"**Three-dimensional transrectal ultrasound guided high-dose-rate prostate brachytherapy: a comparison of needle segmentation accuracy with two-dimensional image-guidance" Brachytherapy. 2016; 15(2) *[PMID: 26832673]*

Gutpel K, **Hrinivich WT**, Hoffman L. "Skeletal muscle fibrosis in the mdx/utrn+/- mouse validates its suitability as a murine model of Duchenne muscular dystrophy". PLOS ONE. 2015; 10(1) *[PMID: 25607927]*

Jensen M, **Hrinivich WT,** Jung A, Holdsworth DW, Drangova M, Chen J, Wong E. "Implementation and commissioning of an integrated micro-CT/RT system with computerized independent jaw collimation". Medical Physics. 2013; 40(8) *[PMID: 23927303]*

iii. Refereed conference proceedings

Hrinivich WT, Hoover D, Surry K, Edirisinghe C, D'Souza D, Fenster A, Wong E. "A comparison of needle tip localization accuracy using 2D and 3D trans-rectal ultrasound for high-dose-rate brachytherapy treatment planning." Progress in Biomedical Imaging and Optics - Proceedings of SPIE, 2016

Hrinivich WT, Gibson E, Gaed M, Gomez J, Moussa M, McKenzie CA, Bauman GS, Ward AD Fenster A, Wong E. *A dimensionless dynamic contrast enhanced MRI parameter for intra-prostatic tumour target volume delineation: Initial comparison with histology.* Progress in Biomedical Imaging and Optics - Proceedings of SPIE, 2014

Gibson E, Gaed M, **Hrinivich WT**, Gómez JA, Moussa M, Romagnoli C, Mandel J, Bastian-Jordan M, Cool D, Ghoul S, Pautler S, Chin JL, Crukley C, Bauman GS, Fenster A, Ward AD. "Multiparametric MR imaging of prostate cancer foci: assessing the detectability and localizability of Gleason 7 peripheral zone cancers based on image contrasts*.* Progress in Biomedical Imaging and Optics - Proceedings of SPIE, 2014

iv. News articles

Hrinivich WT. "Prostate cancer imaging improves the big picture for patients.", The Londoner, November 17, 2016, London, ON, Canada

C. SCHOLARSHIPS
* indicates funding declined

2015, 2016, 2017	*Frederick Banting and Charles Best Canada Graduate Scholarship Doctoral Award (CGS-D)* Canadian Institutes of Health Research Value: $35,000 annually
2013*, 2014, 2015*	*Queen Elizabeth II Graduate Scholarship in Science and Technology* UWO Ontario Graduate Scholarship Value: $15,000 annually
2012, 2013, 2014 2015*	*Cancer Research and Technology Transfer (CaRTT) Trainee* Canadian Institutes of Health Research Value: $26,700 annually
2013	*Frederick Banting and Charles Best Canada Graduate Scholarship Master's Award (CGS-M)* Canadian Institutes of Health Research Value: $17,500 annually

D. AWARDS AND HONOURS

21/07/2016   *First place award in the J.R. Cunningham Young Investigator's Symposium*
Canadian Organization of Medical Physicists (COMP) Annual Scientific Meeting
St. John's NL
Value: $500

26/06/2015   *Poster Award*
Research and Education Day, Department of Oncology, UWO
London ON
Value: $100

2015   *Alan C Groom Award*
Department of Medical Biophysics, UWO
London ON
Value: $1000
Awarded for delivering the most effective Medical Biophysics departmental seminar of the year.

20/06/2014   *Poster Award*
Research and Education Day, Department of Oncology, UWO
London ON
Value: $100

24/03/2014   *First place poster award for the Ontario Consortium for Adaptive Interventions in Radiation Oncology (OCAIRO)*
Imaging Network Ontario (ImNO) Symposium
Toronto ON
Value: $300

18/03/2014   *Poster award in Medical Physics, Engineering and Imaging*
London Health Research Day (LHRD)
London ON
Value: $500

2012   *Western Gold Medal in Medical Physics*
Department of Physics & Astronomy*,* UWO
London ON
Awarded to student with highest cumulative average in the program upon graduation.

E. PRESENTATIONS

i. Podium presentations

Hrinivich WT, Hoover DA, Surry K, D'Souza D, Bauman G, Martin P, Ward A, McKenzie C, Fenster A, Wong E. *3D ultrasound and magnetic resonance imaging for prostate tumour-targeted high-dose-rate brachytherapy.* Oral presentation at Canadian Association of Physicists (CAP) Annual Meeting, Kingston ON, CAN. June 1, 2017 (***Invited speaker.***)

Hrinivich WT, Hoover DA, Surry K, Edirisinghe C, D'Souza D, Fenster A, Wong E. *Robotically-assisted 3D ultrasound guided high-dose-rate prostate brachytherapy.* Short oral presentation at American Brachytherapy Society (ABS) Annual Meeting, Boston MA, USA. April 22, 2017

Hrinivich WT, Hoover DA, Surry K, Edirisinghe C, D'Souza D, Fenster A, Wong E. *Combining sagittally-reconstructed 3D and live-2D ultrasound for high-dose-rate prostate brachytherapy needle segmentation.* Oral presentation at Canadian Organization of Medical Physicists (COMP) Annual Meeting, St. John's NL, CAN. July 21, 2016 (***First place winner in the Young Investigators Symposium.***)

Hrinivich WT, Hoover DA, Surry K, Edirisinghe C, D'Souza D, Fenster A, Wong E. *Ultrasound guided high-dose-rate prostate brachytherapy: live needle segmentation and 3D image reconstruction using the sagittal transducer.* Oral presentation at Oncology Research and Education Day, London ON, CAN. June 17, 2016

Hrinivich WT, Hoover DA, Surry K, Edirisinghe C, Montreuil J, D'Souza D, Fenster A, Wong E. *Intra-operative 3D image-guided radiotherapy for prostate cancer.* Oral presentation at the 25th Annual AC Burton Day, London ON, CAN. April 7, 2016. (***Invited speaker.***)

Hrinivich WT, Hoover DA, Surry K, Edirisinghe C, Montreuil J, D'Souza D, Fenster A, Wong E. *A comparison of needle tip localization accuracy using 2D and 3D trans-rectal ultrasound for high-dose-rate prostate cancer brachytherapy treatment planning.* Oral presentation at SPIE Medical Imaging, San Diego CA, USA. March 1, 2016

Hrinivich WT, Hoover DA, Surry K, D'Souza D, Fenster A, Wong E. *Semi-automatic segmentation of high-dose-rate prostate brachytherapy needles using 3D ultrasound.* Oral Presentation at the Imaging Network Ontario (ImNO) Symposium, Toronto ON, CAN. March 31, 2016

Hrinivich WT, Gibson E, McKenzie CA, Bauman GS, Ward AD, Fenster A, Wong E. *Dynamic contrast enhanced MRI for prostate cancer localization: signal generation and quantification.* Oral presentation at London Cancer Research Trainee Forum, London ON, CAN. November 12, 2015 (***Invited speaker.***)

Hrinivich WT, Hoover DA, Surry K, D'Souza D, Fenster A, Wong E. *3D trans-rectal ultrasound for high-dose-rate prostate brachytherapy: a comparison of 3D image volumes with intra-operative 2D imaging.* Oral presentation at IUPESM World Congress of Medical Physics, Toronto ON, CAN. June 12, 2015

Hrinivich WT, Gibson E, McKenzie CA, Bauman GS, Ward AD, Fenster A, Wong E. *A tale of two pulse sequences: hard lessons learned in computing K^{trans} from dynamic contrast enhanced prostate MRI.* Oral Presentation at the OICR Smarter Imaging Program: Imaging Applications in Prostate Cancer Workshop, London ON, CAN. November 21, 2014 (***Invited speaker.***)

Hrinivich WT, Thang T, McKenzie CA, Bauman GS, Fenster A, Wong E. *Dynamic contrast enhanced MRI parameter map sensitivity to imaging temporal resolution in the prostate.* Oral and Poster Presentation at the Imaging Network Ontario (ImNO) Symposium, Toronto ON, CAN. March 24, 2014 (***Received first place award for corresponding poster presentation.***)

ii. Poster presentations

Hrinivich WT, Hoover D, Surry K, Edirisinghe C, D'Souza D, Fenster A, Wong E. *Image-guided high-dose-rate prostate brachytherapy: combining 2D and 3D ultrasound for needle tip localization.* Poster/Oral Presentation at the OICR Smarter Imaging Program: Imaging Applications in Prostate Cancer Workshop, London ON, CAN. Nov. 25, 2016

Hrinivich WT, Hoover D, Surry K, D'Souza D, Fenster A, Wong E. *Ultrasound guided high-dose-rate prostate brachytherapy: live needle segmentation and 3D image reconstruction using the sagittal transducer.* Poster presentation at American Brachytherapy Society (ABS) World Congress of Brachytherapy, San Francisco CA, USA. June 26, 2016

Hrinivich WT, Hoover D, Surry K, D'Souza D, Fenster A, Wong E. *3D trans-rectal ultrasound for high-dose-rate prostate brachytherapy: a comparison of 3D image volumes with intra-operative 2D imaging.* Poster presentation at Canadian Association of Radiation Oncologists (CARO) Annual Meeting, Kelowna BC, CAN. Sept 9, 2015 *(Poster presented by David D'Souza).*

Hrinivich WT, Hoover D, Surry K, D'Souza D, Fenster A, Wong E. *3D trans-rectal ultrasound for high-dose-rate prostate brachytherapy: a comparison of 3D image volumes with intra-operative 2D imaging.* Poster presentation at Oncology Research and Education Day, London ON, CAN. June 26, 2015 (***Received award for poster presentation*.**)

Hrinivich WT, Hoover D, Surry K, D'Souza D, Fenster A, Wong E. *3D trans-rectal ultrasound for high-dose-rate prostate brachytherapy: a comparison of 3D image volumes with intra-operative 2D imaging.* Poster presentation at London Health Research Day, London ON, CAN. April 1, 2015

Hrinivich WT, Hoover D, Surry K, D'Souza D, Fenster A, Wong E. *Automatic segmentation of multiple needles in 3D trans-rectal ultrasound images for prostate brachytherapy treatment planning.* Poster presentation at the Imaging Network Ontario (ImNO) Symposium, London ON, CAN. March 30, 2015

Hrinivich WT, Hoover D, Surry K, D'Souza D, Fenster A, Wong E. *3D trans-rectal ultrasound for high-dose-rate prostate brachytherapy: a comparison of 3D image volumes with intra-operative 2D imaging.* Poster presentation at the Ontario Institute for Cancer Research (OICR) Scientific Meeting, Toronto ON, CAN, March 12, 2015

Hrinivich WT, Gibson E, McKenzie CA, Bauman GS, Ward AD, Fenster A, Wong E. *Comparing dynamic contrast enhanced MRI parameters in the prostate derived from measured arterial input functions and reference muscle.* Poster presentation at Research and Education Day, London ON, CAN. June 20, 2014 (***Received award for poster presentation*.**)

Hrinivich WT, Edirisinghe C, D'Souza D, Surry K, Hoover D, Fenster A, Wong E. *Interstitial brachytherapy treatment for prostate cancer: Implementation and evaluation of a prototype 3D ultrasound guided mechatronic device.* Poster presentation and Canada Student Health Forum, Winnipeg MA, CAN. June 11, 2014

Hrinivich WT, Edirisinghe C, D'Souza D, Surry K, Hoover D, Fenster A, Wong E. *3D ultrasound guided needle insertion with a mechatronic device for prostate brachytherapy: Initial evaluation.*

Poster presentation at London Health Research Day, London ON, CAN. March 18, 2014 (***Received award for poster presentation***.)

Hrinivich WT, Gibson E, Gaed M, Gomez J, Moussa M, McKenzie CA, Bauman GS, Ward AD Fenster A, Wong E. *A dimensionless dynamic contrast enhanced MRI parameter for intra-prostatic tumour target volume delineation: Initial comparison with histology.* Poster Presentation at SPIE Medical Imaging, San Diego CA, USA. Feb. 17, 2014

Gibson E, Gaed M, **Hrinivich WT**, Gómez JA, Moussa M, Romagnoli C, Mandel J, Bastian-Jordan M, Cool D, Ghoul S, Pautler S, Chin JL, Crukley C, Bauman GS, Fenster A, Ward AD. *Multiparametric MR imaging of prostate cancer foci: assessing the detectability and localizability of Gleason 7 peripheral zone cancers based on image contrasts.* Poster Presentation at SPIE Medical Imaging, San Diego CA, USA. Feb. 17, 2014

Hrinivich WT, Thang T, McKenzie CA, Bauman GS, Fenster A, Wong E. *Dynamic contrast enhanced MRI parameter map sensitivity to imaging temporal resolution in the prostate.* Poster/Oral Presentation at the OICR Smarter Imaging Program: Imaging Applications in Prostate Cancer Workshop, London ON, CAN. Nov. 15, 2013
Hrinivich WT, Thang T, McKenzie CA, Bauman GS, Fenster A, Wong E. *A Dimensionless Dynamic Contrast Enhanced MRI Parameter for Target Volume Delineation.* Poster Presentation at the CARO COMP Joint Scientific Meeting, Montreal QC, CAN. Sept. 19, 2013

Hrinivich WT, Ryu B, Edirisinghe C, D'Souza D, Surry K, Fenster A, Wong E. *High Dose Rate Brachytherapy Catheter Localization using Intra-Operative 3D Trans-Rectal Ultrasound.* Poster Presentation at Oncology Research and Education Day, London ON, CAN. Jun. 21, 2013

Hrinivich WT, Thang T, McKenzie C, Bauman GS, Fenster A, Wong E. *Comparing Dynamic Contrast Enhanced MR Images of the Prostate for Two Pulse Sequences.* Poster Presentation at the Imaging Network Ontario (ImNO) Symposium, Toronto ON, CAN. Feb. 4, 2013

Hrinivich WT, McKenzie CA, Bauman GS, Fenster A, Wong E. *Comparing Dynamic Contrast Enhanced MR Images of the Prostate for Two Pulse Sequences.* Poster/Oral Presentation at the OICR Smarter Imaging Program: Imaging Applications in Prostate Cancer Workshop, London ON, CAN. Nov. 16, 2012

Hrinivich WT, Jensen M, Wong E, *A Point Densitometer Scanner for EBT2 Film Dosimetry.* Poster Presentation at the 2012 American Association of Physicists in Medicine Annual Meeting, Charlotte, NC, USA. Jul. 29, 2012

Jensen M, **Hrinivich WT**, Drangova M, Holdsworth D, Chen J, Wong E, *Commissioning Motorized Jaws for a Micro-CT/RT.* Poster Presentation at the 2012 American Association of Physicists in Medicine Annual Meeting, Charlotte, NC, USA. Jul. 29, 2012

F. TEACHING EXPERIENCE

2015, 2016	*Curriculum Development and Guest Lecturer***,** Problem Discovery and Solving 9704A Department of Medical Biophysics, UWO Course Instructor: Dr. Ali Khan *Curriculum developed through the Pedagogy in Biophysics program coordinated by Dr. Aaron Ward and Dr. Chris Ellis.*
2016	*Teaching Assistant***,** Practical Radiotherapy Physics 5672Y Department of Medical Biophysics, UWO Course Instructor: Dr. Kathleen Surry
2013, 2014	*Teaching Assistant***,** Introduction to Radiological Physics 4672A/9655A Department of Physics & Astronomy, UWO Course Instructor: Dr. Eugene Wong

G. COMMITTEES AND OUTREACH

2016	*Student Representative,* Planning Advisory Committee Cancer Research and Technology Transfer (CaRTT) Strategic Training Program, UWO
2015-present	*Volunteer*, "Let's Talk Cancer" High School Student Outreach Canadian Cancer Society, London ON
2012	*Chair,* Journal Club London Regional Cancer Program, London ON
2012-present	*Founder and Volunteer,* Wheels of Hope Annual Charity Cycling Tour Canadian Cancer Society, London ON *To date, the event has raised over $15,000 for patient transportation.*
2012	*Volunteer,* Cops for Cancer Battle in the Saddle Fundraiser Canadian Cancer Society, London ON
05/2011-06/2011	*Founder and Volunteer,* "Tom and Nate Cross Canada" Cycling Fundraiser Canadian Cancer Society, London ON *Event raised over $6,000 for research.*

H. RESEARCH ASSISTANTSHIPS

05/2012 – 07/2012, *Physics Research Assistant*
06/2011 – 08/2011, Department of Physics & Astronomy, UWO
05/2010 – 08/2010   Supervisor: Dr. Eugene Wong
Summary: Researched and developed an optical densitometer for radiochromic film digitization for small field dosimetry. Assisted with commissioning of a micro-CT-based small animal irradiator.

I. OTHER EXPERIENCE

i. Clinical experience

2013 – present   *Imaging Assistance for High-Dose-Rate Prostate Brachytherapy*
London Regional Cancer Program, London ON
Summary: Setup and operation of robotic system for 3D ultrasound imaging during routine HDR prostate brachytherapy procedures to facilitate clinical implementation of new hardware and software. To date, have attended over 50 HDR prostate brachytherapy procedures at the LRCP.

05/2014 – 09/2014, *Linear Accelerator Mechanical and Output Quality Assurance*
05/2015 – 09/2015   London Regional Cancer Program, London ON
Summary: Perform basic weekly mechanical and output measurements for Varian Clinac iX and TrueBeam linear accelerators (Sun Nuclear MapCheck, water tank, water-equivalent plastic phantom).

ii. Technical experience

- *Vitesse 2.5 and Brachyvision (Varian Medical Systems)*
  Experience with brachytherapy imaging and treatment planning software.

- *Object-oriented programming*
  Extensive object-oriented MATLAB experience, some Python, C++, and Java experience. Experience with relational databases (SQLite, Microsoft SQL Server).

- *RT DICOM standards*
  Experience reading and writing DICOM images, structure sets, and RT plans for HDR brachytherapy treatment planning.